University of Southern Queensland

Development and Characterisation of a Modified Smartphone Camera for Determining UVA Aerosol Optical Depth

A Dissertation submitted by

Damien Igoe, BAppSci, BSc (Hons), BSpecEd, DipEd, MEd, MSc

For the award of

Doctor of Philosophy

Supervisor: Professor Alfio Parisi

Associate Supervisor: Associate Professor Brad Carter

2013

Abstract

This research evaluates a specifically-written, calibrated and validated Android app installed on an inexpensive smartphone with bandpass and neutral density filters attached for measuring and quantifying direct solar UVA irradiances and aerosol optical depth. Currently, the equipment normally used to perform these observations is specialised, expensive and is available at a relatively small number of sites. The continuing proliferation of and the increasing number and type of sensors included in smartphones makes feasible the use of specifically designed apps as a cost effective supplementary means of monitoring direct ultraviolet A solar irradiance and air quality for research, education and community outreach purposes.

Most aerosols from both human and natural sources attenuate the UV wavebands; this has far reaching implications for UV irradiance studies and by extension, important public awareness metrics such as the UV index (UVI). Combined, closer observations and subsequent studies of aerosol optical depth and UVA irradiance are critical given that in recent studies, UVA irradiances have been found to be a major agent in skin cancer, photoaging and eye conditions. Therefore, this research involved the development, calibration and validation of a specifically written Android app on a smartphone in separate environments and across different seasons.

The smartphone camera image sensor’s response to UVA was first tested in the laboratory using a monochromator. Once it was shown that the response could be characterised, calibration and validation tests of the response to solar UVA and aerosol optical depth (AOD) were performed, with correlations of over 99% and a maximum discrepancy of 10% observed respectively. *Android* automation was then developed, calibrated and validated with similar results.

The results obtained in this research show that a consumer smartphone image sensor, fitted with narrow bandpass and neutral density filters, automated using a specifically written app that uses the camera input produces direct UVA irradiances and aerosol optical depth data with comparable accuracy to that obtained from more expensive and specialised equipment, with correlations of over 0.98 and discrepancies only up to 4%. Such an outcome can promote a greater spatial resolution in monitoring UVA irradiance and air quality, allowing a greater awareness of individual UVA exposure and local air quality.

Certification of Dissertation

I certify that the ideas, experimental and field work results, analyses, software and conclusions reported in this dissertation are entirely my own effort, except where otherwise acknowledged. I also certify that the work is original and has not been previously submitted for any other award, except where otherwise acknowledged.

Signature of Damien Igoe

Endorsement

Signature of Professor Alfio Parisi, Principal Supervisor

Signature of Associate Professor Brad Carter, Associate Supervisor

Acknowledgements

First and foremost, I wish to extend my utmost gratitude and genuine admiration for my Principal Supervisor, Professor Alfio Parisi, and my Associate Supervisor, Associate Professor Brad Carter – Their knowledge, patience, wisdom and kindness have been unparalleled, how they dealt with me as their student would be the subject of another thesis.

Many thanks are also extended to Dr. Leigh Brookshaw, whose expertise in and passion for Android programming assisted greatly. Also, gratitude is extended to Oliver Kinder, of the Faculty of Sciences workshop, whose expertise and dedication are appreciated.

The participants of the question and answer website, StackOverflow.com have kindly assisted me in understanding the structure and techniques of Android programming.

Thanks are also extended to owners of the private residences in Emerald and Plainland, Queensland for allowing me to conduct observations in their backyards. A special thanks goes to their pet dogs for keeping me company throughout the 3 hour experiments.

Finally, a big thanks is extended to my parents whose encouragement, tolerance and humour saw me through many bad times when I “hit a wall” in the research.

Contents

List of Figures

List of Tables

1. Introduction

1.1 Rationale

The measurement of the optical effects of atmospheric aerosols is critical in solar UV (290 nm to 400 nm) studies, particularly when measured from the surface, as variations in the amount and types of aerosols present a major source of uncertainty in the modelling of the solar UV. Most aerosols, whether originating from natural or artificial sources attenuate UV wavelengths to varying degrees (Mitchell et al. 2010; Radhi et al. 2010; Leitzell 2008; Kokhanovsky 2008; Kalashnikova et al. 2007; Rosales et al. 2006; Parisi et al. 2004; Meloni et al. 2003; Mitchell and Forgan 2003; Dubovik et al. 2002; Lenoble et al. 2002; Torres et al. 2002; Morys et al. 2001; Wenny et al. 2001; Horvath 1993). Changes in UV radiation are of major concern for human health, agriculture, ecosystems and terrestrial and aquatic vegetation and so requires an improved understanding (Anton et al. 2009; Ialongo et al. 2008; Kokhanovsky 2008; Paulos et al. 2007; Kalashnikova et al. 2005; Parisi et al. 2004; Meloni et al. 2003; Dubovik et al. 2002; Lenoble et al. 2002; Torres et al. 2002; Wenny et al. 2001; Bigelow et al. 1998).

Australia generally has very low aerosol loading, particularly in rural areas (Mitchell et al. 2010; Radhi et al. 2010; Leitzell 2008; Kalashnikova et al. 2005; Mitchell and Forgan 2003). However, many areas of northern Australia experience elevated aerosol levels due to biomass burning during spring (Kalashnikova et al. 2005). For parts of the inland Eastern Australia region, the Lake Eyre basin is a major source of seasonal mineral aerosol during the spring, summer and autumn (Mitchell et al. 2010; Radhi et al. 2010). In comparison, aerosol loading is generally at its lowest during winter (Mitchell et al. 2010; Kalashnikova et al. 2005).

The most common methods to measure aerosol optical depth are satellite observations and specialised ground based equipment, including sunphotometers and sky radiometers (Mitchell et al. 2010; Radhi et al. 2010; Ialongo et al. 2008; Parisi et al. 2004; Queface et al. 2003; Morys et al. 2001). This ground-based equipment is often expensive, heavy and large, hence inaccessible to the wider community and schools (Morys et al. 2001). One of the most portable means of measurement is the hand held Microtops sunphotometer (Morys et al. 2001). However, the cost of the sunphotometer places this out of reach of schools and the general public.

Complementary metal oxide semiconductor (CMOS) image sensors have been in ‘off the shelf’ applications for many years (Hoffman et al. 2005). In recent years, there have been improvements in smartphone camera design, particularly with backside illumination (BSI) and back thinning (PhysOrg 2011; Scott 2011;). Backside illumination is where image sensor pixel circuitry is placed ‘behind’ the silicon photodiode (Scott 2011). The silicon photodiode is then ground down or ‘back thinned’ allowing increased sensitivity to shorter wavelengths, including UV (PhysOrg 2011; Scott 2011).

In recent years, the development and use of smartphones have surged to become the dominant type of mobile phone (Perna 2010). Smartphones often employ the Android programming platform, thus providing multifaceted functions that can either be downloaded, often for free, or written using various emulators found online. Smartphone imaging technology and the Android operating system have been recently used in complex applications, including medical, architectural and air visibility studies (Poduri et al. 2010; Breslauer et al. 2009). The combination of imaging and communication technology, alongside accessibility and ease of use has made the smartphone a prudent choice to allow greater community involvement, hence understanding of scientific applications (Westly 2009; Paulos et al. 2007). Smartphones are thus the technology of choice for this study due to their growing ubiquity and ease-of-use of the integrated communications and image sensing technologies (Westly 2009; Avvenuti and Vecchio 2008; Paulos et al. 2007).

1.2 Hypothesis

This dissertation aims to test the hypothesis that smartphone cameras coupled with narrow-band UV filters can be used to quantify the total UVA direct irradiance and the UV aerosol optical depth.

Smartphone and digital camera image sensors are inherently sensitive to UV wavelengths. Recent innovations in sensor architecture have sought to improve high energy incident light sensitivity, particularly with smartphones. The use of mass market devices such as phone and digital cameras provide an accessible means for widespread UVA aerosol optical depth monitoring at a far greater global spatial resolution than traditional means, coupled with greater community awareness and involvement.

1.3 Objectives

This study focuses on delivering low-cost, easy-to-use solar UVA measurements using smartphones, to enable widespread UVA aerosol optical depth monitoring. UV aerosol optical depth (AOD) is a measure of the relative attenuation of incident solar UV irradiances (Bodhaine et al. 1999).

Smartphones will be developed as AOD sensing devices by:

- Testing and evaluating the smartphone image sensor's ability to detect UVA radiation. This follows on from an investigation by Tetley and Young (2008) that determined that it is possible for standard mass-market image sensors to detect UV radiation.
- Characterising the image sensor's intensity (grayscale) response to increasing direct irradiance at discrete UVA wavelengths, using both artificial (monochromator) and natural (solar) UV sources.
- Calibrating the image sensor intensity response with respect to direct UVA irradiance, with the use of a sunphotometer for solar measuements.
- Validating the calibrated image sensor intensity response to ensure the correct mathematical relationship exists between this and the incident irradiation.
- Calibration and validation of UVA aerosol optical depth at 340 nm and 380 nm.
- Design and validation of an Android app for the automation of the UVA direct irradiance and UVA aerosol optical depth measurements on a smartphone.

The research offers a means to further improve the accuracy of UV models, through the potential of a wider network of AOD measurements, with the use of prolific smartphones. The availability of this capability on a smartphone system makes aerosol optical depth measurements accessible to the wider community, particularly schools.

The overall objectives for this research are:

1. Determining the feasibility and extent that a smartphone camera can detect useful UV readings throughout the UVA waveband, particularly the focus wavelengths for AOD measurements of 340 nm and 380 nm.
2. Developing and testing of a system using the smartphone’s sensor array alongside the Android platform to obtain reliable and useful UVA aerosol optical depth.
3. Design and testing of a smartphone system that makes use of the sensor and Android platform capabilities to be used by the general public, particularly schools, for UV aerosol optical depth measurements.

1.4 Dissertation Outline

- Chapter 2 provides an overview of the properties of UV radiation, atmospheric attenuation and its effects on the biosphere and on human health.
- Chapter 3 details an overview of how aerosols, both anthropogenic and natural, attenuate incoming solar radiation in the visible and ultraviolet wavelengths.
- Chapter 4 gives a description of current standard aerosol and UV measurement equipment, calibration requirements and techniques. These are compared and contrasted with smartphone image sensors. Finally, an analysis of image sensor noise is presented.
- Laboratory tests, including smartphone image sensor characterisation and lens and filter transmission in the UV waveband are detailed in Chapter 5. Also in this chapter are field calibration and verification tests of UVA direct irradiance and UVA aerosol optical depth from selected smartphones in comparison with a sunphotometer.
- *Android* algorithm development and testing are presented in Chapter 6. This chapter also discusses the independent modules needed and how they are linked. The validity of this algorithm for UVA direct irradiance and UVA aerosol optical depth is tested and compared with a sunphotometer.

2. Solar UV

2.1 What is Ultraviolet Radiation?

Ultraviolet (UV) radiations are wavelengths of light starting from the boundary of ionizing and non-ionizing radiation at 100 nm to the boundary with the visible spectrum at 400 nm (Jegou et al. 2011; Parisi et al. 2004; Soehnge et al. 1997). UV radiation is non-ionizing radiation with shorter wavelengths and greater energy per photon than visible and infra-red light (Soehnge et al. 1997). The UV waveband is divided further, as shown in Figure 1, the specific waveband of interest in this research is UVA (320 nm – 400 nm).

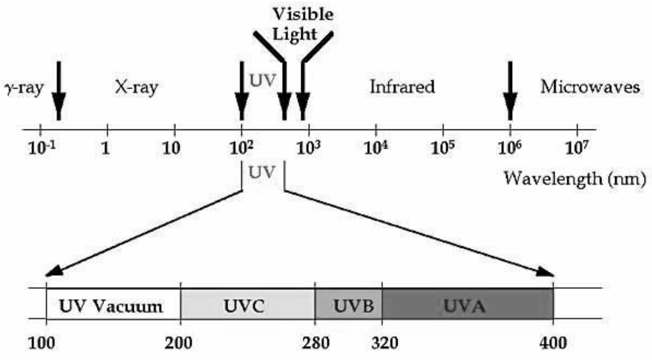

Figure 1: The gamma ray to microwave portion of the electromagnetic spectrum, with emphasis on the ultraviolet (UV) wavebands (Soehnge et al. 1997).

The boundary between UVB and UVA is defined by the CIE (International Commission on Illumination) as being at 315 nm (WHO, 2012); however, there is a lot of research, particularly photobiology that suggests that the boundary needs to be at 320 nm, as there is still appreciable absorption by ozone up to that point (Kollias et al. 2011; Parisi et al. 2004; Diffey, 2002). In this research, the wavelength of 320 nm will be used as the boundary between UVA and UVB. Vacuum UV is absorbed by a few centimetres of air and is often included as part of the germicidal UVC (Parisi et al. 2004; Wang et al. 2001).

2.2 Ultraviolet Radiation in the Atmosphere

All wavebands of ultraviolet radiation emanate from the sun, but not all reach the Earth's surface. Solar UV wavelengths up to approximately 295 nm (UVC and some UVB) are absorbed by the atmosphere's diatomic oxygen (O_2) and ozone (O_3), as can be seen in a sample clear sky solar UV spectrum at a solar zenith angle of 11.2° (Figure 2). The dips in the curve are due to Fraunhofer absorption (Jegou et al. 2011; Young, 2009; Parisi et al. 2004). Despite UVB being heavily absorbed by ozone and being strongly scattered by atmospheric molecules, a small proportion still reaches the Earth's surface (Jegou et al. 2011; Seinfeld and Pandis, 2006; Parisi et al. 2004). UVA radiation accounts for approximately 90-95% of UV radiation reaching the Earth's surface (Jegou et al. 2011; Parisi et al. 2004; Wang et al. 2001).

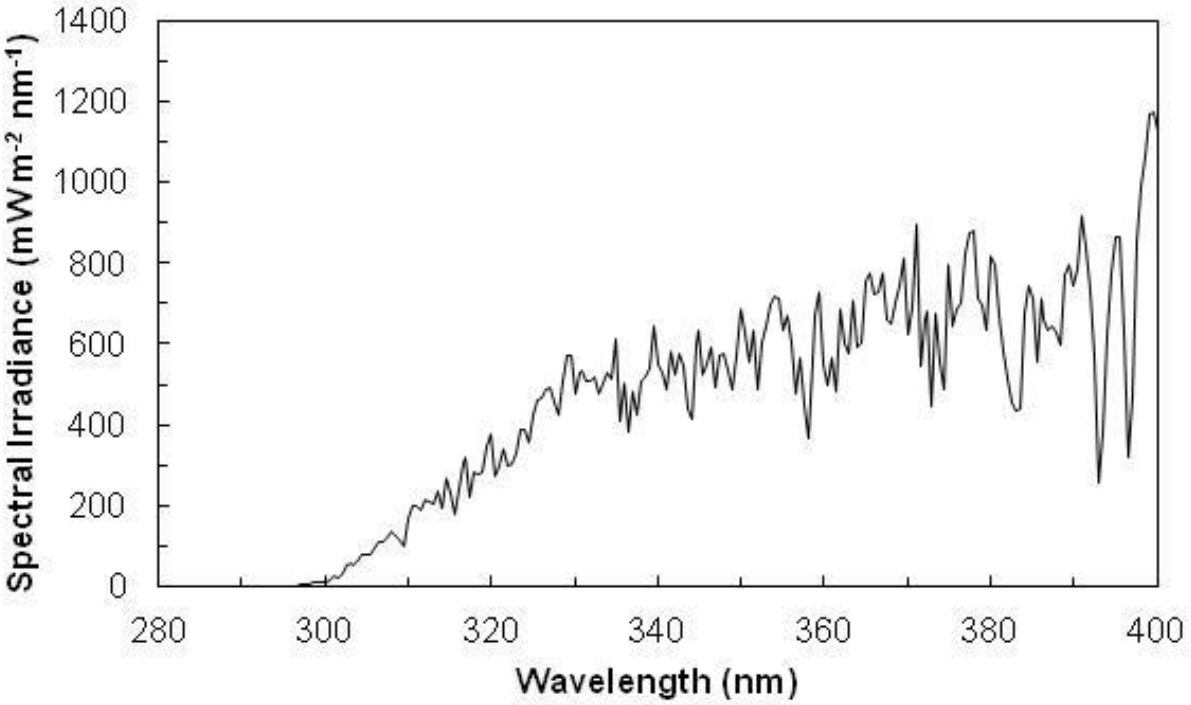

Figure 2: Example of solar UV spectrum data collected by a Bentham DmC300 spectroradiometer on a clear day for a solar zenith angle of 11.2°. The troughs in the data are due to atmospheric Fraunhofer absorption.

Ozone absorption is divided into 4 phases that approximately correspond to the UVB (Hartley), UVA (Huggins), visible (Chappuis) and infrared (Wulf) wavebands (Orphal, 2003). The least absorption occurs near 380 nm and throughout most of the UVA waveband, resulting in UVA being relatively insensitive to ozone layer fluctuations (Figure 3).

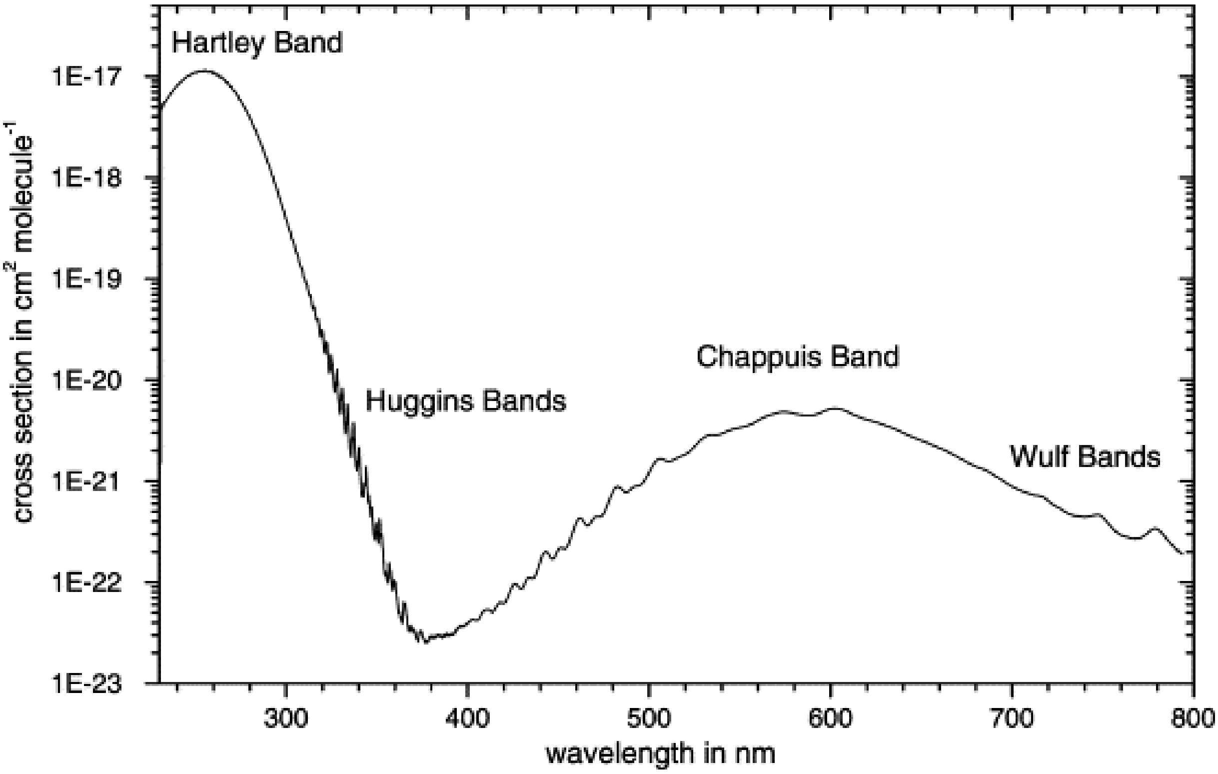

Figure 3: Labelled sections of the ozone absorption cross section spectrum for the UV, visible and infrared wavebands (Orphal, 2003).

The actual amount of UV radiation reaching the Earth's surface is highly dependent on a number of factors including:

- The latitude and altitude of the observation point which affect the intensity of UV radiation (Jegou et al. 2011; Siani et al. 2010; Young, 2009; Siani et al. 2008; Kamran and Khan, 2007; Kimlin, 2008; Parisi et al. 2004: Diffey, 2002; Diffey, 1991).
- The solar zenith angle (SZA) is dependent on the date and time of the day observations are made. The greater the SZA, the greater the air mass or path length through the atmosphere the radiation must traverse. Increasing the path length increases scattering and absorption of UV radiation (Jegou et al. 2011; Siani et al. 2010; Young, 2009; Kimlin, 2008; Siani et al. 2008; Parisi et al. 2004; Diffey, 2002; Diffey, 1991).
- Absorption and scattering due to aerosols and clouds, affecting the measured intensity of UV, particularly as the aerosol and gaseous component is not visible to the naked eye (Jegou et al. 2011; Young, 2009; Kimlin, 2008; Parisi et al. 2004: Meloni et al. 2003; Diffey, 2002; Diffey, 1991).
- Molecular or Rayleigh scattering due to the chemical constituents of the atmosphere, primarily nitrogen and oxygen gas (Jegou et al. 2011; Young, 2009; Kimlin, 2008; Parisi et al. 2004: Meloni et al. 2003; Diffey, 2002; Diffey, 1991).
- Reflection off the horizontal and vertical surfaces and surrounding structures (Turner and Parisi, 2009; Parisi et al. 2004; Diffey, 2002; Diffey, 1991).

- Earth-sun distance, as the Earth is closest to the sun during the Southern Hemisphere summer, UV irradances can be up to 15% higher than those experienced in a similar Northern Hemisphere location (Gies et al. 2004; Gies, 2003).

2.3 Effects of Ultraviolet Radiation on the Biosphere

Ultraviolet radiation is a critical component in the stability of biogeochemical cycles and ecosystems (Zlater et al. 2012; Ballare et al. 2011; Zepp et al. 2011; Hader et al. 2007). Most research with these interactions focuses on the ozone induced fluctuations in UVB radiation reaching the Earth’s surface, which plants are sensitive to due to being immobile (Ballare et al 2011; Reddy et al. 2010). A critical factor is that plant cell proteins and DNA strongly absorb UVB resulting in photoexcitation and potential damage in these structures (Lidon et al. 2012; Zlater et al. 2012; Ballare et al. 2011; Piri et al. 2011; Reddy et al. 2010; Diffey, 1991). Plant species respond differently, some benefit from greater UV exposure, whereas some are unaffected, depending on any inherent UVB protection adaptation; however, many species are negatively affected, including food crops (Lidon et al. 2012; Piri et al. 2011; Reddy et al. 2010; Kakani et al. 2003; Webb, 1998; Diffey, 1991).

Increased and prolonged UVB exposure can result in the breakdown of chloroplasts and a decrease in the quantity of chlorphyll corresponding with an increase in UVB absorbing material (Lidon et al. 2012; Piri et al. 2011; Kakani et al. 2003). Structurally, UVB exposure can result in decreased water use efficiency, leaf area and plant height (Piri et al. 2011; Diffey, 1991). These influences result in a decrease in photosynthesis, affecting other processes including respiration, plant development and reproduction, all critical particularly for agricultural yield (Reddy et al. 2010; Kakani et al. 2003).

Research has indicated that increased UVB radiation results in a strong negative influence on aquatic species and ecosystems, particularly at the base level producers, such as phytoplankton (Hader et al. 2011; Diffey, 1991). Phytoplankton reacts to increased UVB radiation by moving downward in the water column, this results in less photosynthesis as deeper water is darker (Diffey, 1991). In this way, animals are indirectly affected by disruptions in the food chain (Ballare et al. 2011; Hader et al. 2011). Fish in shallow aquaculture environments have also exhibited skin lesions and cataracts from prolonged UV exposure (Webb, 1998).

Animal species are also directly affected by prolonged and changing UV exposure (Hader et al. 2011). There are several parallels between UV exposure effects on many mammalian species and humans (Webb, 1998). Domestic animals have exhibited squamous cell carcinomas on the eyes and unpigmented nostrils, lips and ears due to prolonged UV radiation exposure (Cullen et al. 2002; Webb, 1998). UV radiation immune deficiencies, cataracts and bone metabolism have been found to occur in many species of animals, particularly mammals (Hockwin et al. 1999; Webb, 1998).

2.4 Effects of Ultraviolet Radiation on Human Health

UVB has the shortest wavelengths, hence greatest energy per photon of the solar UV radiation reaching the Earth’s surface, with significant implications for human health (Webb, 1998). UVA, while having longer wavelengths and less energy per photon than UVB constitutes the vast majority of UV radiation humans are exposed to (Zhang et al. 2012; Agar et al. 2004; Berneburg et al. 2000; Krutmann, 2000).

UVA can penetrate deeper into the skin than UVB and can also pass through most non-tinted glass windows and cotton clothing (depending on the tightness of the weave), whereas generally, these objects are opaque to UVB (Jegou et al. 2011; Agar et al. 2004; Parisi et al. 2004; Wang et al. 2001). The skin and eyes are the two organs that are exposed to UV radiation, a known carcinogen and linked with premature skin aging and immune system suppression and sun-related eye diseases; however, it is needed to maintain good health (Hung et al. 2012; Jegou et al. 2011; Young, 2009; Kimlin, 2008; Rigel, 2008; Webb, 1998). Melanin production in the upper layers of the skin affords some minor level of photoprotection, but not to prolonged exposure (Yaar and Gilchrest, 2007; Berneburg et al. 2000).

2.4.1 Vitamin D Synthesis

Human exposure to UVB is necessary for the synthesis of cutaneous vitamin D. As such, vitamin D synthesis is highly dependent on solar zenith angle, ozone levels and diurnal, seasonal and geographical variability (McKenzie et al. 2009; Siani et al. 2009; Kimlin, 2008; Grant and Holick, 2005; Parisi et al. 2004). It is recommended that during the Australian summer, depending on skin type, 2-14 minutes, 3-4 times a week to 15% of the body will provide adequate vitamin D; however, as erythema can occur within 8 minutes, this process should occur well before or after solar noon (Samarek et al. 2006).

The process of vitamin D_3 synthesis begins with the photoconversion of 7-dihydrogencholesterol in the skin to become previtamin-D_3, which in turn undergoes a slow heat isomerisation to become vitamin D (Kimlin, 2008; Webb, 1998). The CIE action spectrum for the synthesis of previtamin-D_3 in human skin is presented in Figure 4, showing minimal to nil response in the UVA waveband.

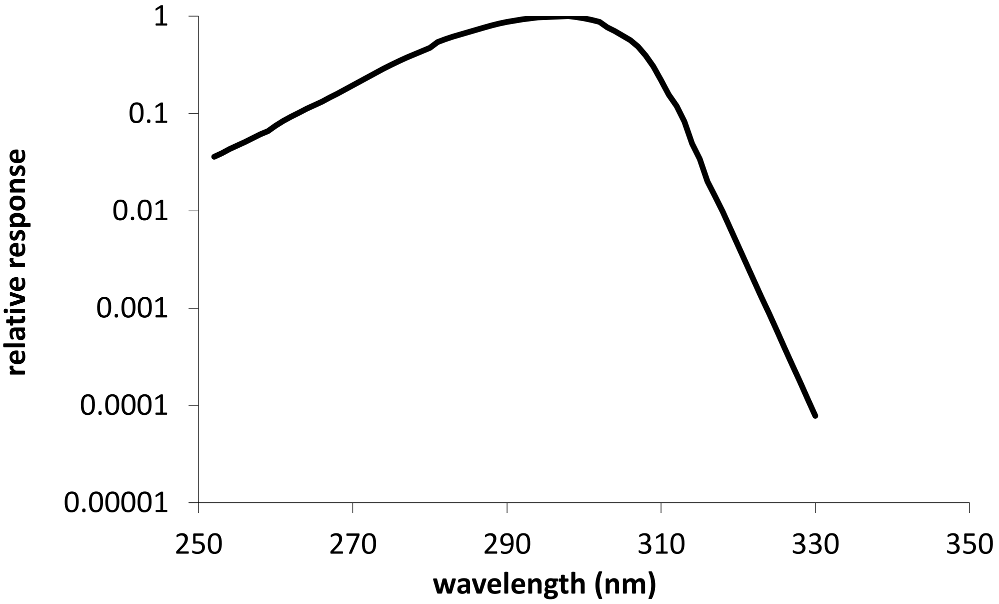

Figure 4: Action spectrum for the synthesis of previtamin-D_3 in human skin (CIE, 2006). The response from wavelengths greater than 330 nm are far lower than what is shown.

One of the main roles of vitamin D is the regulation of calcium absorption (Luk et al. 2012; Kimlin, 2008; Samanek et al. 2006; Webb, 1998). Studies have indicated that vitamin D has a role in the prevention of several types of cancer (Grant, 2008). Deficiencies in vitamin D have been linked with serious conditions such as rickets, bone mass loss, osteoporosis, multiple sclerosis, hypertension, insulin dependent diabetes, schizophrenia, breast cancer, prostate cancer, non-Hodgkin’s lymphoma and colorectal cancer (Kimlin, 2008; Samanek et al. 2006). Some studies reviewed by Luk et al. (2012), suggest that human reproduction may also be affected by vitamin D deficiency.

2.4.2 Skin Cancers

Care is required so as to not expose the skin to excessive UV radiation, as erythema (sunburn) has been found to be less dependent on conditions critical for vitamin D synthesis (McKenzie et al. 2009). Prolonged exposure to UV radiation is linked with three main types of skin cancer, the non-melanoma (NMSC) basal and squamous cell carcinomas and malignant melanoma (Cancer Council Australia, 2012; McKenzie et al. 2009; Samanek et al. 2006; Webb, 1998).

The prevalent notion that UVB is the main cause of skin cancer has been revised, as recent studies have found the UVA, which contributes about 95% of total ultraviolet exposure can penetrate further into the skin than UVB (Fartasch et al. 2012; Zhang et al. 2012; Rigel, 2008; Agar et al. 2004; Moan et al. 1999). UVB is absorbed by DNA, thus resulting in serious damage but penetrates poorly into the skin, whereas UVA reaches further into the skin and is absorbed by other chromophores, potentially generating damaging reactive species (Lund and Timmins, 2007).

Products formed by ultraviolet photosynthesis by melanin in melanocytes, several layers within the skin where UVA wavelengths at a minimum can penetrate to, may activate the carcinogenic processes that lead to melanoma (Lund and Timmins, 2007; Moan et al. 1999). Agar et al. (2004) report that in many skin cancer incidents there is a clear UVA fingerprint mutation, especially in the basal layers and stem cell regions of the skin. Although the exact wavelengths that cause melanoma tumorigenesis in humans is unknown, an analogous action spectrum for fish species of the genus Xiphophorus is used (Setlow et al. 1993). Normalised UV action spectra for erythema and fish melanoma are presented in Figure 5 (CIE, 1998; Setlow et al. 1993), showing a higher relative response in the UVA for the latter.

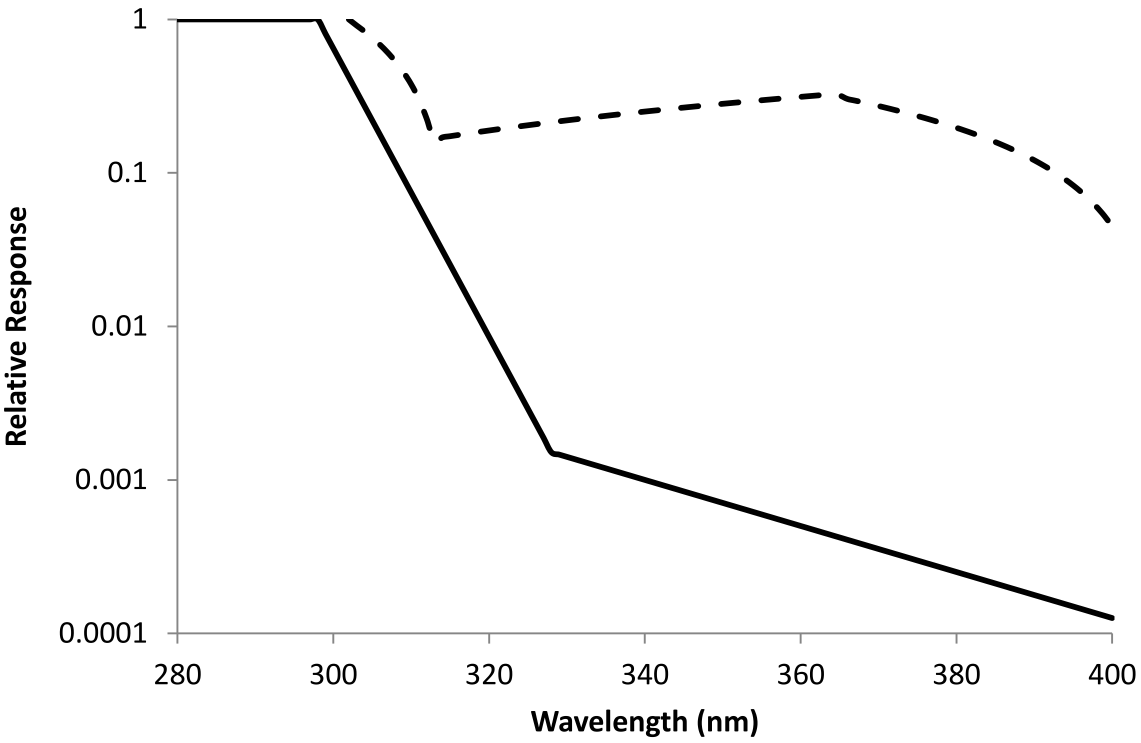

Figure 5: Action spectra for erythema (solid line) and fish melanoma (dashed line) (CIE, 1998; Setlow et al. 1993).

The following statistics from the Cancer Council Australia (2012), SunSmart Victoria (2012) and Fransen et al. (2012) show the significant health problems caused by excessive exposure to UV radiation:

- In general, skin cancers account for about 80% of newly diagnosed cancers, with over 1000 treated per day. About 1890 die each year of skin cancers. Australia has the highest incident rate of skin cancer in the world.
- Non-melanoma skin cancer is the most common type of cancer diagnosed in Australia, with men twice as likely as women to suffer from them.
- Melanoma are more common in men than women, but is ranked as the 3rd most common diagnosed cancer for both sexes, and is the 9th most common cause of cancer death.

2.4.3 Photoaging

Skin aging is the result of either intrinsic or extrinsic mechanisms, such as chronological aging and UV exposure respectively (Hung et al. 2012; Vierkotter and Krutmann, 2012; Yaar and Gilchrest, 2007; Rabe et al. 2006). Although there are many similarities between chronologically aged and photoaged skin, the latter sometimes referred to as ‘premature aging’, there are some fundamental differences in the processes (Rabe et al. 2006; Berneburg et al. 2000). Although lifestyle and skin type are major factors, prolonged exposure to UVA has been found to be the primary cause of photoaging (Vierkotter and Knutmann, 2012; Agar et al. 2004; Rabe et al. 2006; Berneburg et al. 2000; Knutmann, 2000). The action spectrum of photoaging has never been fully determined (Yaar and Gilchrest, 2007).

Laboratory experiments on nude mice and observations made with different groups of people in different environments reveal that prolonged exposure to UVA results in the degradation of elastin and collagen as well as oxidation of skin proteins and lipids, through the formation of reactive oxygen species, resulting in dermal enlargement (wrinkles), variable epidermal thickness, solar elastosis and pigment irregularities (Vierkotter and Knutmann, 2012; Hung et al. 2012; Yaar and Gilchrest, 2007; Rabe et al. 2006; Knutmann, 2000).

Recent studies suggest that UVA indirectly causes mitochondrial DNA mutations through the formation of reactive oxygen species that are a contributing factor to the effects of photoaging (Vierkotter and Knutmann, 2012; Yaar and Gilchrest, 2007; Berneburg et al. 2000). This process of indirect DNA damage due to prolonged exposure to UVA implicates the waveband’s critical role in photocarcinogenesis (Lund and Timmins, 2007; Yaar and Gilchrest, 2007; Rabe et al. 2006).

2.4.4 Eye Conditions

The parts of the eye that are exposed, hence are sensitive to light are the cornea, lens and retina, exposure to these are dependent on the incident angle of the light source (Oliva and Taylor, 2005; Sliney, 2005; Sliney, 2002). Not all wavelengths of incident light actually reaches the eye most of the time (Oliva and Taylor, 2005). Most ultraviolet radiation is absorbed by the cornea and lens. The absorption increases with age and the relative absorption of UV is in Figure 6 (Behar-Cohen et al. 2011; Oliva and Taylor, 2005; Sliney, 2002; Vajdic et al. 2002). The outer components of the eye, including the eyelid and conjunctiva are exposed to UV similar to that of the rest of the skin, potentially increasing the risk of skin cancers as described in section 2.4.2 (Friedlaender, 2005; Oliva and Taylor, 2005).

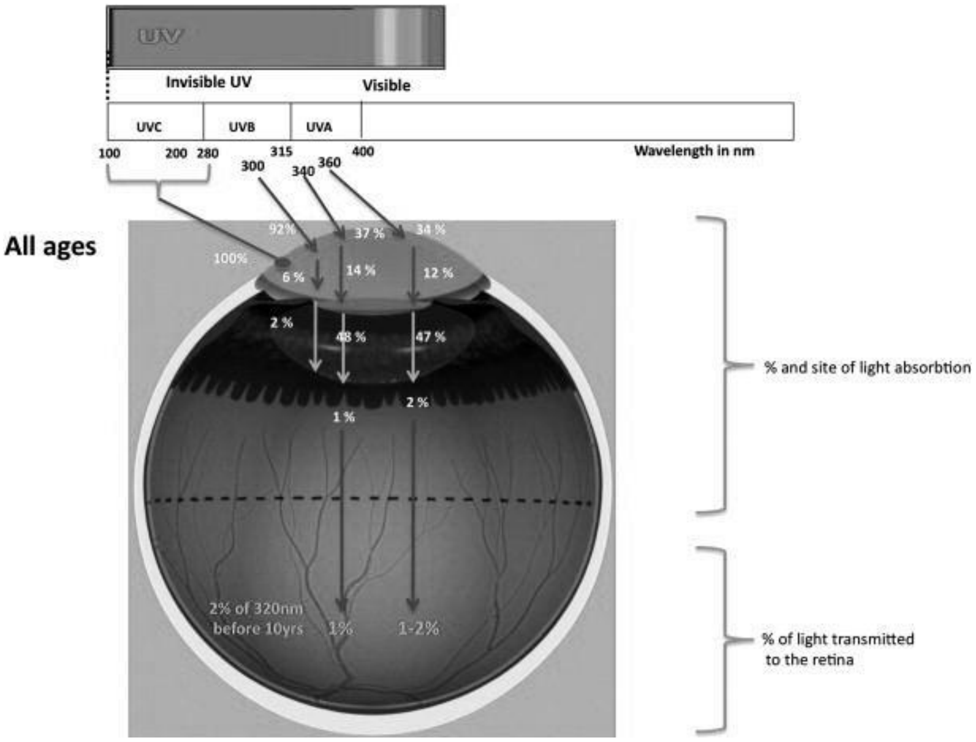

Figure 6: Relative UV absorption and transmission into the human eye (Behar-Cohen et al. 2011).

Most studies state that prolonged exposure to UVB results in serious conditions of the human eye, including cataracts, eyelid, conjunctiva and corneal lesions (Oliva and Taylor, 2005; Zigman, 2005). DNA damage through UVB dosage in these outer areas of the eye is likely to be similar to photo responses that can occur in the human skin (Samarek et al. 2006; Oliva and Taylor, 2005). However, as with skin cancer, DNA damage can be the result of prolonged indirect UVA exposure causing the formation of reactive oxygen species that can result in these conditions, including lens damage cannot be underestimated (Lund and Timmins, 2007; Zigman, 2005).

2.4.5 Immune Response

The lack of vitamin D can lead to several conditions concerning the immune system (Kimlin, 2008; Samanek et al. 2006). Prolonged exposure to both UVA and UVB radiation is implicated in local and systemic immunosuppression (Yaar and Gilchrest, 2007; Rabe et al. 2006; Webb, 1998). Studies indicate that immunosuppression of UV radiated skin occurs due to immune cell DNA damage and is thought to play a role in the development of non-melanoma skin cancer (Fartasch et al. 2012; Lund and Timmins, 2007; Berneburg et al. 2000). Localised UV cell mediated immunosuppression in the eye can lead to an increase in incidents of infections (Oliva and Taylor, 2005).

2.5 Chapter Discussion

This chapter demonstrated why the study of ultraviolet wavelengths is critical for human health, particularly of the skin and eyes; the ecosystem, both aquatic and terrestrial and for understanding the chemistry and structure of the atmosphere. In order to fully quantify ultraviolet radiance at the surface, all attenuating factors need to be carefully quantified, in particular, ozone, clouds and air pollution. Chapter 3 focuses on the aerosols that cause air pollution and uncertainty in UV models. In addition, some recent studies have shown that air pollution is a contributing factor to skin aging in a similar manner to photoaging (Vierkotter and Knutmann, 2012).

3. Aerosols

The causes, extent and consequences of air pollution due to atmospheric aerosols are of fundamental interest (Mitchell et al. 2010; Radhi et al. 2010; Kalashnikova et al. 2007). Aerosols can be of natural or anthropogenic origin and can be organic or inorganic and can be generated from the surface or through gas to particle conversions (Kokhanovsky, 2008; Seinfeld and Pandis, 2006; Jacobson, 2002). Aerosols are typically around 100 nm in size, although not visible to the human eye, their effects can be seen with changes in visibility, climatic influences and their potential to cause health problems in humans (Kokhanovsky, 2008; Jacobson, 2002). This chapter discusses the optical properties and the global and local aerosol loading.

3.1 Attenuation of Radiation due to Aerosols

The optical properties of aerosols are dependent on their size, shape, concentration, chemical composition and internal structure (Kokhanovsky, 2008; Seinfeld and Pandis, 2006). The attenuation of radiation due to aerosols is highly variable and can be due to absorption and scattering (Kokhanovsky, 2008). Aerosol loading can decrease the erythemally weighted UV measured at the surface and therefore the UV Index (Wenny et al. 2001). Aerosol optical depth (AOD) is a dimensionless quantity that describes the attenuation of incident light due to aerosol particles (Kokhanovsky, 2008; Jacobson, 2002). The Beer Lambert Law is used to measure the direct normal irradiance at wavelength λ (I_λ) and is given by (Wenny et al. 2001; Bodhaine et al. 1999),

$$I_\lambda = I_{0\lambda}\, e^{-m\tau_\lambda \frac{P}{P_0}}. \qquad [1]$$

Where $I_{0\lambda}$ is the extraterrestrial irradiance at wavelength λ and is usually determined using the Langley Method (Meloni et al. 2003; Bigelow et al. 1998; Bodhaine et al. 1999; Harrison and Michalsky, 1994). The terms m, τ_λ, P and P_0 represent air mass, total optical depth, station pressure and mean sea level pressure respectively, these will be described in more detail later in this section.

The Langley Method for measuring extraterrestrial irradiance assumes that the Beer-Lambert Law provides a negative linear relationship between the natural log of the direct normal irradiance ($\ln I_\lambda$) and relative air mass (m), assuming that the atmospheric composition ($-k$) remains constant; namely (Adler-Golden and Slusser, 2007),

$$\ln I_\lambda = \ln I_{0\lambda} - km. \qquad [2]$$

The natural log of the extraterrestrial irradiance is determined when the linear plot is extrapolated to the vertical axis, (Adler-Golden and Slusser, 2007; Meloni et al. 2003). The extraterrestrial irradiance needs to be corrected for the mean Sun Earth distance factor $\left[\left(\frac{d_m}{d}\right)^2\right]$, calculated using the calendar day of observation (doy) (Porter et al. 2001),

$$\left(\frac{d_m}{d}\right)^2 = \{1 - 0.01673\cos[0.017201(doy - 4)]\}^{-2}. \qquad [3]$$

The handheld Microtops II sunphotometer is an example of an instrument that is calibrated in this way, with the mean sun-Earth distance extraterrestrial irradiation programmed into the device for use as a ‘factory constant’ (Solar Light, n.d.; Morys et al. 2001).

In the case for instruments where the extraterrestrial irradiance is set, the direct normal irradiance needs to be corrected with the Earth-sun difference factor, derived from equation 3,

$$\left(\frac{d}{d_m}\right)^2 = \{1 - 0.01673\cos[0.017201(doy - 4)]\}^2. \qquad [4]$$

m is the relative air mass. The atmosphere can be assumed to be plane parallel for a relative air mass (m) of less than 2 which corresponds with solar viewing at midday, with an error margin less than 0.1% (McIntosh, 2006). However, this assumption does not apply to all latitudes. This assumption results in a simplified air mass equation where the angle (θ) is the solar zenith angle (Wenny et al. 2001),

$$m = \sec\theta. \qquad [5]$$

τ_λ is the total optical depth, comprising the Rayleigh (molecular), ozone and aerosol optical depths (Bodhaine et al. 1999),

$$\tau_\lambda = \tau_{Rayleigh} + \tau_{Ozone} + \mathrm{AOD}. \qquad [6]$$

At the target wavelengths of this research (340 nm and 380 nm), ozone absorption is negligible, thus the term τ_{Ozone} can be assumed to be zero.

$\frac{P}{P_0}$ is the ratio of the station air pressure with mean sea level air pressure (1013.25 hPa).

Rearranging equation 1 and including the assumptions above, to make the aerosol optical depth the subject yields (adapted from Morys et al. 2001),

$$\mathrm{AOD} = \frac{1}{m}\left[\ln(I_{0\lambda}) - \ln\left(I_\lambda \cdot \left(\frac{d}{d_m}\right)^2\right)\right] - \tau_{Rayleigh} \cdot \frac{P}{P_0}. \qquad [7]$$

3.1.1 Visible

Very few aerosols and atmospheric gases absorb in the visible spectrum, mainly in the blue region (Igoe, 2011; Kokhanovsky, 2008; Horvath, 1993). Primarily, elemental carbon particularly in the form of soot, iron oxides often found in volcanic ash; and gaseous nitrogen dioxide are the main contributors to visible light attenuation, sky discoloration and loss of visibility (Igoe, 2011; Kokhanovsky, 2008; Yamanoi et al. 2008; Gangl et al. 2007; Schnaiter et al. 2003; Horvath, 1993). Some gaseous species, such as sulphur dioxide, that do not cause appreciable attenuation in the visible spectrum can microlens, or focus the absorption when in contact with soot (Schnaiter et al. 2003).

3.1.2 Ultraviolet

Aerosols are a major cause of UV trends due to stratospheric changes being obscured due to solar radiation being modified as it passes through aerosols present in the atmosphere (Mitchell et al. 2010; Siani et al. 2010; Leitzell, 2008; Lenoble et al. 2002; Wenny et al. 2001; Horvath, 1993). The inhomogeneous and variable nature of aerosols poses significant difficulties in attaining accurate UV and global radiation models (Radhi et al. 2010; Siani et al. 2010; Kokhanovsky, 2008; Kalashnikova et al. 2007). Aerosols and atmospheric gases attenuate the incident extrasolar UV radiation through scattering and absorption processes (Mitchell et al. 2010; Radhi et al. 2010; Siani et al. 2010; Mitchell and Forgan, 2003; Torres et al. 2002; Horvath, 1993). Examples that cause attenuation by scattering include gaseous species such as anthropogenic ozone, sulphur dioxide and nitrogen dioxide (Siani et al. 2010; Westly, 2009; Yabe et al. 2003; Horvath, 1993; Platt et al. 1979). Particulate aerosols such as soot, organic material, mineral dust, haematite and sea salt attenuate UV through scattering and absorption (Yabe et al. 2003; Dubovik et al. 2002; Horvath, 1993).

3.2 Aerosol and Gaseous Species

Although it is beyond the scope of this research to be able to differentiate between different aerosol and gaseous species, the following is a summary of the optical properties of the most common aerosols and gaseous species: anthropogenic ozone, nitrogen dioxide, sulphur dioxide and particulate matter, from multiple sources adding to the complexity of measuring AOD (Kokhanovsky, 2008; Kazadzis et al. 2007).

Natural sources of aerosols and gaseous species include volcanic eruptions, sea spray and dust storms. Anthropogenic or manmade aerosol based air pollution primarily derives from industry, transport, agriculture and forest fires (Jacobson, 2002). The effects of air pollution are of concern to human health, particularly in urban areas (Igoe, 2011; Kokhanovsky, 2008; Seinfeld and Pandis, 2006; Jacobson, 2002). It is not uncommon for many different sources contributing different types of aerosols, which may result, with the influence of ambient UV radiation, in the formation of secondary aerosols (Kokhanovsky, 2008). A summary of the interaction between UV and some of the major types of aerosols is presented below.

Anthropogenic Ozone

Anthropogenic ozone is one of the main constituent of photochemical haze and one of the two main gaseous species that affect the UVB waveband (Siani et al. 2010; Seinfeld and Pandis, 2006; Wayne and Wayne, 2005; Fioletov et al. 1998). Studies in Mexico City have indicated a strong relationship between less UVB flux reaching the surface with increased levels of anthropogenic ozone (Galindo et al. 1995).

Sulphur Dioxide

Sulphur dioxide is the other gaseous species that affects UVB wavebands, and is almost transparent in the visible (Siani et al. 2010; Seinfeld and Pandis, 2006; Fioletov et al. 1998). Sulphur dioxide is the most common anthropogenic sulphur based aerosol, and the most detected naturally emanating from volcanoes (Kokhnovsky, 2008; Seinfeld and Pandis, 2006; Fioletov et al. 1998).

Nitrogen Dioxide

Nitrogen dioxide is the most common and visible of the nitrogen oxide gaseous species and one of the main discolorants in photochemical smog (Siani et al. 2010; Seinfeld and Pandis, 2006; Wayne and Wayne, 2005). Nitrogen dioxide is unique in that it has absorbance features across the UV and visible wavebands, between 300 nm and 370 nm and 90% will dissociate into nitrogen oxide and oxygen. Dissociation drops off significantly between 370 nm and 420 nm (Kokhanovsky, 2008; Seinfeld and Pandis, 2006; Jacobson, 2002).

Particulate Matter

Most particulate matter are weak absorbers of UV wavebands; many, including sea salt and mineral dust, have optical properties that are difficult to characterise due to the aerosol varying composition, morphologies and sizes (Kokhanovsky, 2008; Meloni et al. 2003; Jacobson, 2002). Black carbon, hematite, aluminium oxide and most organic matter strongly absorb UV wavebands (Kokhanovsky, 2008; Jacobson, 2002).

3.3 Aerosols over Australia

The Australian environment has relatively low anthropogenic aerosol loading for an industrialised nation, but is the southern hemisphere's greatest source of mineral dust aerosol. The Lake Eyre Basin (Figure 7) is the main source of dust aerosols (Radhi et al. 2012). Sea salt and seasonal biomass burning aerosols are also prevalent (Radhi et al. 2012; Kalashnikova et al. 2005; Mitchell and Forgan, 2003). Australia has very high levels of UV radiation in the spring and summer due to the latitude of the continent and the relative low aerosol loading (Kalashnikova et al. 2005). Increased UV radiation also leads to the production of secondary aerosols (Radhi et al. 2012).

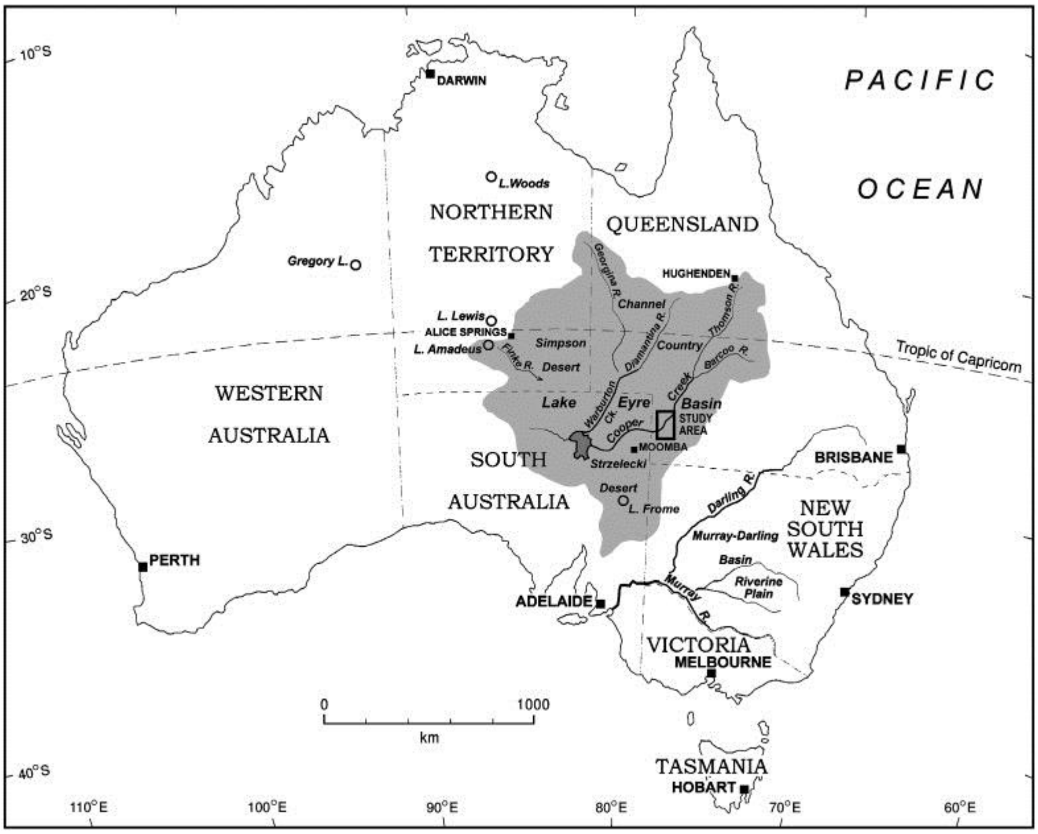

Figure 7: Map of the Lake Eyre Basin being the main source of dust aerosols in Australia (Radhi et al. 2012; Maroulis et al. 2007).

An increase in mineral dust aerosols were recorded after prolonged drought conditions (Radhi et al. 2012). Variability in different types of aerosol loading is primarily due to seasonality, meteorological conditions and the source location (Mitchell et al. 2010).

3.4 Chapter Discussion

Aerosols, both natural and anthropogenic, play a major role in determining the amount of UV radiation reaching the Earth's surface. The attenuation of UV radiation is known as aerosol optical depth and is a critical component of the Beer-Lambert Law which describes the relationship between irradiance and the amount of aerosols. Australia is unique in that generally, the aerosol loading is low but measurable. The next chapter looks at the current detection techniques and how current digital imaging technology can be used to supplement the current methods.

4. Measurement

4.1 Current Measurement Techniques

Measurements of aerosols are usually made using satellite and ground based instrumentation. These instruments are further divided into passive and active sensors. Passive methods provide values that represent the average aerosol properties across the light path or column, whereas active sensors measure the active aerosol profile using photon backscattering (Kokhanovsky, 2008; Diner et al. 2004). Passive and active sensors are often most effectively used in tandem as no one method would be able to fully encapsulate the complexity of aerosol systems (Ialongo et al. 2008; Diner et al. 2004).

There are numerous satellite aerosol observation programs, advantages of these are that they can be timely and provide a global picture of aerosol behaviour and movement and not require Langley calibration, as they provide values of the extraterrestrial irradiance (Kokhanovsky, 2008). Typical resolutions range from 40 km by 320 km for the Global Ozone Monitoring Experiment (GOME) to 13 km by 24 km for the Ozone Monitoring Instrument (OMI) (Lohberger et al. 2004). The large scale resolution of satellite imagery and the fact that land and sea surfaces provide differing responses are a major disadvantage for localised and detailed aerosol measurements (Kokhanovsky, 2008). As satellite data becomes more refined and the resolution size decreases, a more refined and accurate measure of AOD can be determined (Slusser et al. 2000).

Ground based aerosol measurements are also made through a mix of passive and active methods (Kokhanovsky, 2008). The passive methods used for satellite based observations rely on backscattered data, whereas for ground based observations, the data is forward scattered. Similarly, for active sensing, satellite data is single track, whereas ground based is from a point source (Diner et al. 2004). Ground based data needs to have the extraterrestrial irradiance determined using the Langley Plot method described in equation 2 (Kokhanovsky, 2008; Adler-Golden and Slusser, 2007; Estelles et al. 2007; Cheymol et al. 2006; Mitchell and Forgan, 2003; Slusser et al. 2000; Harrison and Michalsky, 1994).

Dobson and Brewer spectrophotometers are the best known ground based aerosol measurement tools and are often the basis of calibrating other equipment (Cheymol et al. 2009; Ialongo et al. 2008; Gao et al. 2001; Morys et al. 2001; Kohler, 1999; Slusser et al. 1999). The Dobson spectrophotometer is a double prism monochromator and the later designed Brewer is a single grating spectrophotometer (Slusser et al. 1999). Despite being a standard for ozone and aerosol measurement, Dobson and Brewer spectrophotometers are largely inaccessible to most people, due to their size and cost (Morys et al. 2001; Kohler, 1999).

The CIMEL CE318 sunphotometer is a common instrument used in Australia’s CSIRO Aerosol Ground Station Network (AGSNet), which forms part of the international program AERONET (Mitchell et al. 2010; Radhi et al. 2010; Kokhanovsky, 2008; Mitchell and Forgan, 2003). Many AGSNet locations are within the Lake Eyre Basin, the major source of mineral dust in Australia (Mitchell et al. 2010; Mitchell and Forgan, 2003). The CIMEL CE318 sunphotometer is designed to be a solar powered, weather proof, automated means of measuring solar and sky irradiances (Cheymol et al. 2009; Kokhanovsky, 2008; Estelle et al. 2007).

The Multi-filter rotating shadow-band radiometer (MFRSR) is an instrument that uses independent filter photodiode detectors to measure spectrally resolved direct and diffuse solar horizontal radiation (Bigelow et al. 1998; Harrison et al. 1994;

Harrison and Michalsky, 1994). The instrument has an automated rotating shadow band (Harrison et al. 2004). The MFRSR is also used throughout AGSNet sites where it can be left to run automatically (Mitchell and Forgan, 2003; Slusser et al. 1999; Bigelow et al. 1998). Tests performed by di Sarra et al. (2002) and Gao et al. (2001) determined that the MFRSR has a high level of accuracy, comparable to Dobson and Brewer spectrophotometers. Both the CIMEL and MFRSR are examples of specialised instrumentation; however, they both are too large and expensive for anything other than specialised research locations and personnel (Kohler, 1999).

LIDAR (Light Ranging and Detection) is an example of an active monitoring system that is commonly used in aerosol studies (Tsaknakis et al. 2011; Kokhanovsky, 2008; Lohberger et al. 2004; di Sarra et al. 2002). Information about the vertical aerosol profile is obtained from backscattered photons (Tsaknakis et al. 2011; Kokhanovsky, 2008; Diner et al. 2004).

The Microtops II sunphotometer is a less expensive and far more portable passive direct sun irradiance measurement tool (Morys et al. 2001; Porter et al. 2001; Kohler, 1999). This instrument also has an array of inbuilt meteorological sensors, particularly a barometer (Morys et al. 2001; Porter et al. 2001) The handheld device has the mean Sun-Earth extraterrestrial irradiance programmed in, from calibrations performed at Mauna Loa Observatory; incident irradiation is corrected for Sun-Earth distance (Morys et al. 2001; Porter et al. 201; Kohler, 1999). Comparisons made with the Dobson and Brewer spectrophotometers by Morys et al. (2001) found that the measurements are comparable with agreement between instruments at ±1% (Kohler, 1999).

The costs and complexity of all traditional equipment mean that they are inaccessible to the general community and schools. However, mass market, accessible and inexpensive technology, including digital cameras and smartphones, have image sensors that could be used for observations to supplement existing technology and research programs (Igoe, 2011).

4.2 Image Sensors

The two main types of image sensors are charged coupled devices (CCD) and complementary metal oxide semiconductors (CMOS). These image sensors are commonly found in digital, smartphone and iPhone cameras and have been used for applications such as forensic investigations, archaeology, space-borne imaging and volcanic gas emission measurements (Kantzas et al. 2010; Olsen et al. 2010; Verhoeven and Schmitt, 2010; Minoglou et al. 2008; Bluth et al. 2007; Bogaerts et al. 2007; Har et al. 2004). Ground based sky cameras, used to measure the amounts and distribution of cloud, also use a CCD image sensor (Sabburg and Wong, 1999). Igoe et al. (2013a and 2013c) used CMOS based smartphones to measure and calculate UVA irradiance and AOD.

The basic architectural differences between CCD and CMOS image sensors is mainly in how the electrical signal generated by photodiodes is relayed for processing within the instrument. The signal amplifier in a CCD image sensor is at the end of the chip, whereas in CMOS, this component is attached to each pixel (Figure 8) (Luo and Yang, 2010; Bai et al. 2008).

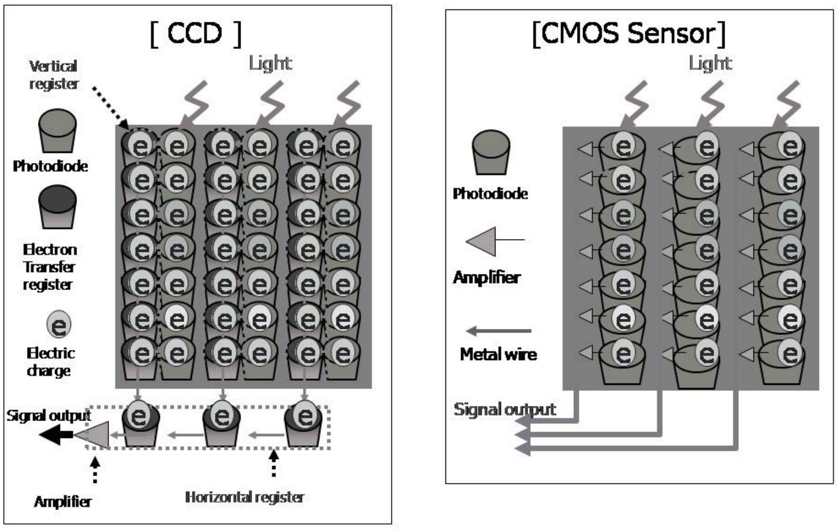

Figure 8: Basic architectural and functional differences between CCD and CMOS showing pixel structure of each type of image sensor (Medina, 2012).

CMOS image sensors have the advantage over the CCD filters of ‘commercial’imaging in requiring lower power, cost less to manufacture and possess greater on chip functionality (Jerram et al. 2010; Blue et al. 2009; Minoglou et al. 2008). CMOS image sensor architecture of an array of photodiodes and pixel circuitry is similar to digital memory components, effectively a ‘lab on a chip’ (Shen et al. 2011; Theuwissen, 2008).

CMOS and CCD image sensors have an inherent sensitivity to UV (Igoe et al. 2013a; Tetley and Young, 2008). The outer lens and internal filters of imaging devices attenuate UV, but still allow useful transmissions to occur in the UVA wavebands (Igoe et al. 2013a; Tetley and Young, 2008). UV sensitivity is increased measurably by including the processes of back-thinning and backside illumination in manufacture, where the substrate is made thinner and the circuitry is placed behind the photodiode respectively (Figure 9) (Jerram et al. 2010; Blue et al. 2009; Minoglou et al. 2008).

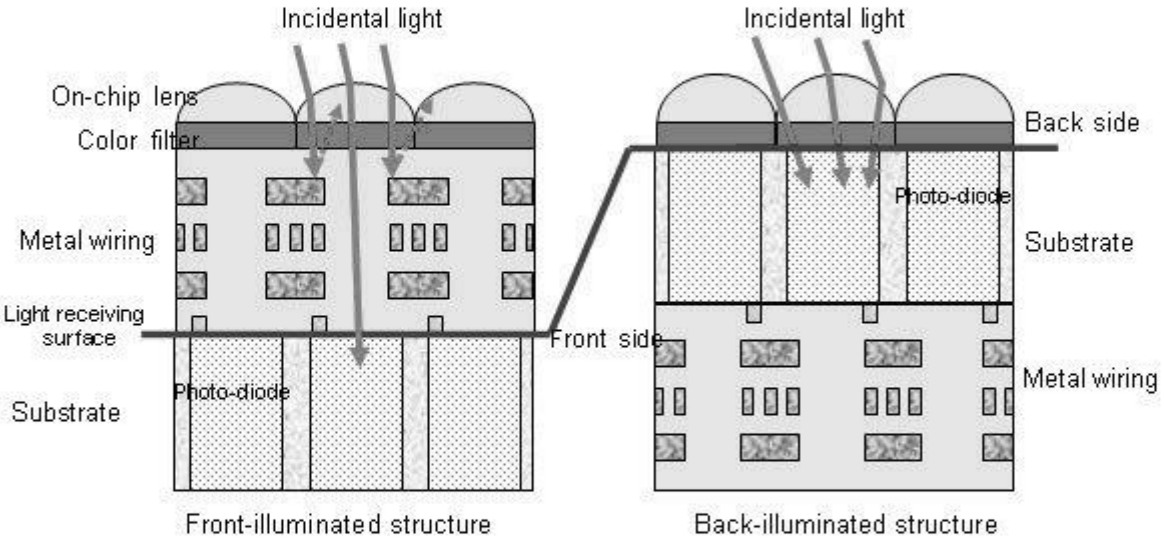

Figure 9: Structure of backside illumination (BSI) showing the difference in how incidental light is received from the image sensor photodiode (Goldman, 2011).

The majority of smartphones use CMOS image sensors, as the on-chip functionality complements the need to economise on space (Hayes, 2012; Shen et al. 2011; Theuwissen, 2008). The size of a smartphone image sensor is limited by the small and shrinking space available in a smartphone due to increasing amount of MEMS (micro electro mechanical sensors) that are being included in these devices (Hayes, 2012). Smartphone image sensors, with suitable narrow bandpass and neutral density filters can effectively detect UVA radiation, even with the outer lens intact and with no modification of the internal filters (Igoe et al. 2013a and 2013c).

4.2.1 Noise Summary

Each brand of smartphone possesses unique noise responses; this is primarily due to differences in manufacture (Alakarhu, 2007). Details of manufacture are unobtainable as they are considered to be propriety information. Most noise sources are temperature dependent (EMVA, 2010; Irie et al. 2008). Image sensor noise can be categorised in 3 ways (Irie et al. 2008):

1. Spatial noise

At low illumination, this is referred to as ‘dark current’ or dark signal non-uniformity (DSNU) (EMVA, 2010; Irie et al. 2008). DSNU is measured by taking the average signal of all pixels while covered at different temperatures (Irie et al. 2008). The magnitude of DSNU is typically low for smartphone image sensors (Alakarhu, 2007). At high illumination, photo response non-uniformity (PRNU) is the main source of noise (Irie et al. 2008). Spatial noise is mitigated by averaging several images with the same illuminance (Irie et al. 2008).

2. Temporal noise

Temporal noise describes pixel fluctuations that vary between images, the mean variation over several images are what provides an approximation of the magnitude (Irie et al. 2008). CMOS image sensors have a greater temporal noise than CCD (Campos et al. 2012).

3. Total noise

Total noise represents the combined spatial and temporal components, determined by the average standard deviation across all image columns (Irie et al. 2008). Each test performed in this study will take the average of multiple pixels taken of the solar image across different times to evaluate the total noise.

4.3 Chapter Discussion

The advantages of commercial image sensor devices are portability, light-weight, ease-of-storage and cost. As cameras, smartphones and iPhones are mass produced, they are easily affordable; have ease of use and require no complicated in depth training. Smartphones are not meant to be replacements of current technology, but rather as a means to supplement, by making monitoring systems accessible to schools and the community.

5. Experimental Results

The components for this research were divided into two parts:

- Feasibility tests, where, under low intensity UVA light, observations were made to test if the smartphone image sensor's response can be characterised when exposed to UVA radiation of known intensity (Igoe et al. 2013a).
- Calibration field tests, where, the smartphone image sensors were calibrated using a Microtops E540 sunphotometer when viewing the sun, to determine aerosol optical depth (AOD) (Igoe et al. 2013c).

5.1 Standard Equipment Used

Known irradiance values used in the feasibility study were supplied by an irradiation monochromator (Figure 10). The monochromator includes a 1600 W xenon arc ozone free lamp (Model 66390 Oriel Instruments, California, USA), digital exposure controller (Model 68591; Oriel Instruments) and a double grating monochromator (Model 74125 Oriel Instruments, California, USA). The monochromator input and output slits were set to 4.5 and 4.0 mm, respectively. The full width at half maximum (FWHM) was approximately 10 nm.

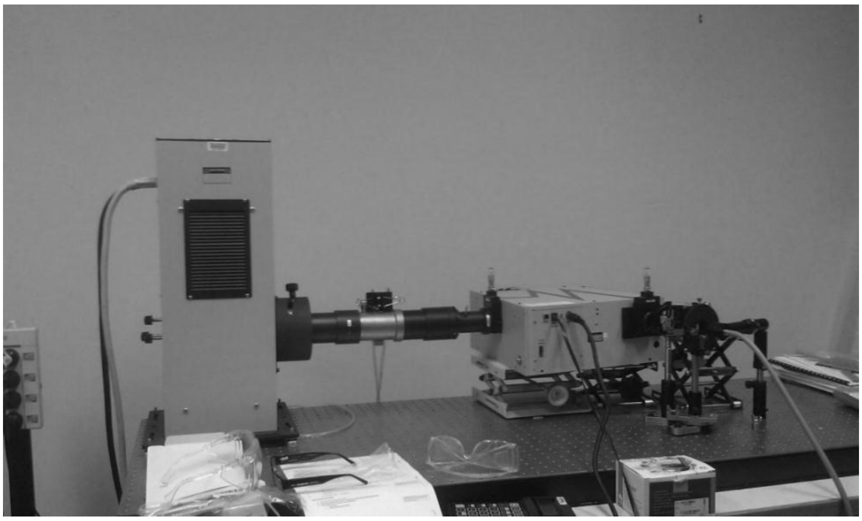

Figure 10: Irradiation monochromator used for producing a stable beam of approximately 10 nm FWHM for the feasibility studies.

Irradiances in the feasibility studies were detected using a double grating scanning UV spectroradiometer, (Model DMc150 Bentham Instruments Ltd. Reading, UK) (Figure 11). The spectroradiometer is calibrated to a UV standard lamp with calibration traceable to the NPL (National Physical Laboratory, Teddington, Middlesex, UK). The input optics were provided by a 10 mm diameter diffuser (model D7; Bentham Instruments, UK) connected by a 5 m long, 4 mm diameter optical fiber to the input slit of the monochromator of the spectroradiometer. The output beam of the irradiation monochromator covered the entire diffuser surface.

Figure 11: Spectroradiometer used for the irradiance measurements in the feasibility tests.

Field tests were calibrated and verified with the use of a Microtops II sunphotometer (model 540, Solar Light, USA) for measuring direct UV irradiances and aerosol optical depth (Figure 12). This instrument was calibrated by the manufacturer at the Mauna Loa Observatory, Hawaii (Morys et al. 2001).

Figure 12: Microtops II Model 540 sunphotometer, used in field calibration tests for measuring direct UV and AOD (Image by Solar Light).

Narrow bandpass filters were used in both the feasibility and calibration tests, specifically bandwidths centred on 320 nm, 340 nm, 360 nm and 380 nm (supplied by CVI Melles Griot, New Mexico, USA); the 340 nm and 380 nm narrow bandpass filters were used specifically for the calibration and verification tests. The 320 nm and 360 nm filters were used for comparison in lab tests. Each filter had a full width at half maximum of 5 nm and a 25 mm diameter.

Neutral density (ND) filters were also used extensively during the experiment to prevent pixel saturation. For both the feasibility and field calibration tests, a ND1% (XND0001, Asahi Spectra, Japan) neutral density filter was used. The 380 nm field calibration tests also used an additional ND2 filter (Bentham Intruments Inc. UK). The neutral density filters transmitted approximately 1% and 50% incident light respectively.

5.2 Smartphone Selection

Three smartphones were selected for testing, based on their cost, accessibility and useability (Igoe et al. 2013a). The Samsung Galaxy 5 (Samsung Electronics, Seoul, South Korea); Huawei U8180 (Huawei Technologies, Shenzhen, China) and the LG Optimus (LG Electronics, Seoul, South Korea) smartphones are examples of low cost and easy to obtain mass market imaging technology, accessible to anyone. All three smartphones have similar size and thickness of the outer lenses and have a CMOS (complementary metal oxide semiconductor) image sensor.

Phone camera settings were set as they would be for the ‘off the shelf’ default. This results in the pictures being saved in JPEG format, subjected to auto exposure and auto white balance. It is unnecessary to obtain the raw images and such a modification would unnecessarily complicate the procedure, especially as the compression can be factored into the data analysis.

Of these smartphone camera systems, the Samsung Galaxy 5 was the only phone that provided photographic information, particularly exposure time, required for characterising the UVA response. For this reason the Samsung Galaxy 5 was used as a representative phone for the feasibility tests (Igoe et al. 2013a).

5.2.1 Lens Attenuation

The 25 mm diameter outer lens of the Samsung Galaxy 5 smartphone was excised as a representative example typical for many smartphone cameras. UVA irradiances from the irradiation monochromator at 10 nm increments were passed through the excised lens. The lens-attenuated irradiance is compared with the incident irradiance from the monochromator in Figure 13.

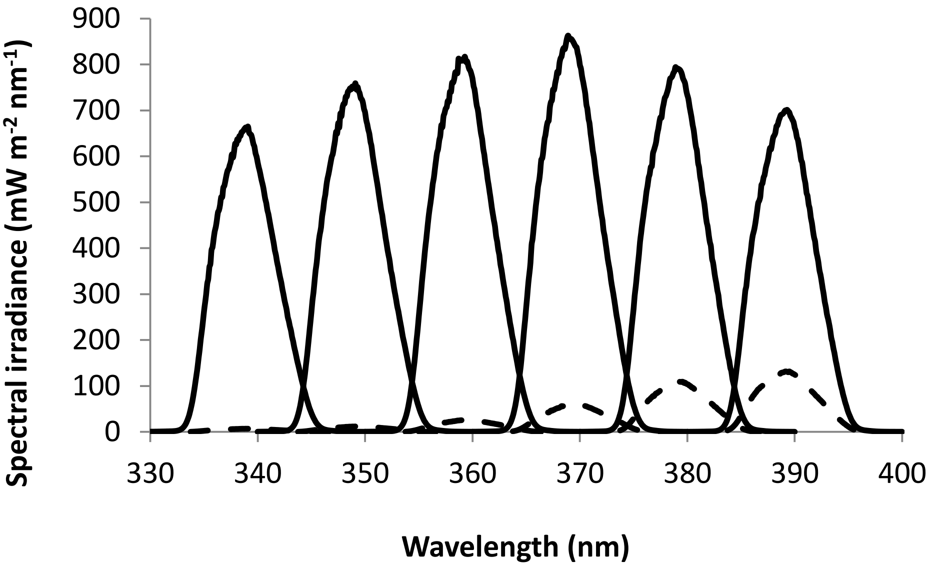

Figure 13: Comparison of the spectral irradiance from the irradiation monochromator (solid lines) to the attenuated irradiance through the excised outer lens (dashed lines) (Igoe et al. 2013a).

The UVA lens transmission is in Figure 14. The smartphone camera lens is a major source of attenuation of UV radiation, decreasing from 18.9% at 390 nm to 1.1% at 340 nm; however, there is still a distinguishable signal at 340 nm (Igoe et al. 2013a).

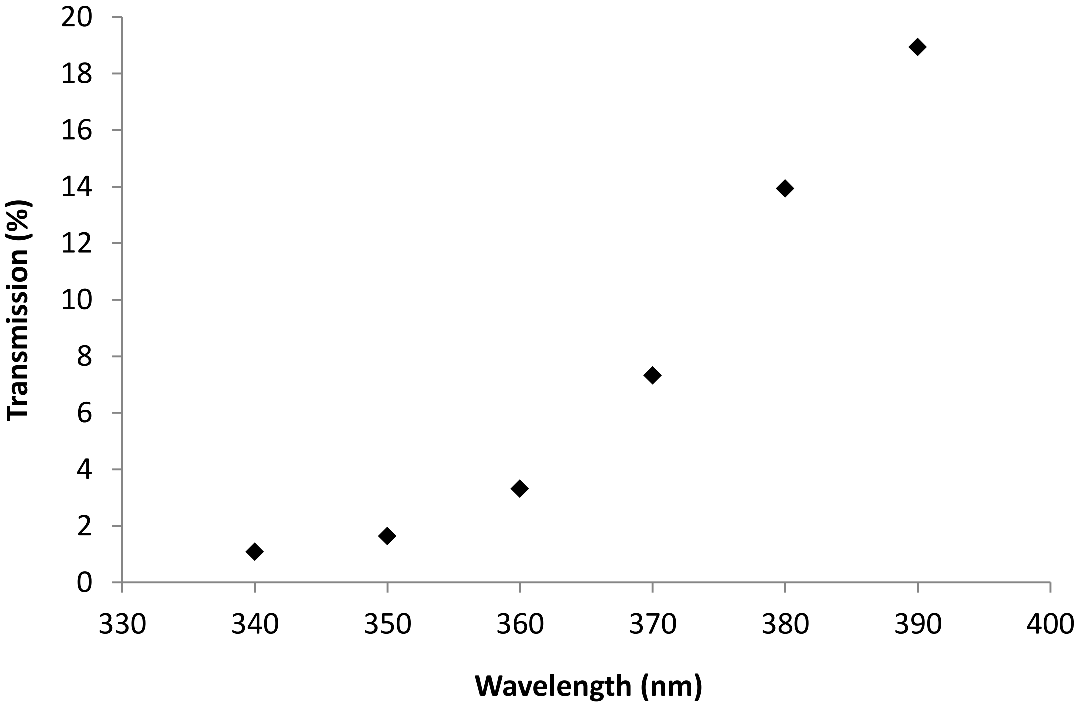

Figure 14: Percentage transmission curve through a smartphone excised outer lens (Igoe et al. 2013).

It was not possible to investigate the transmission of the inner lens and the image sensor filters without causing serious damage to the smartphone camera. For the purposes of this research the outer lens, alongside the inner lens and on-image sensor filters are considered to be components of the smartphone image sensor as a whole, as it is impractical to remove it in everyday use.

5.2.2 Lens Fluorescence

A potential source of error is if the smartphone camera lens fluoresced. To test for fluorescence, the excised lens was subjected to 340 nm and 380 nm irradiances from the irradiation monochromator in a room with a constant temperature of 20°C, with the spectroradiometer detecting throughput spectral irradiances in 1 nm increments up to 500 nm. The tests revealed that the excised lens did not fluoresce. Peaks of 171.2 and 10.9 $mWm^{-2}nm^{-1}$ were measured for 380 nm and 340 nm narrow wavebands respectively, the response measured between 400 nm and 500 nm was only 0.043±0.009 $mWm^{-2}nm^{-1}$ which is insignificant (Igoe et al. 2013a).

5.2.3 Noise Tests

Dark current (or dark fixed pattern noise, DFPN) and thermal noise tests were performed on each of the smartphones. Raising the temperature by 20°C resulted in negligible fluctuations in the average image sensor digital number. Dark current tests were performed by taking photos when the lens was covered at temperatures of 17°C and 37°C. The grayscale digital numbers were obtained using the freeware program SciLab (Igoe et al. 2013a).

Each DFPN image was loaded into SciLab and converted to grayscale, the frequency of each digital number was extracted from the histogram of the whole image and these were then averaged to provide a summary mean DFPN quantity at that temperature. The results are summarised in Table 1.

Table 1: Dark fixed pattern noise (DFPN) at 17°C and 37°C for the Samsung Galaxy 5, Huawei U8180 and LG Optimus, measured in grayscale digital numbers (DN).

Smartphone	DFPN at 17°C (DN)	DFPN at 37°C (DN)
Samsung Galaxy 5	1.7	1.9
Huawei U8180	1.8	2.0
LG Optimus	1.6	1.9

5.3 Feasibility Tests

5.3.1 Methodology

A main concern in this study is to not saturate, nor damage the smartphone camera sensor. However, the signal detected needs to also be above background digital noise levels to be useful (Gallo et al. 2012). Obtaining sufficient and useful digital values will allow an approximation of the sensor irradiance (I_λ) to be calculated using Debevec and Malik (1997)'s algorithm, linking digital values (Z) and exposure time (Δt),

$$f(Z) = \ln I_\lambda + \ln \Delta t. \qquad [8]$$

Debevec and Malik (1997) state that the luminaire irradiance (e.g. from the monochromator) can be used for sensor irradiance. The exposure time (Δt) is retrieved from the photo's digital EXIF data, this generally cannot be altered in a smartphone (Igoe et al. 2013a). The red, green and blue digital values (Z) can be retrieved from the photo's pixel data using a program such as the freeware program SciLab (SciLab, 2012). The camera response function (f) is determined by graphing digital values (Z) against the natural logarithm of the product of sensor irradiance and exposure time ($\ln I_\lambda + \ln \Delta t$), incorporating the linear and non-linear image processes (Gallo et al. 2012; Debevec and Malik, 1997).

UV narrow bandpass filters from 320 nm to 400 nm, at 20 nm intervals were used; each not only restricted the incident wavelengths, but also attenuated the light, resulting in transmissions of approximately 25% to 50%. However, this transmission is well above that of neutral density filters used for solar photography, for example, the ND-400 filter, has only a transmission of 0.2% (hoyafilter.com). Used in combination, the UV bandpass and the ND1% neutral density filter approximated the ND-400 filter while only allowing a specific wavelength to pass through to the image sensor. Baseline irradiances were determined, using the spectroradiometer. These irradiances were measured at 0.1 nm intervals 10 nm above and below the discrete target UV-A wavelengths emitted from the monochromator. The transmissions of the lens, neutral density and 340, 360 and 380 nm narrow bandpass filters used in laboratory tests are summarised in Table 2.

Table 2: The percentage transmissions of each and combinations of the lens and filter elements used in this part of the study (Igoe et al. 2013a).

	Transmission (%) at Incident Wavelength		
	340 nm	360 nm	380 nm
Bandpass filter	35.1	29.2	3.41
ND1%	1.3	1.3	1.4
Bandpass + ND1%	0.46	0.38	0.048
Bandpass + ND1% + lens	0.0051	0.017	0.0065

Images were taken in the dark at a constant room temperature of 20°C. The 5 highest red, green and blue digital numbers were extracted and averaged across 3 images (Igoe et al. 2013a). Saturated and noise level values were omitted for these calculations. Distances from the monochromator were varied from 10 to 25 cm in 2.5 cm intervals for each discrete wavelength at 320, 340, 360 and 380 nm, in order to provide a range of irradiances and corresponding images that are used to characterise the Samsung Galaxy 5 according to equation 8. (Igoe et al. 2013a). An example of a feasibility experiment setup is shown in Figure 15.

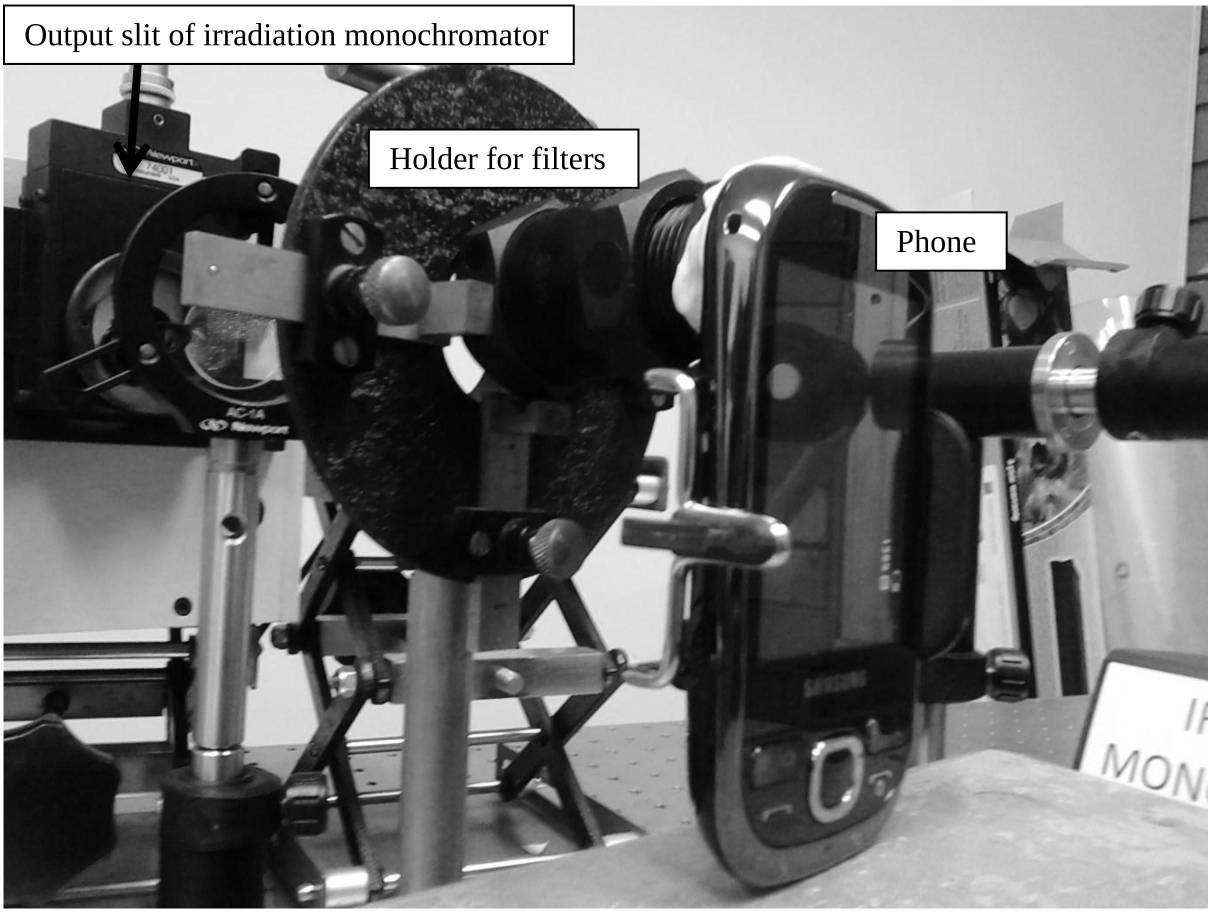

Figure 15: Feasibility experimental setup. The UV radiation is from the irradiation monochromator and the smartphone is in position in front of the output optics.

5.3.2 Results

Figure 16 shows the result of the tests performed with irradiances from 340, 360 and 380 nm compared with the image sensor's chromatic green response as defined by Malacara (2002) in equation 9,

$$g = \frac{G}{R+G+B} \qquad [9]$$

(R, G and B represent the red, green and blue digital numbers respectively).

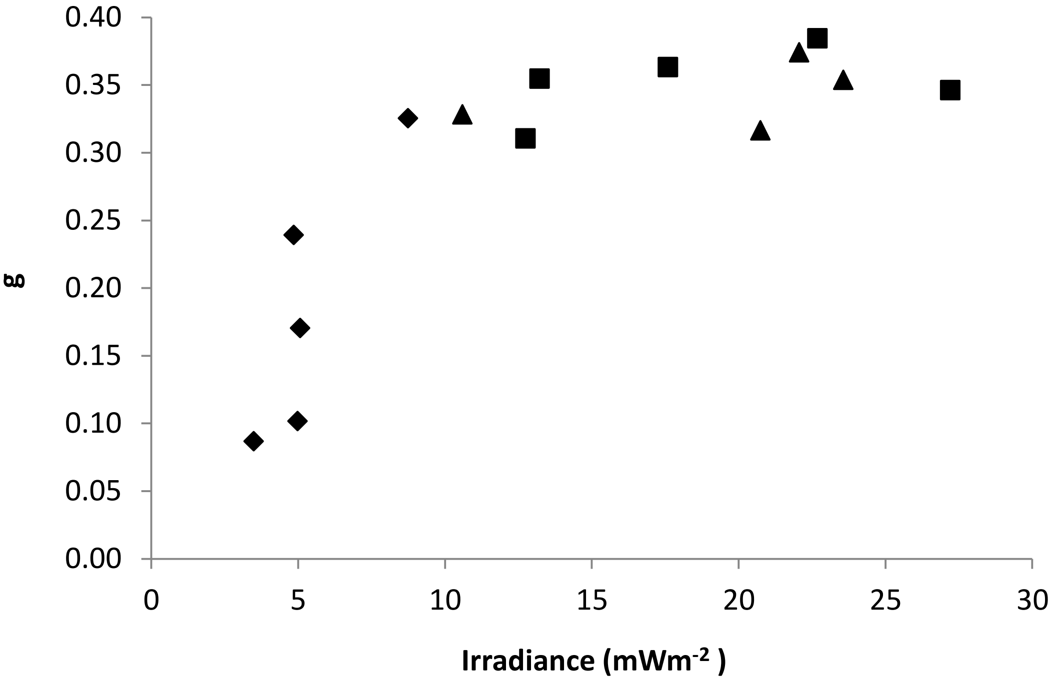

Figure 16: Raw smartphone camera response as a function of irradiance for 340 nm (squares), 360 nm (triangles) and 380 nm (diamonds) (Igoe et al. 2013a). Exposure time was not changed.

Several mathematical models to characterise the smartphone camera UVA response were considered. Debevec and Malik (1997)'s algorithm (equation 8) provided the strongest fit when modified by (Igoe et al. 2013a) to become,

$$f(Z) = f(g) = 26.455g^{2.5} - 7.9206, \qquad [10]$$

This yields the full derivation from equation 8 as being,

$$26.455g^{2.5} - 7.9206 = \ln I_\lambda + \ln \Delta t \qquad [11]$$

This relationship can be seen in Figure 17, the data point is the average over 15 values and the error bars represent the standard error from 15 samples taken at each point. The correlation coefficient was 0.82 (Igoe et al. 2013a).

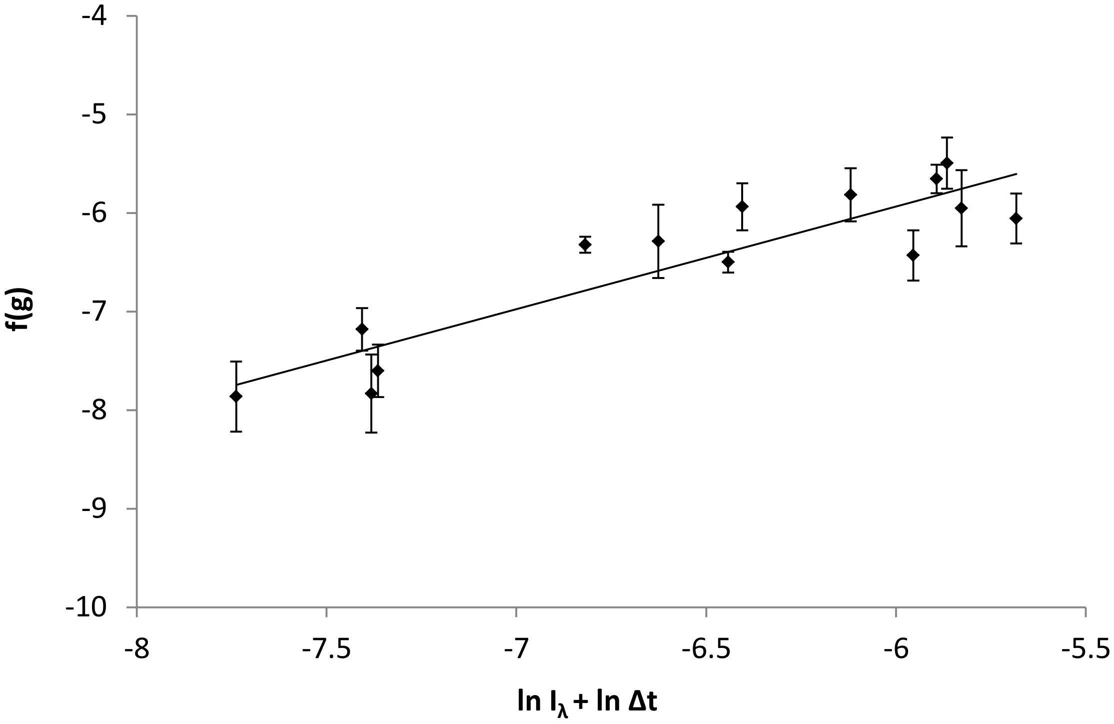

Figure 17: UVA characterisation of a Samsung Galaxy 5 (Igoe et al. 2013a).

5.4 Calibration Field Tests

5.4.1 Methodology

Field tests were conducted in two phases: the first was to develop a calibration between the smartphone camera image sensor’s response to direct UV in narrow wavebands with the direct UV irradiance recorded by the Solar Light Microtops II sunphotometer, then develop an algorithm to determine AOD from the image sensor response; the second was to verify that the algorithm from the first phase still applied for different or similar conditions. The same three smartphones as for the laboratory tests (Huawei 8180, Samsung Galaxy 5 and LG Optimus) were used for the field calibration and verification tests with the same settings. However, the Huawei 8180 failed during the first 380 nm calibration test with the full calibration and validation being done on the remaining two phones.

<u>Locations</u>

Two Queensland locations were selected for this part of the study. The first set of tests were performed in mid-Spring in the coal mining town, Emerald (23.53°S 148.16°E), this location is susceptible to high continental and desert dust aerosol loading due to the mining operations, infrequent biomass burning and desert dust originating from arid regions to the west of this location. The solar zenith angles observed in Emerald during the tests were between 60° and 20°. The second set of tests were performed in mid-Summer in Toowoomba (27.56°S 151.96°E), this location has a higher altitude of approximately 690 m above sea level and often has more stable urban-continental aerosol loading. The solar zenith angles observed during this series of tests were between 60° and 4°.

Calibration and verification

Calibration tests were performed at 20 minute intervals from 9 am to midday on visually clear days, when the sun's disk was not obscured by clouds. Calibration tests were performed in both Emerald and Toowoomba during spring and summer. Each 20 minute observation was calibrated to the Microtops II sunphotometer (Solar Light) which takes direct irradiance measurements (Morys et al. 2001). This requires the smartphone cameras to take photos directly of the sun, something that they are not designed to do as the image sensor would be saturated at best and irreparably damaged at worst. Also, smartphone image sensors are not inherently designed to detect specific wavelengths, despite being sensitive to UV wavelengths (Tetley and Young, 2008).

Filters were used to ensure the image sensor did become saturated when exposed to incident light. Saturation of the image sensor still occurred with the inclusion of the 340 nm and 380 nm narrow bandpass filters, necessitating the use of the ND1% neutral density filter for use with both narrow bandpass filters and an additional ND2 neutral density filter for 380 nm observations. The filters were secured into a small 7 cm long, 25 mm inner diameter black pipe that in turn covered the outer lens of the smartphone camera (Figure 18). It is important that the base is completely sealed to prevent any light leakage. It is also important that the filters are securely placed at the open end. For these initial calibration tests, temporary adhesives such as BluTak and electrical tape were found to effectively block all stray light. The pipe was selected so that the inner diameter accommodated the filters, providing a 20° field of view. Internal reflection within the pipe was minimised by ensuring the solar disk was at the centre of the image.

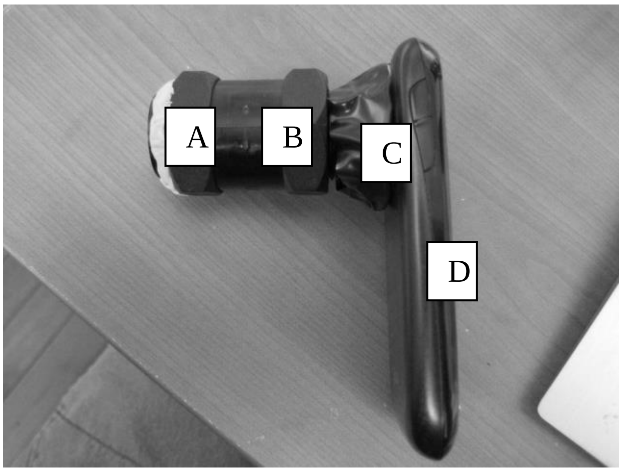

Figure 18: Smartphone camera and filter setup. Bandpass filter is at A; ND2 neutral density filter (for 380 nm tests) at B; and ND1% neutral density filter at C. The smartphone is at D.

The smartphone setup in Figure 18 was then clamped onto a tripod for stability. Figure 19 shows the full setup, with the smartphone setup on top of the tripod at height 1 m above the ground. On one of the seats is the Microtops II sunphotometer used for calibration.

Figure 19: Field setup, including smartphone with filters on top of the tripod. The Microtops sunphotometer pictured was used to calibrate the smartphone camera's image sensor data.

At each 20 minute interval, a reading from the sunphotometer was taken, and the smartphone camera and tube assembly aligned to take 3 photos of the sun. This process was repeated to validate the original results. The ambient air temperature ranged from 16°C to 32°C and the air mass was between 1 and 2 for the observations. The zero-shadow method was employed to ensure that the image of the sun was at the centre of each image as can be seen in Figure 20.

Figure 20: A grayscale image of the sun, taken with a 340 nm filter covered Samsung Galaxy 5 smartphone camera (magnified image). (Igoe et al. 2013b).

Each photo was converted to greyscale in Scilab, and the highest 100 pixel values, approximating the brightest part of the sun’s image were selected. The three photos taken for each observation were averaged, giving a total of 300 pixel values which were then averaged and the standard deviation determined using Microsoft Excel. For each series of measurements with each phone, the best model was evaluated that gave the best regression of the averaged grey values from the smartphone with the measured ln(I) from the Microtops II sunphotometer. For each of the target wavelengths, a 2nd set of observations were performed in different locations and/or different aerosol conditions to validate the calibration.

5.4.2 Results

The results are presented in three stages:

1. Calibration of the smartphone signal with the direct irradiance detected by the Microtops II sunphotometer for each phone at each wavelength individually; a summary of 340 nm and 380 nm tests and finally, all the data from all tests together.
2. Comparisons of the derived ln(I) values from the Microtops and smartphones in a similar manner to stage 1.
3. Comparisons of the derived AOD, with validation data where appropriate.

Three data analyses were performed. One testing the viability of a single algorithm of all combined data, the next investigated wavelength based data and the final test determined if each phone responded differently to each of the target wavelengths.

5.4.2.1 Calibration

Incident direct solar irradiance observed at a point when the sun is at zenith is subjected to an air mass of 1. When viewing the sun ‘off axis’ or with an air mass greater than 1, the irradiance detected by a camera sensor is subjected to the same trigonometric transformations that occur with vignetting and field darkening, reducing it by a factor of $\cos^4\theta$ (Hauftecker, 2000; Smith, 2000), where θ is the solar zenith angle. The $\cos^4\theta$ reduction at increased air masses was found to also apply to the average grey signal (G) from the smartphone image sensor, providing a ‘cosine grey' value, corrected for increased air mass. The natural log of both the measured irradiance and the corresponding cosine grey were then compared, as follows (Igoe et al. 2013c).

$$\ln\left(I_{Microtops}\right) \propto \ln(Y \cos^4 \theta) \qquad [12]$$

where $$Y = 0.30R + 0.59G + 0.11B \qquad [13]$$

(R, G and B represent red, green and blue pixel values respectively).

As each calibration took on the form of a linear regression, equation 12 becomes (Igoe et al. 2013c),

$$\ln\left(I_{Microtops}\right) = m \ln(Y \cos^4 \theta) + c \qquad [14]$$

where m and c are the gradient and intercept for each regression respectively.

Calibration error calculations

The error of Y in equation 12 is calculated as being one standard deviation of 300 pixel values taken for each test (α_Y) and therefore is a far more dominant error than that occurring with θ. For error purposes, θ will be considered as a constant (Hughes and Hase, 2010). Therefore, for error calculations, the cosine grey formula (equation 12) simplifies to,

$$Z = \ln kY \qquad [15]$$

where $k = \cos^4(\theta)$

Thus using the calculus approach described by Hughes and Hase (2010), the error (α_Z) of the right hand side of equation 12 is,

$$\alpha_Z = \frac{\alpha_Y}{Y} \qquad [16]$$

The errors associated with the gradient and intercept in equation 14 are calculated according to algorithms developed by York et al. (2004), implemented in *Microsoft Excel*® for this research in order to incorporate the errors in each data point.

Samsung Galaxy 5

The calibration regression for the Samsung Galaxy 5 observations at 340 nm (Figure 21) was calculated as,

$$\ln\left(I_{Microtops}\right) = 0.2618[\ln(G\cos^4\theta)] - 1.0538 \qquad [17]$$

The regression correlation is very strong ($R^2 = 0.99$). The errors calculated for the gradient and intercept are 0.0206 and 0.0014 respectively.

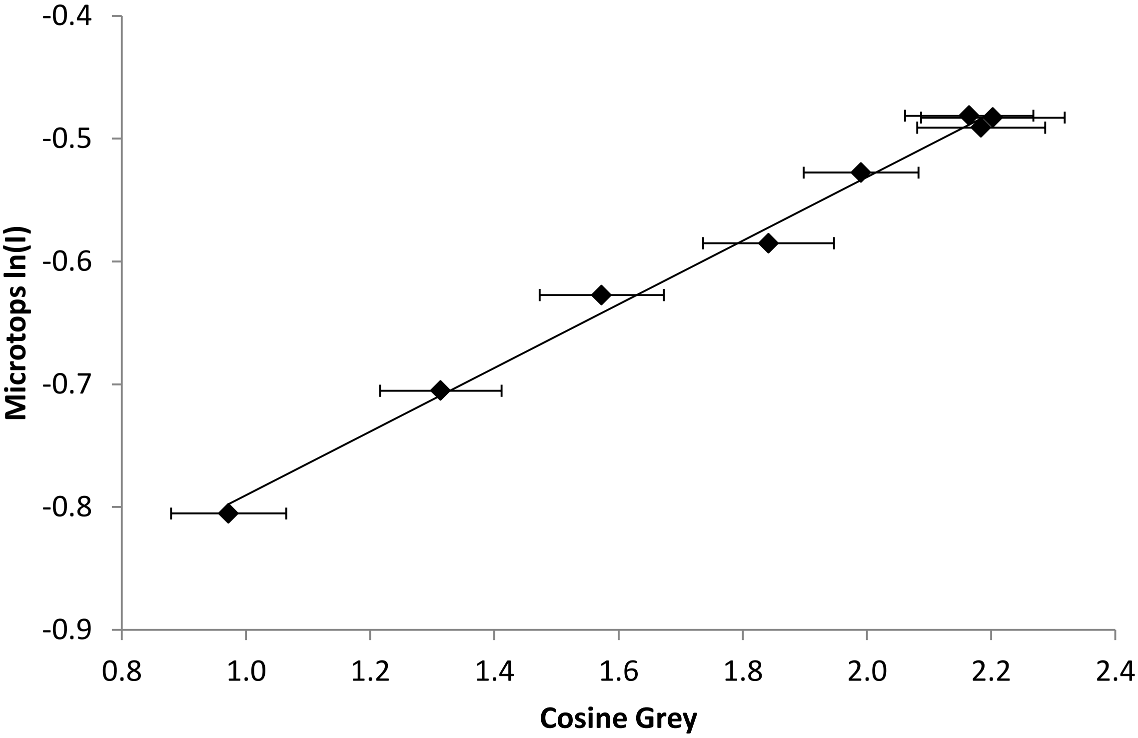

Figure 21: Calibration regression between the Microtops derived ln(I) and the Samsung Galaxy 5 derived cosine grey for observations made at 340 nm.

The calibration regression for the Samsung Galaxy 5 observations at 380 nm (Figure 22) was calculated as,

$$\ln\left(I_{Microtops}\right) = 0.1451[\ln(G\cos^4\theta)] + 0.1228 \qquad [18]$$

The regression correlation is very strong (R^2 = 0.97). The errors calculated for the gradient and intercept are 0.0021 and 0.0001 respectively. Note, the error bars are too small to be seen in the graph.

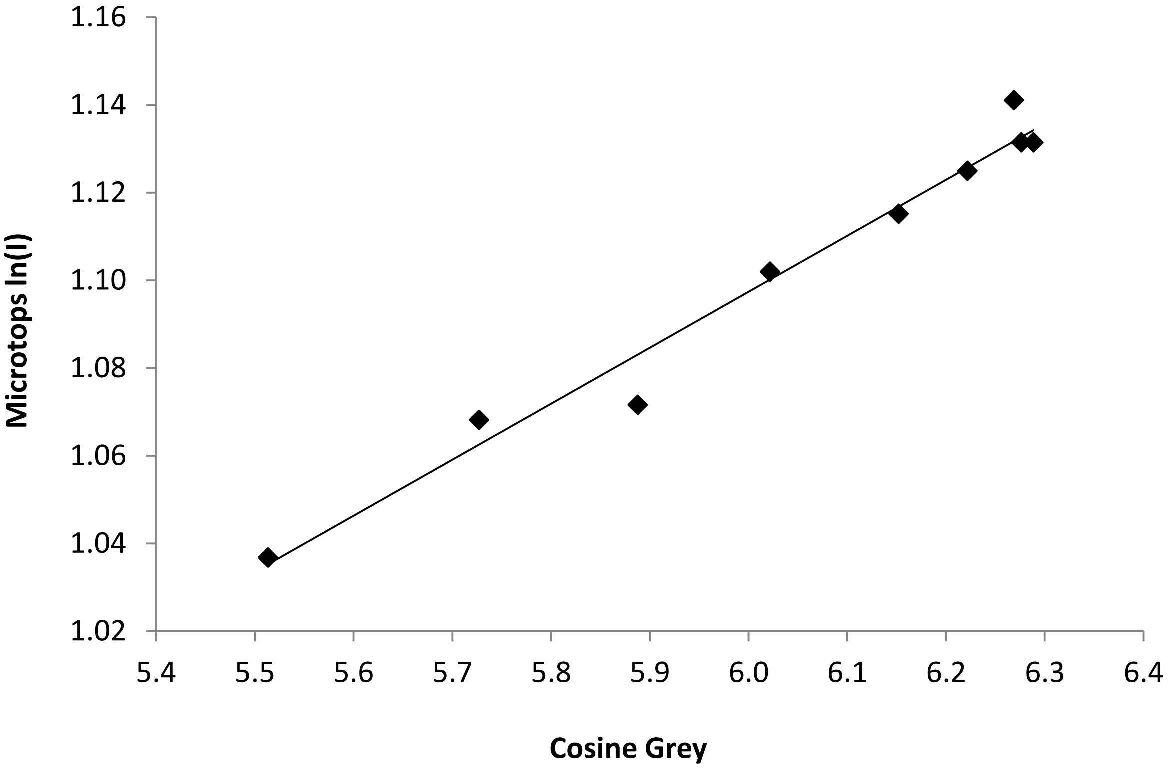

Figure 22: Calibration regression between the Microtops derived ln(I) and the Samsung Galaxy 5 derived cosine grey for observations made at 380 nm. Error bars are too small to be seen.

<u>Huawei U8180</u>

The calibration regression for the Huawei U8180 observations at 340 nm (Figure 23) was calculated as,

$$\ln(I_{Microtops}) = 0.2922[\ln(G\cos^4\theta)] - 1.1152 \qquad [19]$$

The regression correlation is very strong ($R^2 = 0.99$). The errors calculated for the gradient and intercept are 0.0092 and 0.0003 respectively. The Huawei failed to work for the 380 nm observations.

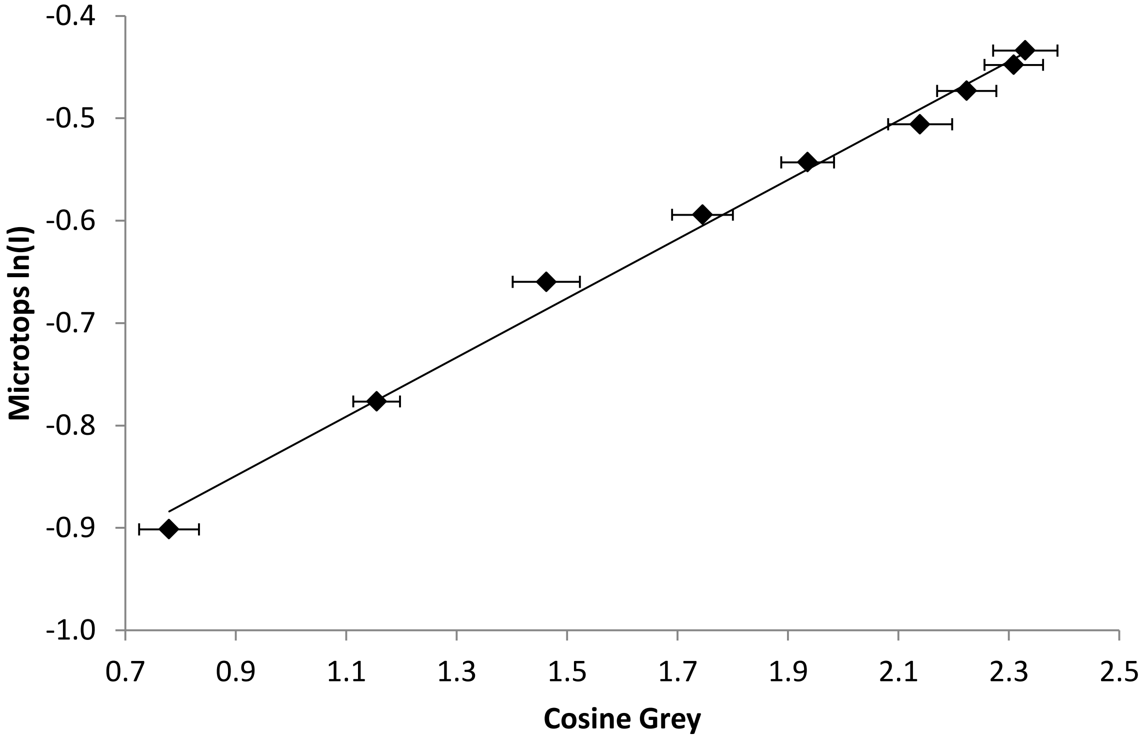

Figure 23: Calibration regression between the Microtops derived ln(I) and the Huawei U8180 derived cosine grey for observations made at 340 nm.

LG Optimus

The calibration regression for the LG Optimus observations at 340 nm (Figure 24) was calculated as (Igoe et al. 2013c),

$$\ln\left(I_{Microtops}\right) = 0.3396[\ln(G\cos^4\theta)] - 1.2695 \qquad [20]$$

The regression correlation is very strong ($R^2 = 0.996$). The errors calculated for the gradient and intercept are 0.0124 and 0.0005 respectively.

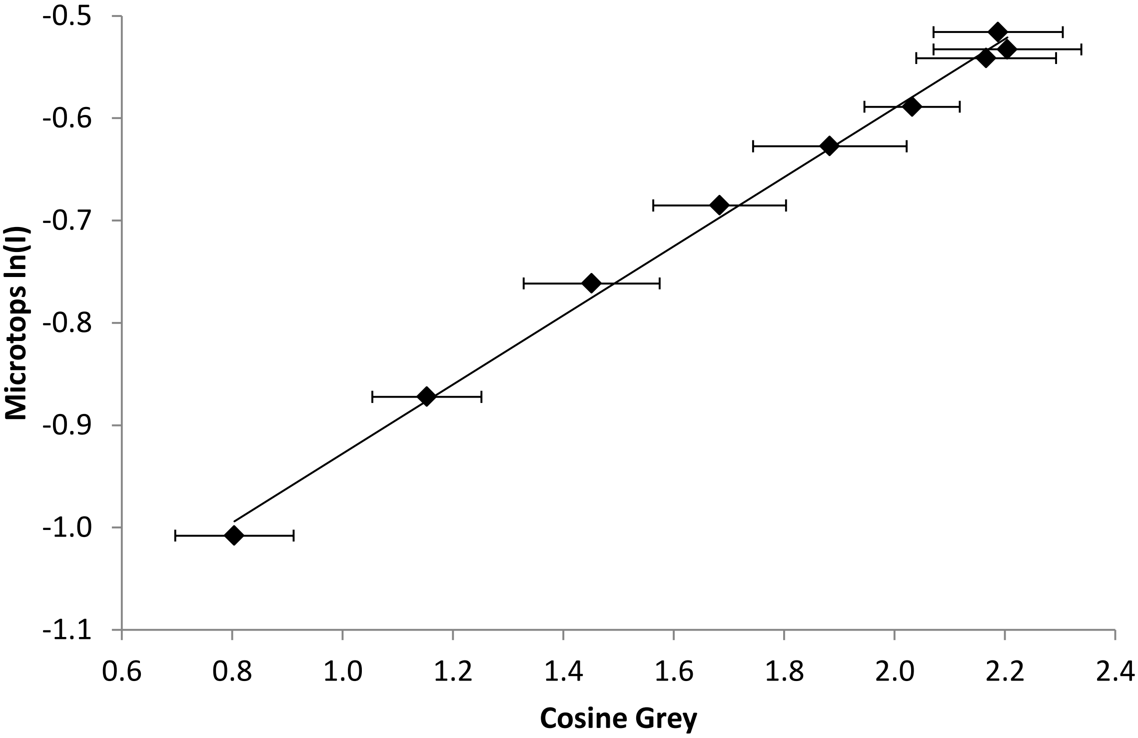

Figure 24: Calibration regression between the Microtops derived ln(I) and the LG Optimus derived cosine grey for observations made at 340 nm.

The calibration regression for the LG Optimus observations at 380 nm (Figure 25) was calculated as (Igoe et al. 2013c),

$$\ln(I_{Microtops}) = 0.1370[\ln(G\cos^4\theta)] + 0.2728 \qquad [21]$$

The regression correlation is very strong (R^2 = 0.97). The errors calculated for the gradient and intercept are 0.0003 and 0.000004 respectively. Note, the error bars are too small to be seen on the graph.

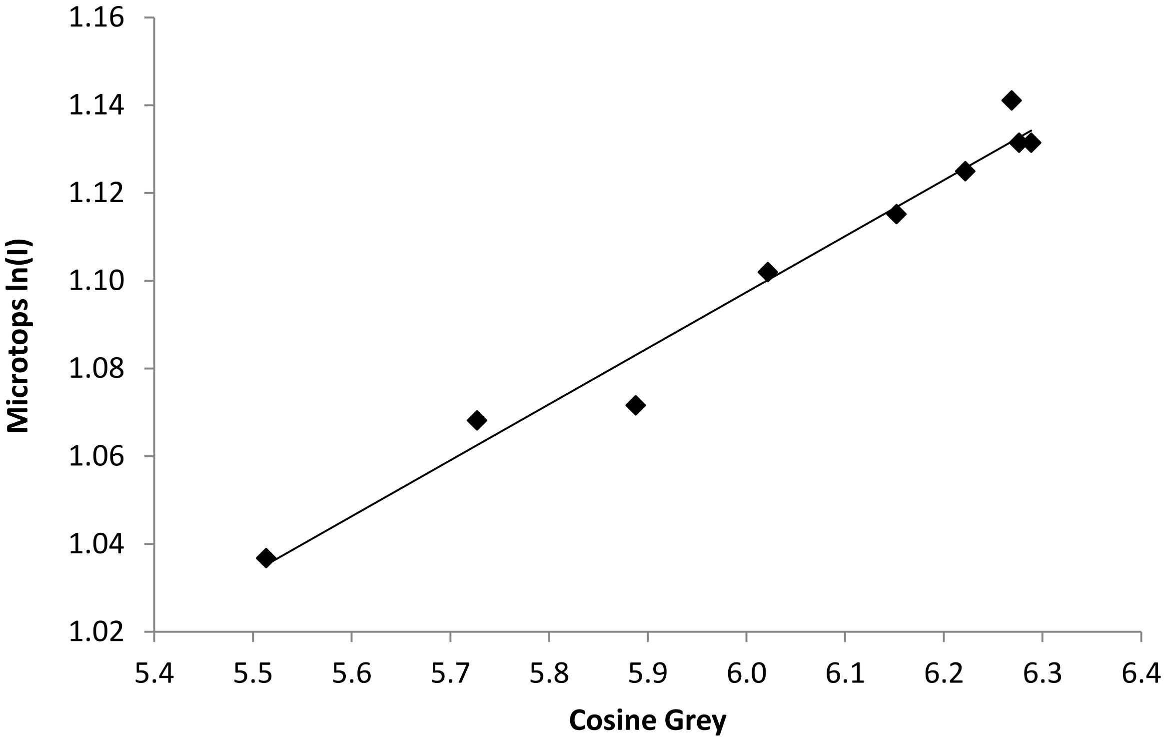

Figure 25: Calibration regression between the Microtops derived ln(I) and the LG Optimus derived cosine grey for observations made at 380 nm. Error bars too small to be seen.

Combined 340 nm results

The calibration regression for all 340 nm combined observations (Figure 26) was calculated as,

$$\ln\left(I_{Microtops}\right) = 0.3077[\ln(G\cos^4\theta)] - 1.1511 \qquad [22]$$

The regression correlation is very strong ($R^2 = 0.93$). The errors calculated for the gradient and intercept are 0.0086 and 0.0002 respectively.

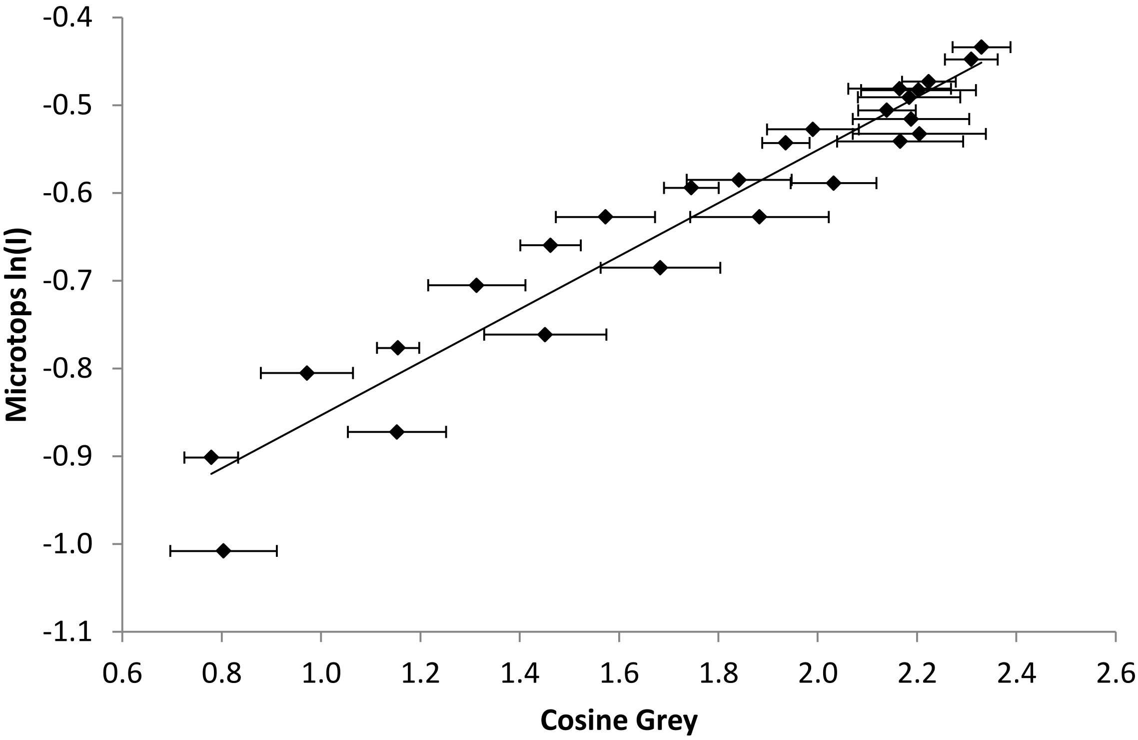

Figure 26: Calibration regression between the Microtops derived ln(I) and all smartphones derived cosine grey for observations made at 340 nm.

<u>Combined 380 nm results</u>

The calibration regression for all 380 nm combined observations (Figure 27) was calculated as,

$$\ln\left(I_{Microtops}\right) = 0.1821[\ln(G\cos^4\theta)] - 0.0042 \qquad [23]$$

The regression correlation (R^2) provides a coefficient of 0.76. The errors calculated for the gradient and intercept are 0.0006 and 0.00001 respectively.

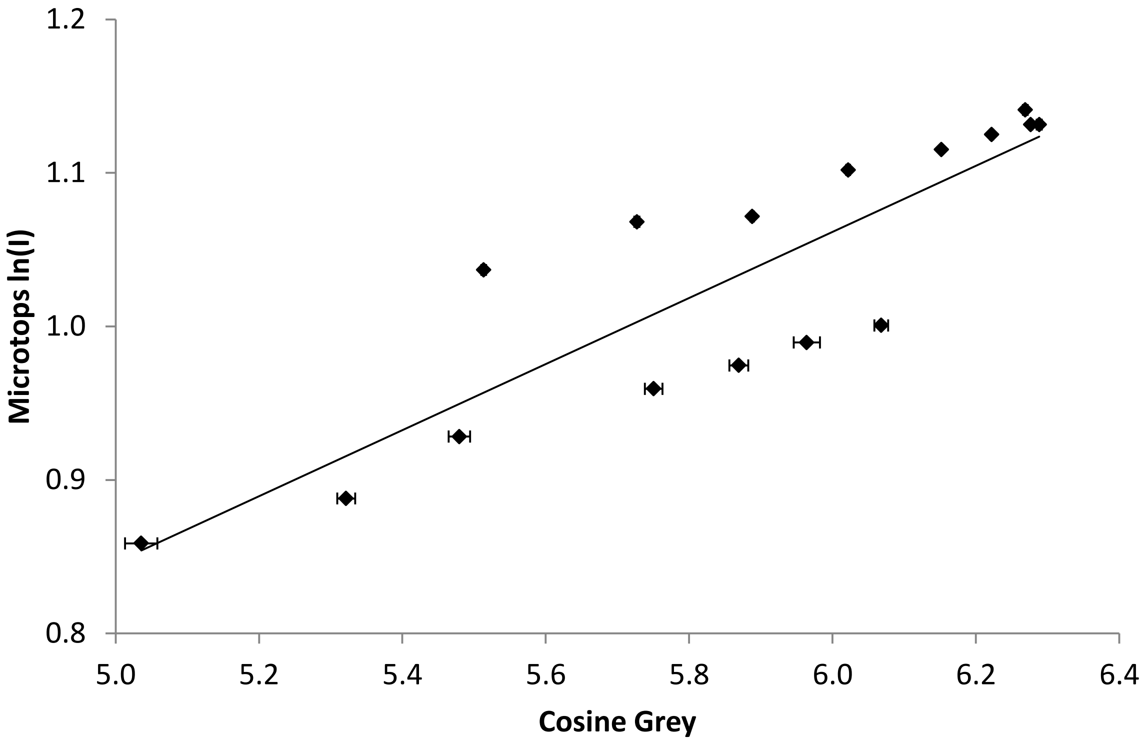

Figure 27: Calibration regression between the Microtops derived ln(I) and all smartphones derived cosine grey for observations made at 380 nm.

All combined results

The calibration regression for all combined observations (Figure 28) was calculated as,

$$\ln\left(I_{Microtops}\right) = 0.3515[\ln(G \cos^4 \theta)] - 1.0396 \qquad [24]$$

The regression correlation is very strong ($R^2 = 0.99$). The errors calculated for the gradient and intercept are 0.0009 and 0.00003 respectively.

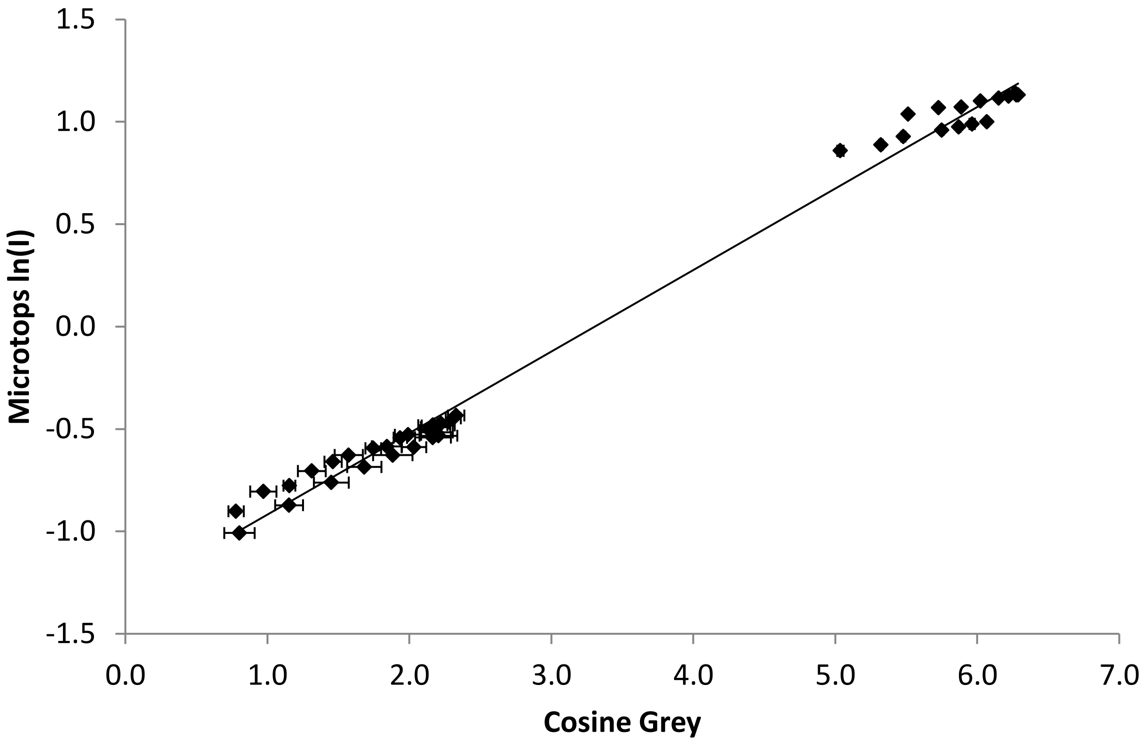

Figure 28: Calibration regression between the Microtops derived ln(I) and all smartphones derived cosine grey observations.

5.4.2.2 Direct Irradiance comparisons

For error calculations, the smartphone calibration regression can be simplified to,

$$\ln\left(I_{Smartphone}\right) = mZ + c \qquad [25]$$

where $Z = \ln(G \cos^4 \theta)$

The error for the intercept (c) is significantly lower than the error for the gradient (m), hence, would not add significantly to the overall calculated error and is subsequently considered negligible in subsequent error calculations (Hughes and Hase, 2010). Thus, the revised formula for error purposes becomes

$$\ln\left(I_{Smartphone}\right) = mZ \qquad [26]$$

Using the calculus approach described by Hughes and Hase (2010), the total error for the smartphone calibration regression is calculated by

$$\alpha\ln\left(I_{Smartphone}\right) = \ln\left(I_{Smartphone}\right)\sqrt{\left(\frac{\alpha_m}{m}\right)^2 + \left(\frac{\alpha_Z}{Z}\right)^2} \qquad [27]$$

The irradiance comparisons will be grouped according to the target wavelengths.

340 nm

There are very strong correlations between the Microtops and smartphone derived natural log of direct solar irradiance data at 340 nm. Individually, the natural log of the derived irradiance of each of the phones had an average discrepancy of between 2% and 4% (Figure 29-Figure 31); with the least discrepancy occurring with the LG Optimus; all the 340 nm data combined for all phones yielded an average discrepancy of 6% (Figure 32). The errors decreased with increasing solar irradiance. The error bars are calculated according to equation 27.

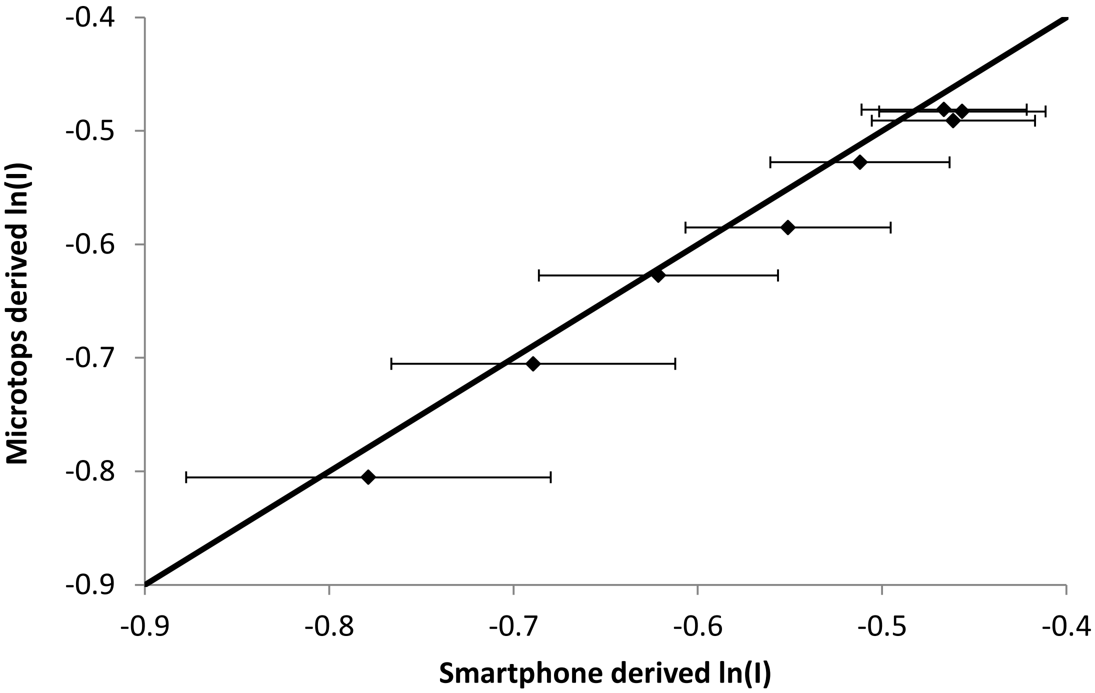

Figure 29: ln(I) comparison for the Samsung Galaxy 5 observed at 340 nm. The one-to-one equivalence line is in bold.

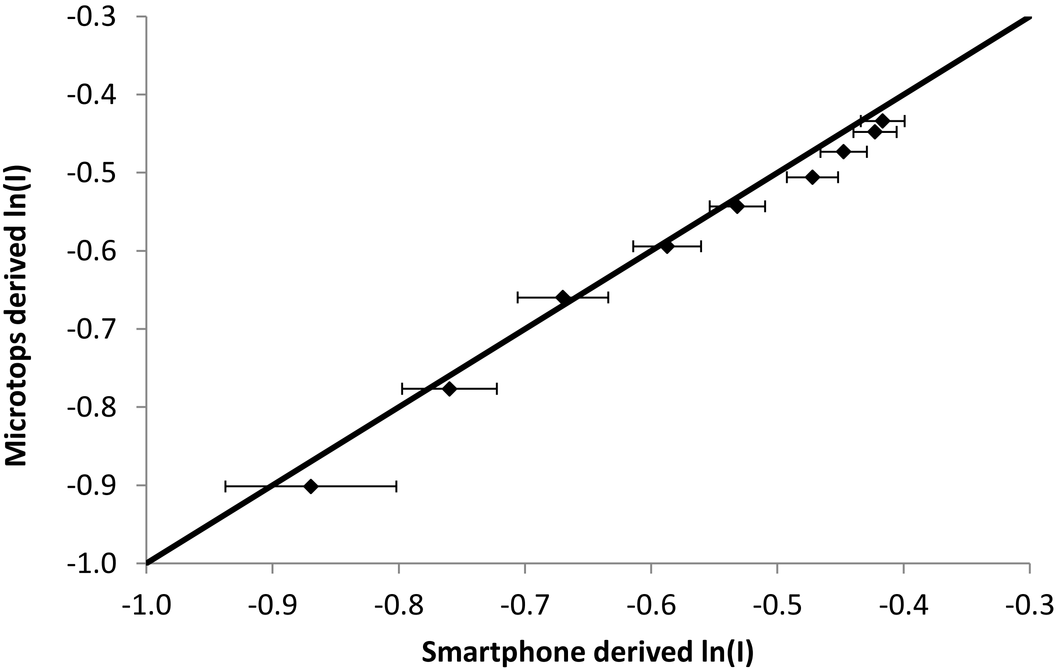

Figure 30: ln(I) comparison for the Huawei U8180 observed at 340 nm. The one-to-one equivalence line is in bold.

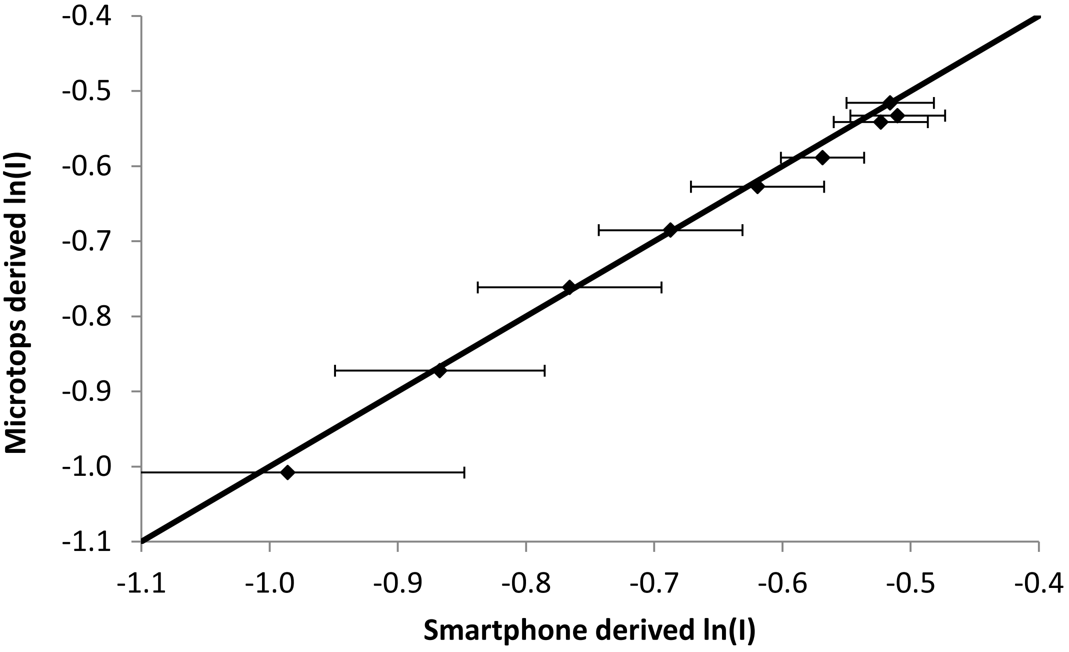

Figure 31: ln(I) comparison for the LG Optimus observed at 340 nm. The one-to-one equivalence line is in bold (Igoe et al. 2013c).

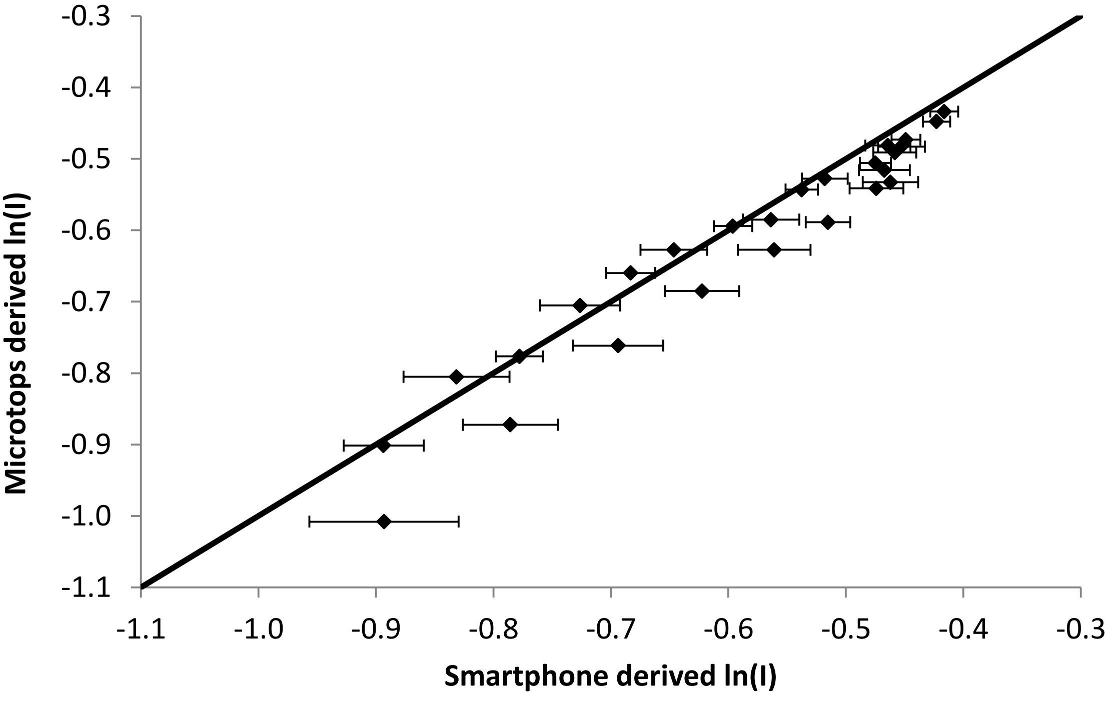

Figure 32: ln(I) comparison for all observations at 340 nm. The one-to-one equivalence line is in bold.

380 nm

There are strong correlations between the Microtops and smartphone derived natural log of direct solar irradiance data at 380 nm. Individually, the natural log of the derived irradiance of each of the phones tested had an average discrepancy of 3% for both the Samsung Galaxy 5 and the LG Optimus (Figure 33 and 34); all the 380 nm data combined yielded an average discrepancy of 6% (Figure 35). The discrepancies could be, in part, due to some internal reflections within the pipe and solar aureole on the sensor. Unlike the 340 nm data, the errors at 380 nm remained constant with increasing solar irradiance, with most of the smartphone derived data falling below the equivalence line.

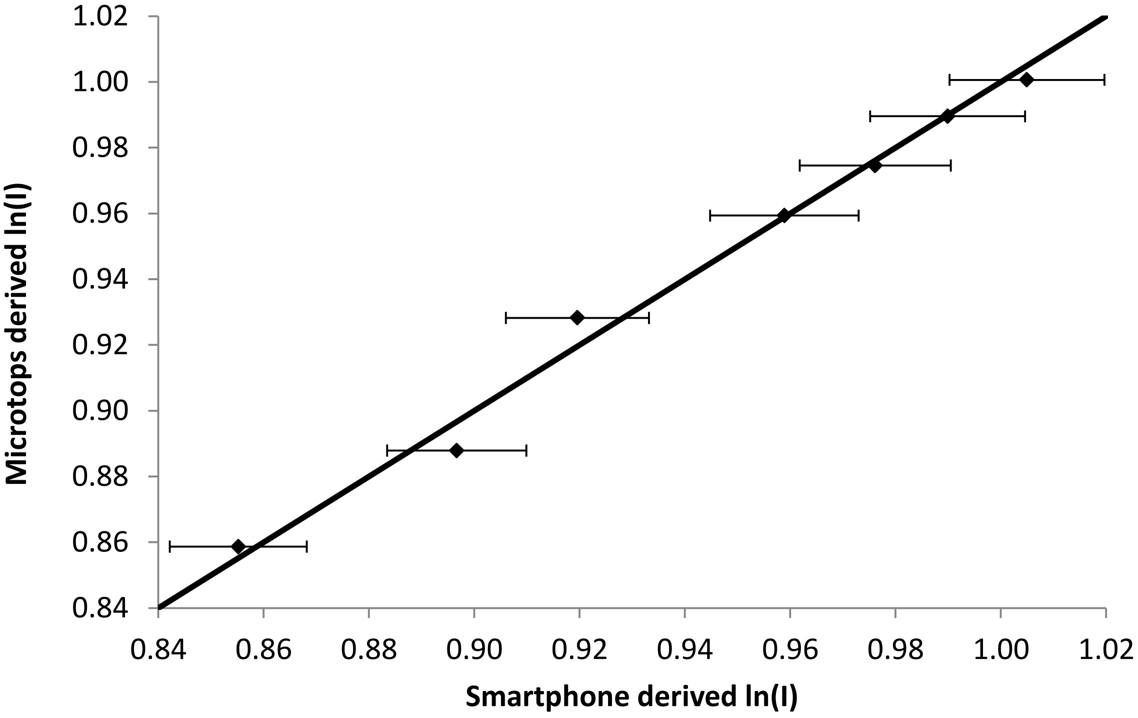

Figure 33: ln(I) comparison for the Samsung Galaxy 5 observed at 380 nm. The one-to-one equivalence line is in bold.

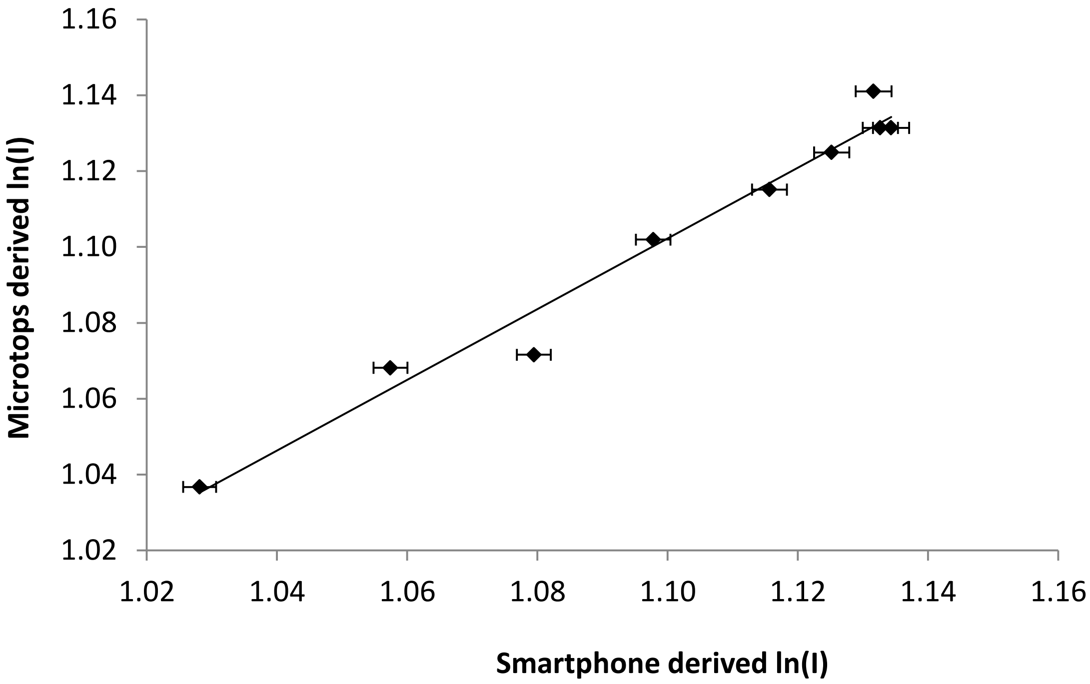

Figure 34: ln(I) comparison for the LG Optimus observed at 380 nm. The one-to-one equivalence line is in bold (Igoe et al. 2013c).

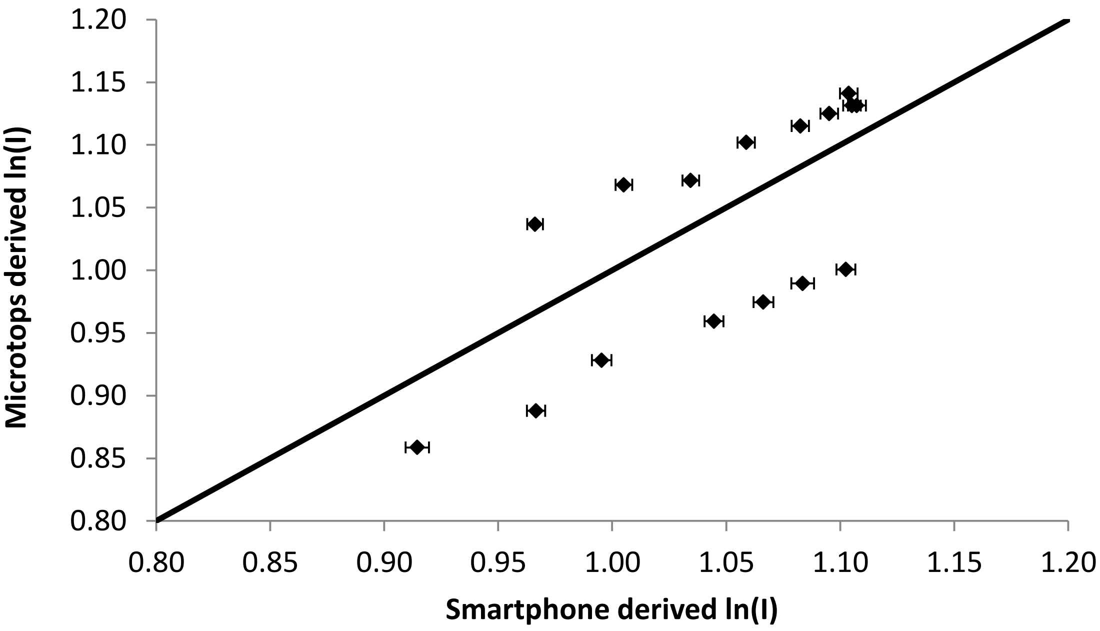

Figure 35: ln(I) comparison for the combined smartphone observations at 380 nm. The one-to-one equivalence line is in bold.

All data

There is strong correlation for all combined smartphone derived ln(I) data compared to that derived from the Microtops based on the calibration in equation 24. The one-to-one equivalence line is above most of the 340 nm data and bisects the 380 nm data, resulting in an average discrepancy of 26%. The error patterns observed with the 340 nm and 380 nm were also observed with the complete data set, where the errors decrease with increased solar irradiance (Figure 36). The differences between this and earlier graphs are due to the different calibration constants used in equation 24 compared to earlier smartphone and wavelength based calibrations.

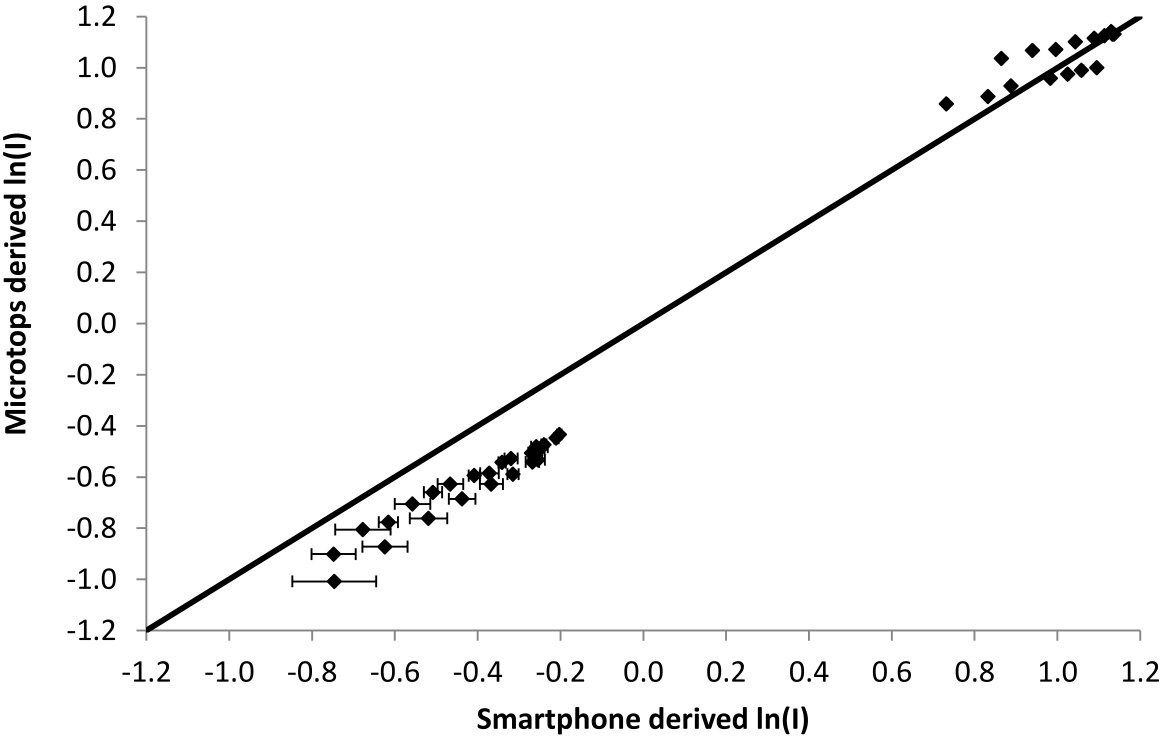

Figure 36: ln(I) comparison for all combined observations of all smartphones at both target wavelengths. The one-to-one equivalence line is in bold.

5.4.2.3 AOD comparisons and validation

The aerosol optical depth (AOD) is calculated employing the Beer-Lambert Law (equation 7), using the smartphone derived direct UV irradiance. Each calibration test was following by a validation set of data on a different day to determine if the AOD values from the smartphone continue to match those from the Microtops sunphotometer. Microtops and smartphone derived aerosol optical depth are compared in three ways:

- All combined data, using AOD values derived from the combined data calibration algorithms.
- Combined 340 nm and 380 nm data, using AOD values derived from the 340 nm and 380 nm grouped data calibrations.
- Combined individual smartphone calibration and validation AOD data.

The smartphone derived irradiance possesses the dominant error, as θ_{SZA} and P errors are far smaller. $I_{0\lambda}$ and $\tau_{Rayleigh}$ are constants depending on the wavelength used and P_0 is constant at 1013.25 hPa. However, $\cos\theta_{SZA}$ is a scaling multiplier to the derived irradiances. Thus, for error analysis, the AOD formula becomes

$$AOD = k\ln\left(I_{Smartphone}\right) \qquad [28]$$

where k is the $\cos\theta_{SZA}$ scaling multiplier.

Using the calculus approach described by Hughes and Hase (2010), the error for aerosol optical depth can be calculated as being,

$$\alpha_{AOD} = |k|\alpha_{\ln(I_{Smartphone})} \qquad [29]$$

AOD comparisons between the smartphone and the Microtops sunphotometer are presented in 3 ways:

- The average discrepancy is 35% (Figure 37), when the AOD derived from the algorithm combining all target wavelengths and smartphone data (derived from equation 24 and Figure 36) is compared with the Microtops sunphotometer.
- The average discrepancy is 28% (Figure 38), when the AOD derived from the algorithms of the combined smartphone calibrated data for each of the target wavelengths (derived from equations 22 and 23; and Figure 32 and 35) is compared with Microtops sunphotometer.

Several calculations gave negative AOD values, which are nonsensical and are indicative of the weakness of these calibrations. The data for the combined calibration data had the most variation.

- When individual smartphone calibrated and validated AOD data (based on equations 17-21) are compared to Microtops sunphotometer observations and plotted together (Figure 39), the average discrepancy of the smartphone derived and validated data was 4%.

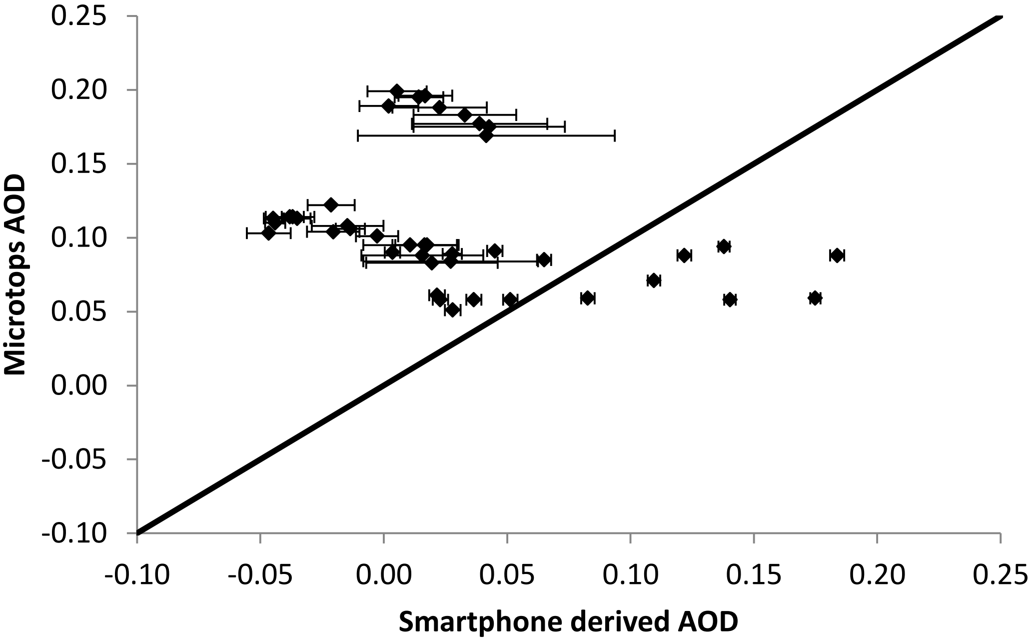

Figure 37: Comparisons between smartphone and Microtops sunphotometer data for combined smartphone calibration.

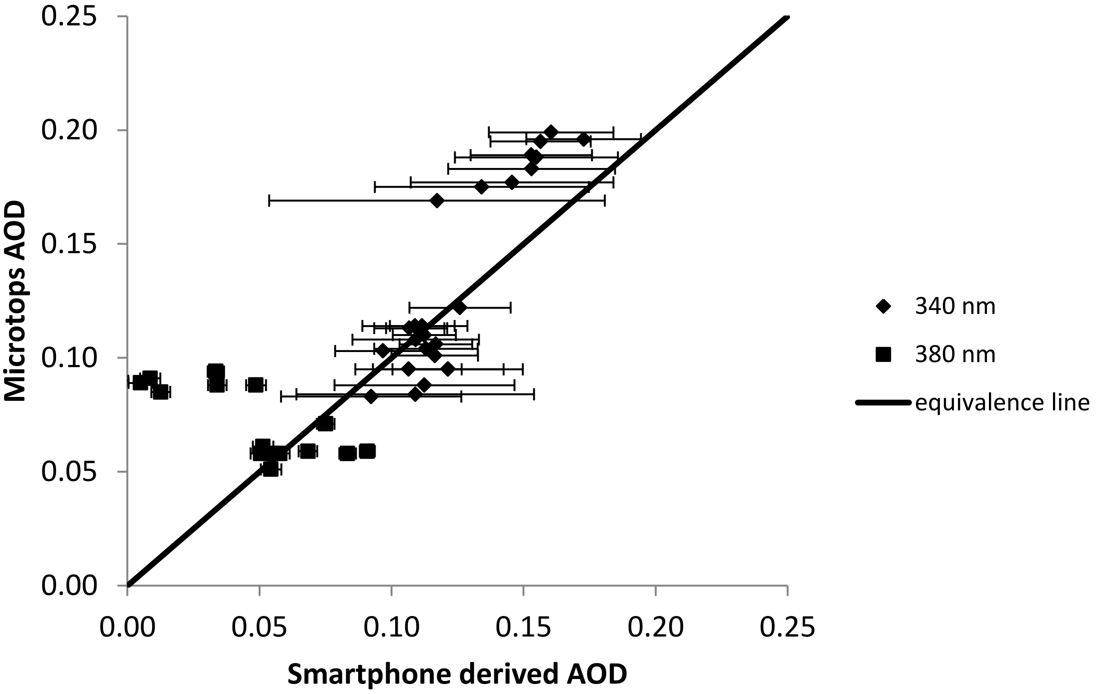

Figure 38: Comparisons between smartphone and Microtops sunphotometer data for target wavelength calibrations (as indicated by the key).

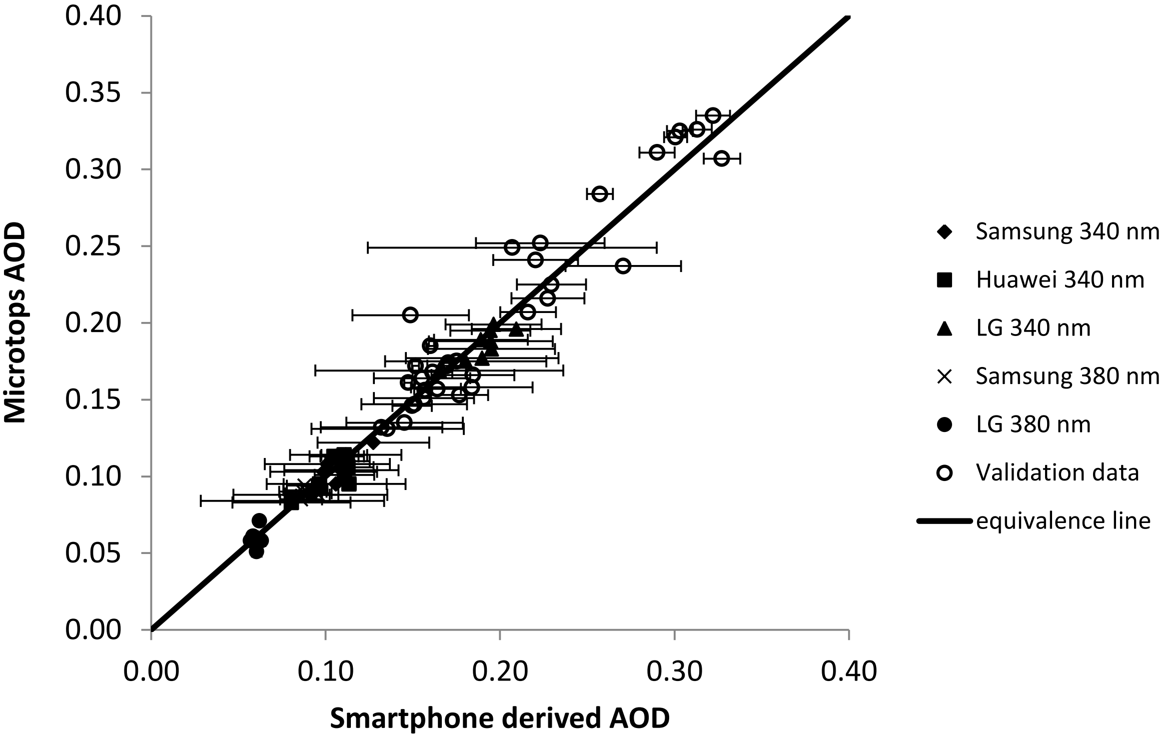

Figure 39: Comparisons between smartphone and Microtops sunphotometer data for individual smartphone calibrations (as indicated by the key).

5.4.3 Signal to Noise Ratio

The signal to noise ratio (SNR) is a measure of the useful signal compared to the background noise. The mean (μ) of the brightest pixel values are compared to their standard deviation (σ) (Gonzales and Woods, 2008; Firbank et al. 1999). The ’20 log’ rule is then applied to give the SNR in decibels as in equation 30 (Nakamura, 2006).

$$SNR = 20\log\left(\frac{\mu}{\sigma}\right) \qquad [30]$$

The grey digital numbers from all smartphone tests retained near constant SNR values, independent of the incident irradiance. Each SNR varied across the different brands, with the SNR considerably higher for 380 nm observations than those made at 340 nm, with the latter retaining the most consistent SNRs (Figure 40). The error bars are the standard deviation of the SNR across the tests performed on each phone.

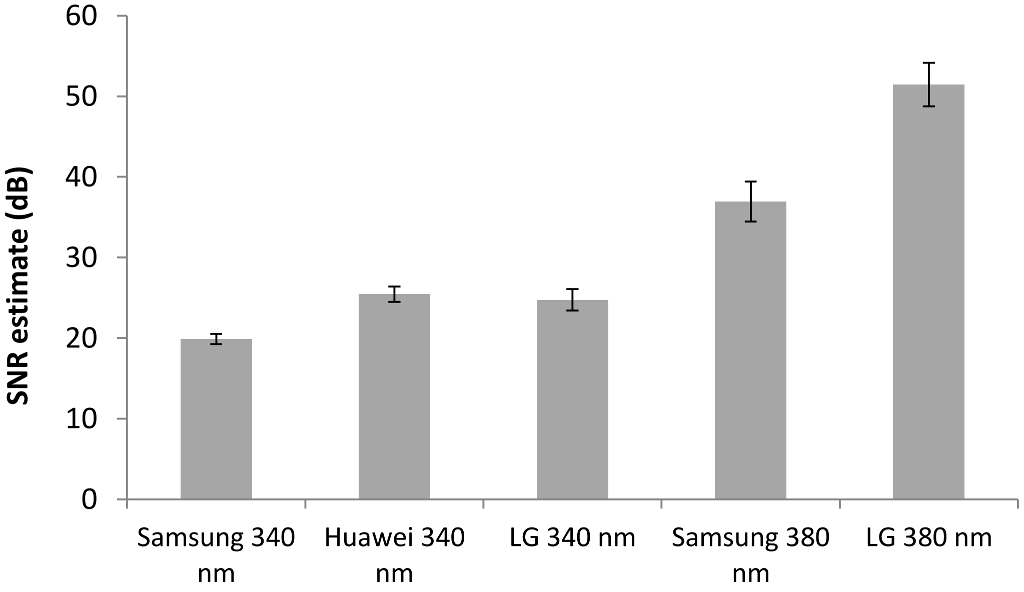

Figure 40: SNR values for each smartphone test.

5.5 Discussion

Noise

All smartphones exhibited reasonably constant and a low level of DFPN which did not vary significantly with a significant temperature change (Table 1). Temperature changes throughout the field calibration tests also exhibited negligible effects of temperature change and direct sunlight on the image sensor.

Calibration

Most of the smartphones tested performed well in field tests, the Samsung Galaxy 5 and LG Optimus adequately endured prolonged exposure to field conditions, which included direct sunlight on the casing. However, the Huawei U8180 failed to work for most of the 380 nm test and the images obtained demonstrated some form of damage in the internal computing of the phone rather than the camera, as a couple of solar images were able to be obtained. This demonstrates the great need to insulate the phone or, preferably shield the phone from the direct sunlight between measurements to prevent overheating. The thermally based dark current on all three smartphones was found to be negligible for temperatures between 17°C and 37°C.

The natural log of direct irradiance derived for each narrow waveband from each smartphone image sensor tested demonstrated a very strong correlation with those derived from the Microtops, providing a strong case for the use of the $\cos^4\theta_{SZA}$ correction to the average grey responses, as described by Smith (2000) and Hauftecker (2000). The calibrations for each smartphone made at 340 nm provided a very slightly higher correlation than those taken at 380 nm, having a correlation coefficient of above 0.99 and 0.97 respectively. When the calibration was calculated for all of the smartphone and target wavelength data combined, the correlation was also found to be very strong at 0.99. However, when the data was grouped by target wavelength, the correlation coefficients were significantly lower at 0.93 and 0.76 for 340 nm and 380 nm respectively.

The grey response at 380 nm with increasing incident solar irradiance was less affected by atmospheric scattering than that observed at 340 nm, as indicated by the gradients calculated from the calibration regressions at those wavelengths (Igoe et al. 2013c). The gradient for the Samsung Galaxy halved approximately, whereas the gradient was reduced to a third in the LG Optimus. Equations 17-21 demonstrate that each of the smartphone's image sensors respond independently from each other, primarily as each manufacturing company has different proprietary processes. Individual differences may also exist from phones of the same type due to differences in manufacturing quality assurance.

All errors and signal to noise ratios (SNRs) were consistent within each set of observations, showing no significant variation with increasing incident solar irradiation. However, as with the calibration regression, each smartphone image sensor possessed unique errors and signal to noise ratio response to the target wavelength. The greatest difference in SNR was observed in the 380 nm tests, where the LG Optimus has a superior SNR to the Samsung by approximately 40%, a similar trend was observed for the 340 nm tests. The average error at 340 nm was approximately 8 times higher than that observed at 380 nm, consequently, the SNR at 380 nm was over double that of 340 nm. The errors for the gradient and the intercept were considerably higher with 340 nm calibrations than at 380 nm.

ln(I) comparison

When the natural log of direct irradiances derived from the smartphone were compared to those derived from the Microtops, it is clear that the individual smartphone calibrations provide an improved accuracy than for the calibrations of all the data combined or for when the data were grouped by target wavelengths. The average discrepancy from the Microtops data were typically 4% or less using calibrations for each individual smartphone, rising to 6% when the data were grouped according to target wavelength and 26% for all combined data. The LG Optimus demonstrated the least average discrepancy overall.

The 340 nm data tended to either fall on or under the one-to-one equivalence line, indicating a tendency for the smartphone image sensor to slightly underestimate the irradiance, this is reflected when target wavelength data, and especially when all data are combined (Figure 32 and Figure 36 respectively). A similar trend was not noted for observations at 380 nm; however, despite the low discrepancies, there is an apparent degree of sensitivity to prevalent conditions when observations are being made, particularly the presence of high level clouds.

The errors observed at 340 nm were on average, 10 times more than those observed for 380 nm tests. The errors at 340 nm behave considerably differently to those at 380 nm, decreasing with increasing irradiance, but only as the air mass decreases. As SNR is constant with increasing irradiance, this phenomenon is likely to be as the effects of the increased atmospheric scattering that radiation at 340 nm experiences due to the air mass increases (Verhoeven and Schmitt, 2010; Liuo, 2002).

AOD comparison and validation

Individually, each smartphone image sensor yields a very strong match with the measured AOD in comparison to those observed on the Microtops. In comparison, when the data are grouped according to target wavelength and combined together it does not provide reasonable comparative data. The combined data algorithm also yielded nonsensical negative AOD values. The average discrepancy from Microtops observations for each individual smartphone calibration and validation test was 4%, reaching a maximum of 7%. This is much more favourable than the 28% average discrepancy for target wavelength grouped data and 35% average discrepancy for all combined data; maximum discrepancies reached over 100% for both combinations (the highest being an unacceptable 380%).

Similar to what was observed with the ln(I) comparisons, the error observed at 340 nm was on average 10 times more than that observed at 380 nm. All errors for each smartphone test were reasonably consistent, largely independent of air mass, but showing some sensitivity to local aerosol conditions and changes.

5.6 Chapter Summary

The data, analysis and comparisons of ln(I) and AOD indicate that each phone responds considerably differently to direct UV irradiance at 340 nm and 380 nm. The main indicators being the calibration regression gradient and the image sensor's SNR. These observations strongly preclude any algorithm being possible that involves combined wavelength data as well as any 'one size fits all' algorithm for all phones. The LG Optimus, overall, demonstrated superior SNR and consistent comparisons for both target wavelengths. For each wavelength, calibration gradients and intercepts of each phone are independent of each other. The results indicate that the smartphone image sensor, with additional external narrow bandpass and neutral density filters can be used as a field sensor to evaluate solar UVA irradiance and aerosol optical depth after undergoing extensive calibration and validation.

6. Android Automation

This section will describe and analyse the automation of smartphone detection and calculation of direct solar UVA irradiance and aerosol optical depth. Automation is achieved by writing and implementing smartphone-based *Android* code to perform calculations based on the smartphone calendar and clock alongside sensory data obtained from the image sensor.

6.1 Android Schematics

The following is a brief overview of the *Android* system, a full in-depth analysis of how *Android* works is beyond the scope of this research. There are many resources that assist in explaining how the Android system works, the most authorative being the Android Developers Guide (android.com). The *Android* system is a software stack based on a Linux kernel based operating system that is partly written in the *C* and *C++* programming languages (Ableson et al. 2011; Gandhewer and Shiekh, 2010). The operating system controls the core services, including processes, memory, filesystem management and hardware specific drivers, such as for the camera (Mednieks et al. 2012; Ableson et al. 2011).

Java is the main programming language used in developing the app and is an object orientated language focussing on a combination of data and procedures referred to as a ‘class’ (Mednieks et al. 2012). The runtime environment is known as the *Dalvik Virtual Machine (VM)* and contains the core *Java* packages and libraries; however, the *Android* environment is not exactly the same as the *Java ME* environment (Ableson et al. 2011; Gandhewer and Shiekh, 2010).

A major aspect of programming in the *Android* environment is the use of an “Intent”, which is a ‘declaration of need’ or in other words, a unit of communication between sections of code within the app, primarily made up of information used to describe the desired action (Mednieks et al. 2012; Ableson et al. 2011).

There are four main components of *Android* programming: activities, services, broadcast-receivers and content-providers, all of which can be called by an intent (Mednieks et al. 2012; Ableson et al. 2011). An activity is a programming unit of user interaction and code execution (Mednieks et al. 2012). The app developed and tested for this research uses a single activity, controlled by an intent. The calculations were not complex enough to require background services, at no time was there any need to send or receive data using the broadcast receivers and no database was needed for its use, hence no need for content-providers.

XML is another essential programming language used in the Android environment. Three important *XML* files must be included as part of any app (Ableson et al. 2011):

- The AndroidManifest.XML file is a root file of any app, containing all design-time relationships, intents, deployment descriptions and hardware permission declarations (Mednieks et al. 2012; Ableson, 2011).

- The Main.XML file declares the assignment attributes for UI (user interface) components (e.g. radio boxes, text entry boxes) as well as defining the UI layout (Mednieks et al. 2012; Ableson, 2011).

- The Strings.XML file defines the names of the elements used in the app (Mednieks et al. 2012; Ableson, 2011).

Programming and testing the app via an emulator is usually performed using a freely downloadable program such as *Eclipse* which allows for a simulation of the smartphone environment on a computer (Mednieks et al. 2012; Ableson et al. 2011; Gandhewer and Shiekh, 2010).

6.2 Android Requirements to Calculate Direct Irradiance and AOD

The initial user interface consists of the following components (Figure 41):

- A radio box to select the target wavelength (340 nm or 380 nm). This is set so that one of the target wavelengths must be selected before the program can proceed by being on 340 nm by default.
- A text entry box to enter the station elevation in metres. A reminder is automatically written in the text box, disappearing when the user enters their station elevation. To prevent errors from this text box being empty or having a ‘null’ value, the default value is set at 0 metres.
- A text entry box to enter the station latitude. As for the elevation entry, a reminder is automatically written in the text box, also stating the user to write southern hemispheric latitudes as negative values. To prevent null values, the default is set to the Toowoomba, Queensland latitude (27.56°S or -27.56°).
- A button labelled ‘Proceed’ is then pressed, temporarily saving the values entered, to proceed to the next task.

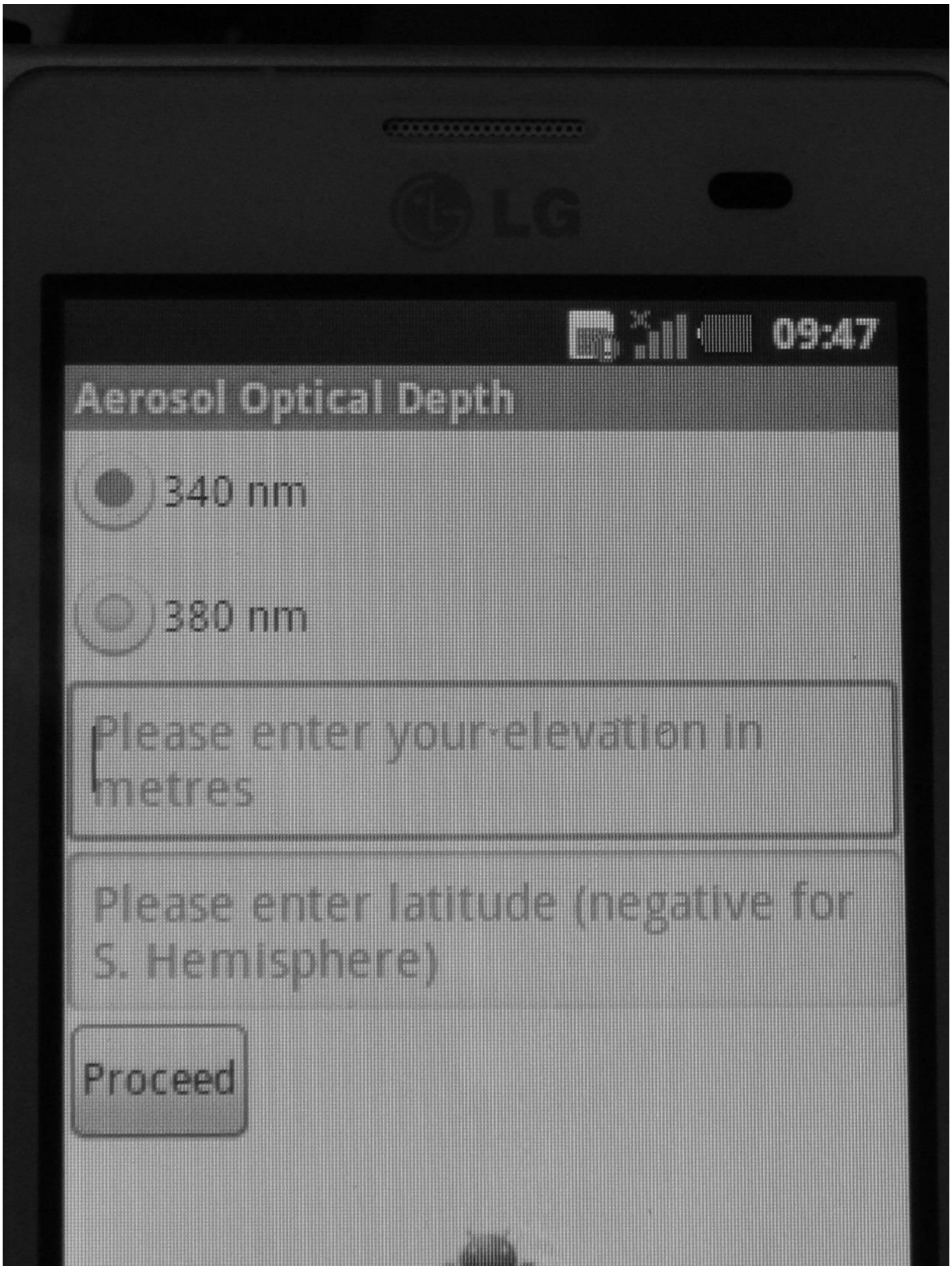

Figure 41: User interface of the automated Android app for determining direct solar UVA irradiance and AOD on a smartphone. (Photo taken using another smartphone).

Smartphones have a GPS that can detect via satellites or Wifi towers, the local latitude, longitude and elevation. However, in field tests, while the latitude and longitude proved to be accurate, the elevation varied significantly, by up to 1.2 km in field tests. This occurred on all phones tested. Additionally, in remote areas, the acquisition of the necessary signals would not be assured due to the lack of reference points. The app subsequently requires the user to enter the elevation and latitude.

The automation process is summarised in Figure 43 and explained in detail here.

Once the 'Proceed' button is clicked, the user interface is hidden and the camera is immediately activated by a camera-intent. This is in the place of using the full camera programming functions, which are unnecessary for this app. The camera is opened just as in normal use, allowing the user to check that the settings are at their default, as they were in the research performed by Igoe et al. (2013c), including the photo being saved in the default jpeg format. The intent is intercepted and the photo taken is converted to a bitmap array, via a content resolver that exactly determines the location of the stored image.

The next task is to retrieve the grayscale (intensity) data from the captured image bitmap. Each pixel from the captured image bitmap is converted to grayscale by equation 13 (Malacara, 2002). The converted pixel digital values are stored as a separate grayscale bitmap array. To simplify the *Android* app running time, a threshold was determined by observing the minimum grey value corresponding to the diameter of the solar disk in the captured images taken for both 340 nm and 380 nm. This threshold value was found to be consistent for both target wavelengths at an approximate digital number of 20. The average of the grayscale pixel values above the threshold is then calculated for each captured image. Although this calculation is different to the one used by Igoe et al. (2013c) and in the previous chapter, the thresholded average grey values were found experimentally to be similar to the values determined in the previous research.

After determining the average grey response, the Sun-Earth distance correction was calculated as is used by the Microtops sunphotometer (equation 3) (Morys et al. 2001; Porter et al. 2001). This task requires the use of the smartphone internal calendar, accessed via Java code, converting the date into a ‘day of year’. This correction is applied to the average grey value as it was in Igoe et al. (2013c).

The next stage is to determine the sun position for the date and time of the observation, using the latitude (*la*) entered initially and calculations of declination (*decl*) (equation 31) and hour angle (*ha*) (equation 32) based on the date and time (Wenham et al. 2012).

$$decl = 23.45° \sin\left[\frac{360° \, (d-81)}{365}\right] \tag{31}$$

where d is the calendar day of the year. The day of the year is calculated as a decimal float value to account for the time of the day.

$$ha = 15° \, (h - 12) \tag{32}$$

where h is the hour of the day.

The cosine of the solar zenith angle is used in the Beer-Lambert Law, as from equations 5 and 7. Thus $\cos\theta_{SZA}$ is determined using equation 33 (Wenham et al. 2012),

$$\cos\theta_{SZA} = \sin(decl)\sin(la) + \cos(decl)\cos(la)\cos(ha) \qquad [33]$$

The fourth power of this term is multiplied with the average grayscale value as in Igoe et al. (2013c) to give an expression for ‘cosine grey’, as in equation 12 and 14.

The next stage is to estimate the station air pressure correction to the Rayleigh optical depth (refer to equation 7). Although the most modern smartphones possess an internal barometric sensor, the majority of smartphones currently in common use do not. Consequently, as a substitute, the barometric formula was used to determine the pressure (P) at the specified elevation (z) as in equation 34, valid up to 6 km in elevation (Berberan-Santos et al. 1996).

$$\frac{P}{P_0} = e^{\left(-\frac{mgz}{kT}\right)} \qquad [34]$$

The molecular mass of air (m), acceleration due to gravity (g) and absolute temperature (T) are assumed to be constant at 28.95 amu, 9.81 $\mathrm{ms^{-2}}$ and 288 K respectively. The Boltzmann constant (k) is 1.3806488 x 10^{-23} $\mathrm{m^2\ kg\ s^{-2}\ K^{-1}}$. The ratio of air pressure at elevation and mean sea level pressure (1013.25 hPa) is used to correct the Rayleigh optical depth at the target wavelengths of 340 nm and 380 nm, which are constants in the Android app at 0.7125 and 0.4436 respectively (Bodhaine et al. 1999).

A final correction to the average grayscale values for the 380 nm tests are needed to take into account the increased attenuation of the additional ND2 filter used in the observations (Igoe et al. 2013c). The final calculations are to determine the direct UV irradiance and AOD, constants used in these stages depend on the wavelength selected in the initial user interface. The natural log of the irradiance is determined by equation 14, and as the tests were performed on an LG phone, the regression constants used in equations 20 and 21 were programmed in as constants.

The final calculation is to determine the AOD. The natural log of the extraterrestrial irradiances used as constants in the Microtops was programmed as constants for the Android app. The natural log of the direct irradiance calculated in the step before is subtracted from the natural log of the extraterrestrial irradiance, this difference is multiplied by the calculated cosine of solar zenith angle and has the corrected Rayleigh optical depth taken from it as per equation 7.

The entire activity takes less than a second to complete all pixel conversions and calculations. In timed tests, the average time for completion was 0.22 seconds. Once all calculations are complete, the user is returned to the initial user interface and a dialog box with the calculated solar zenith angle, average grayscale value, direct irradiance and AOD are shown (Figure 42). Once the user has noted the results, they can exit the dialog box and be at the initial user interface to be able to perform the next test if desired.

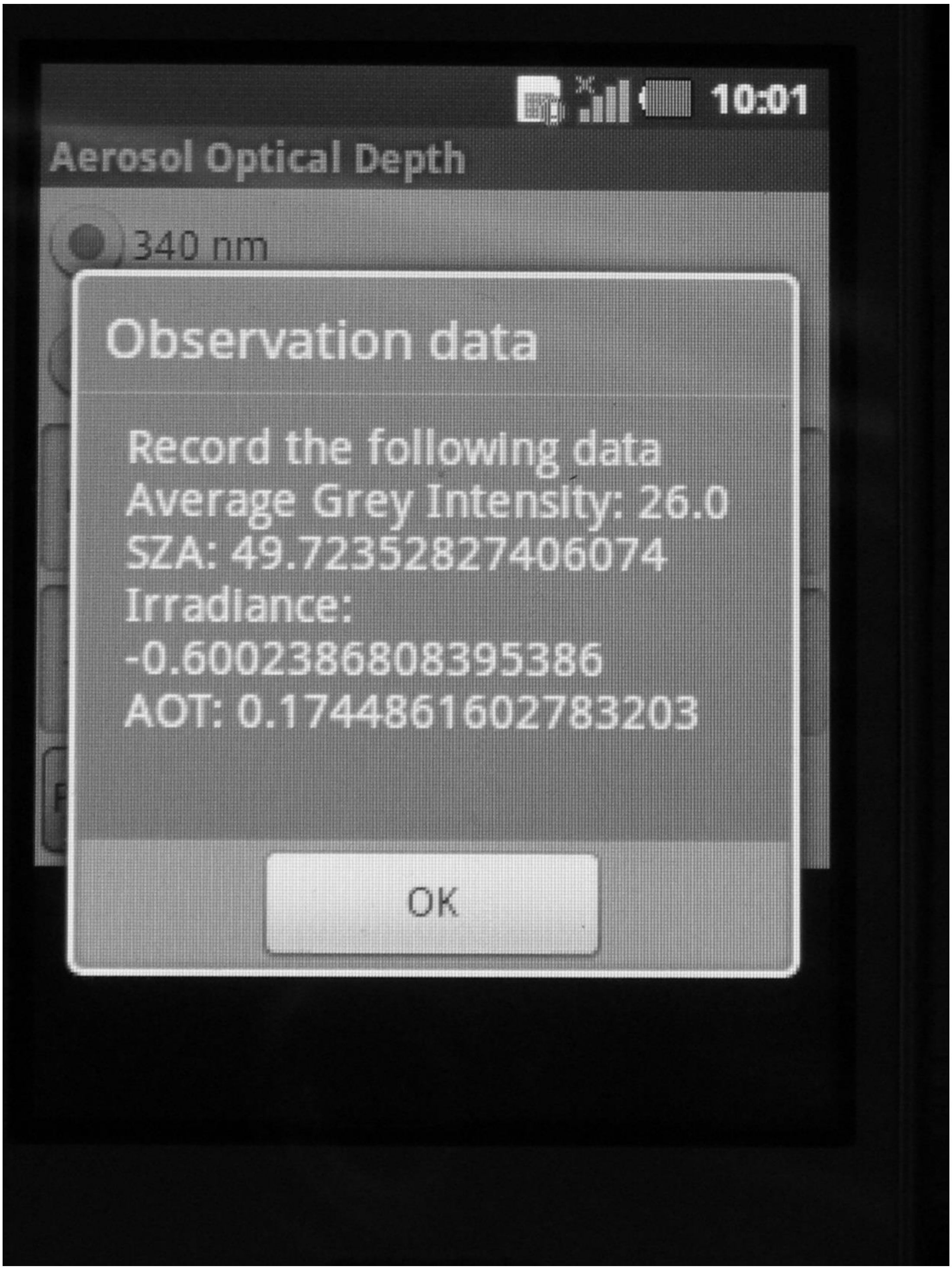

Observation data

Record the following data
Average Grey Intensity: 26.0
SZA: 49.72352827406074
Irradiance:
-0.6002386808395386
AOT: 0.1744861602783203

Figure 42: Raw data dialog box as the final stage of the Android app calculations (note, the irradiance value is actually its natural log). The apparent precision in the data is due to the simplicity in the app code.

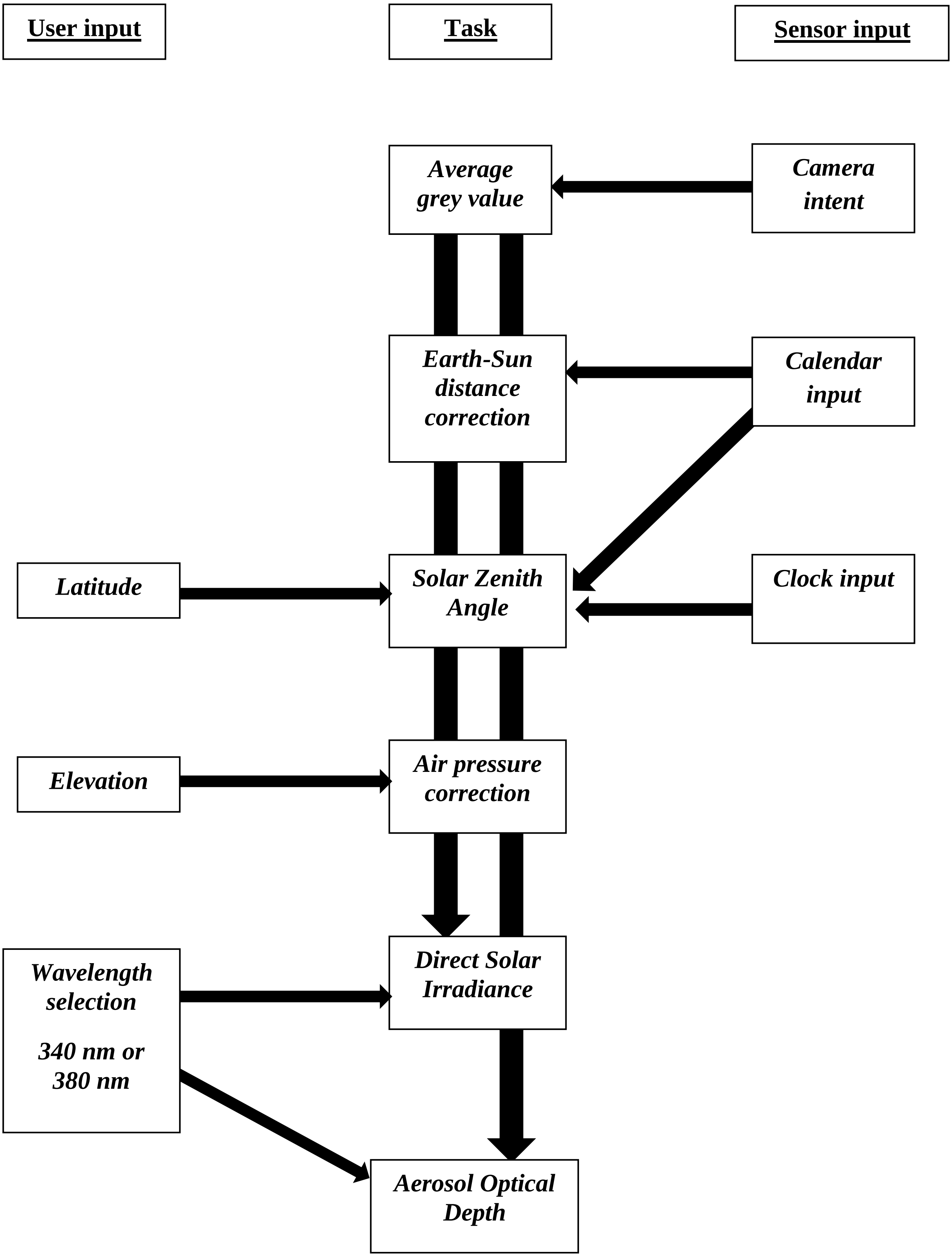

Figure 43: Flowchart of tasks and their dependencies in the Android app used for measuring direct solar irradiance and AOD at 340 nm and 380 nm.

6.3 Recalibration of Direct Irradiance and AOD

The regression calibration constants determined in the field calibration tests (outlined in section 5.4.2.1) needed to be recalibrated due to the following factors:

- The smartphone used for testing the *Android* app was an LG Optimus L3, similar to the one used in previous studies by Igoe et al. (2013c), representing a 4th phone used in the overall research. The only differences in the previous and present study smartphone is that the one used in this aspect of the study has a slightly more advanced *Android* version (version 2.3.6 compared to 2.3.3), but the same *Android* functions work for both. Any potential differences in sensor architecture between the LG Optimus phones need to be taken in consideration via the calibration as details of the sensor architecture are LG proprietary information and unavailable. In order to maintain consistency, the same narrowband and neutral density filters used for the initial calibration tests were used to test the *Android* app.

- The difference in how data is gathered to determine the average grayscale value also needs to be taken into consideration. The calibration data took the top 100 grey pixels across 3 images and averaged them whereas the Android app averaged all grey pixel values above a threshold. However, the average grayscale pixel values recorded when testing the *Android* app were similar to those in the calibration tests for both the 340 nm and 380 nm target wavelengths.

The recalibration was performed in the same manner as outlined in section 5.4.2.1 and the results of this and subsequent validation tests are presented in the next section.

6.4 Calibration and Validation test results

6.4.1 Locations

The locations where field observations for both calibration and validation tests were made for this research were at private residences in Toowoomba, Queensland (27.56°S 151.96°E, elevation 690 m) and Plainland, Queensland (27.57°S 152.42°E, elevation 80 m). Observations were made between 9 am and noon at both locations at 30 minute intervals, over three consecutive weekends during Spring. The two sites were selected as they represented separate aerosol environments, Toowoomba situated on top of a range of hills within the Great Dividing Range and Plainland situated in the middle of farming land in the Lockyer Valley.

6.4.2 Potential sources of error

Potential sources of error of the direct irradiance and subsequently, AOD calculated from the recalibrated smartphone app are the calculated values for solar zenith angle and the station pressure calculations derived from the entered altitude. Observations of the errors of these parameters are outlined below:

- Throughout the recalibration and subsequent validation tests, the smartphone calculated solar zenith angle only varied from the Microtops by a maximum of 5%. This discrepancy decreased with decreasing zenith angle down to 0.01%. At solar noon, the values were roughly equivalent to each other.

- The other potential source of error is the altitude based pressure correction, there was only a maximum of 1% discrepancy between the smartphone derived pressure and that recorded on the Microtops.

6.4.3 Recalibration results

The field calibration steps (chapter 5) have been modified slightly to be able to be applied to the app. For this reason, the steps are referred to as ‘recalibration’. Figure 44 and Figure 45 compare the natural log of direct irradiance derived from the Microtops with that of the cosine grey values derived from the smartphone, as defined by equation 12. The precision for both target wavelengths was very high with correlation coefficients of 0.98. The error bars are the values calculated in section 5.4.2.1 and stated in Igoe et al. (2013c). The same trends in calibration precision occurred in this study as were observed in section 5.4.2.1 and by Igoe et al. (2013c).

The recalibrated regression at 340 nm was,

$$\ln I_{Microtops} = 0.2821(cosine\ grey) - 1.0339 \qquad [35]$$

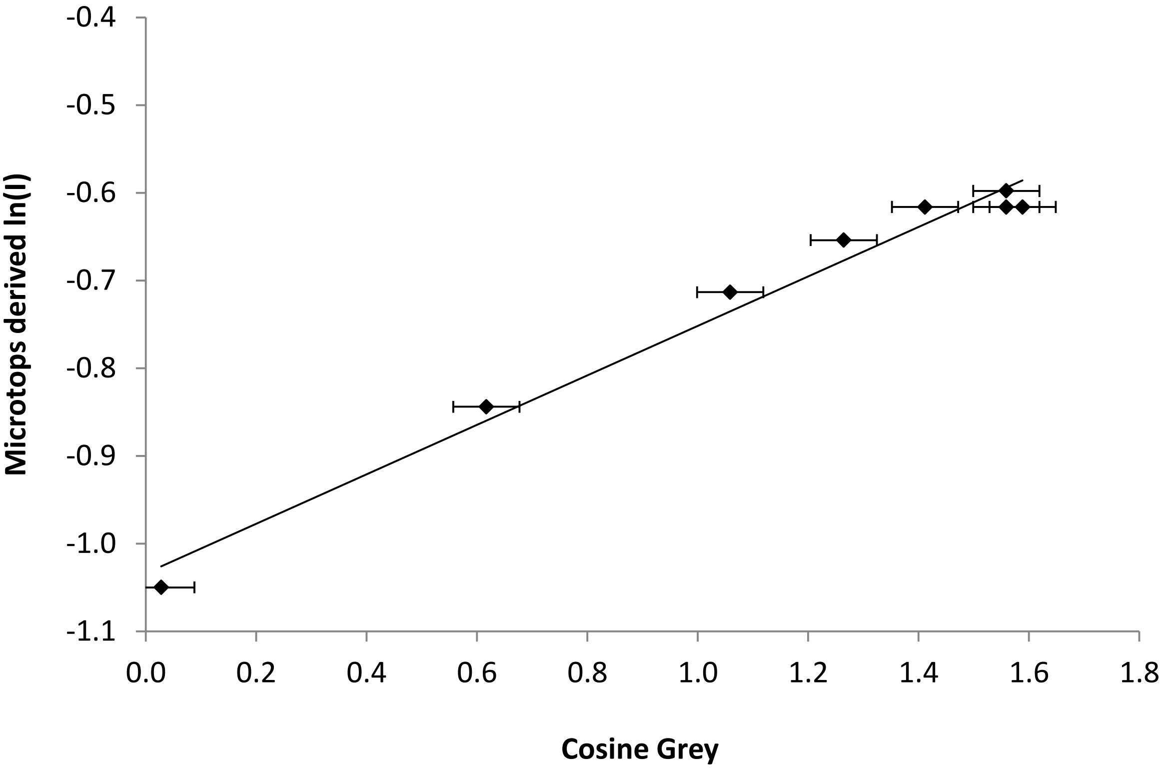

Figure 44: Recalibrated regression comparing the smartphone app derived cosine grey values with the natural log of Microtops measured direct irradiance at 340 nm.

The recalibrated regression at 380 nm was,

$$\ln I_{Microtops} = 0.1804(cosine\ grey) + 0.2462 \qquad [36]$$

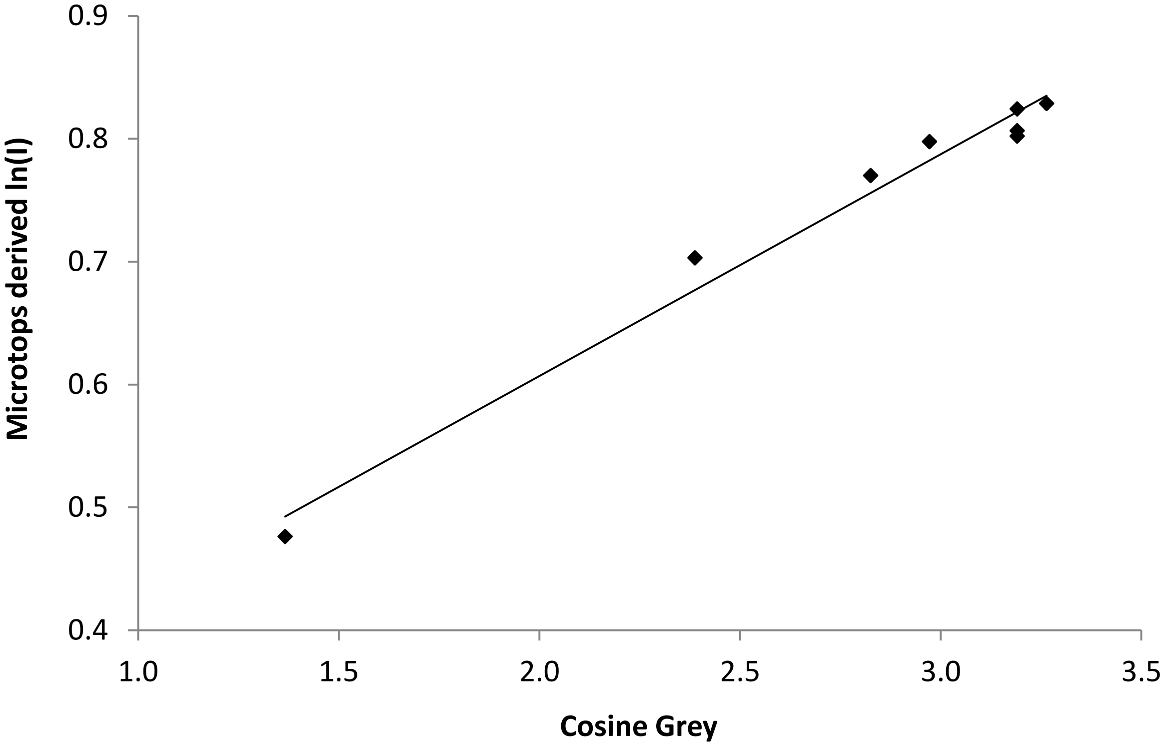

Figure 45: Recalibrated regression comparing the smartphone app derived cosine grey values with the natural log of Microtops measured direct irradiance at 380 nm. The error bars at this target wavelength are too small to be seen.

The gradients for 340 nm and 380 nm recalibration tests decreased and increased respectively when compared to the initial calibration tests by between 0.04 and 0.06. The change in the intercept was significantly less but following an opposite trend than the gradients.

6.4.4 Validation results

Using the recalibration regression constants derived in the previous section, three validation field tests were performed and the values for the natural log of direct irradiance and AOD were compared between those from the smartphone and the Microtops. Strong correlations exist between the irradiances and AOD data for both the 340 nm and 380 nm target wavelengths. Comparisons for the natural log of direct irradiances at 340 nm and 380 nm are shown in Figure 46 and Figure 47 respectively. The error bars for the 380 nm observations are too small to be seen. The corresponding AOD comparisons are shown in Figure 48 and Figure 49.

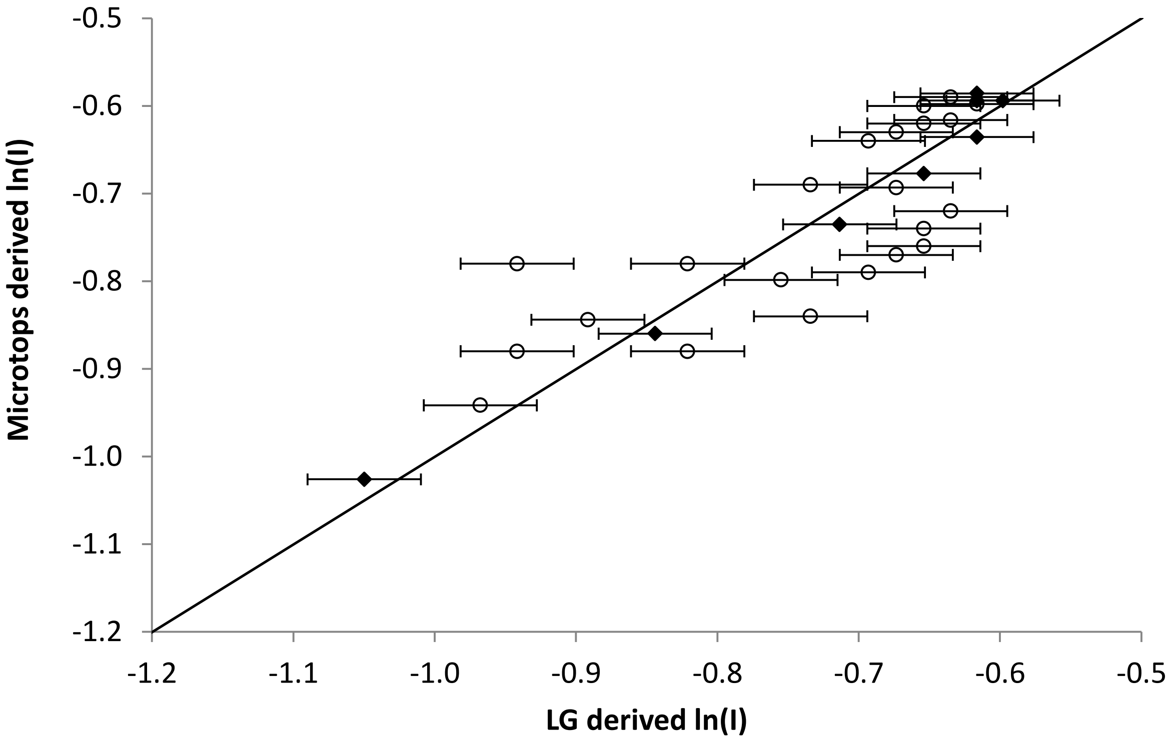

Figure 46: Comparison of the natural log of direct irradiances derived from observations from the smartphone app and the Microtops at the 340 nm waveband. The diamonds represent the recalibration data and the circles are the validation data. The line represents an exact match.

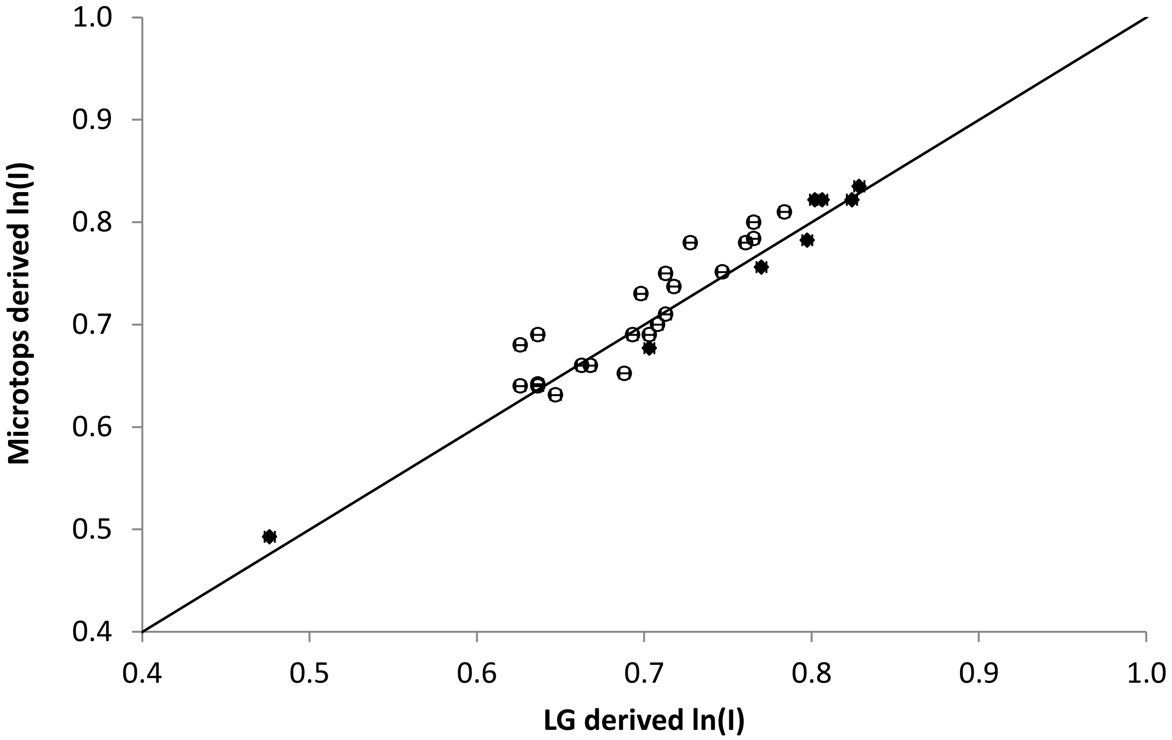

Figure 47: Comparison of the natural log of direct irradiances derived from observations from the smartphone app and the Microtops at the 380 nm waveband. The diamonds represent the recalibration data and the circles are the validation data. The line represents an exact match. The error bars are too small to be seen.

The comparisons were consistent with the results of the calibration test comparisons in section 5.4.2.2 and reported in Igoe et al. (2013c). The 380 nm waveband observations were more accurate and precise than those observed at the 340 nm waveband. The precision also increased as the solar zenith angle decreased. The average discrepancies for the 340 nm and 380 nm observations were 6% and 4% respectively.

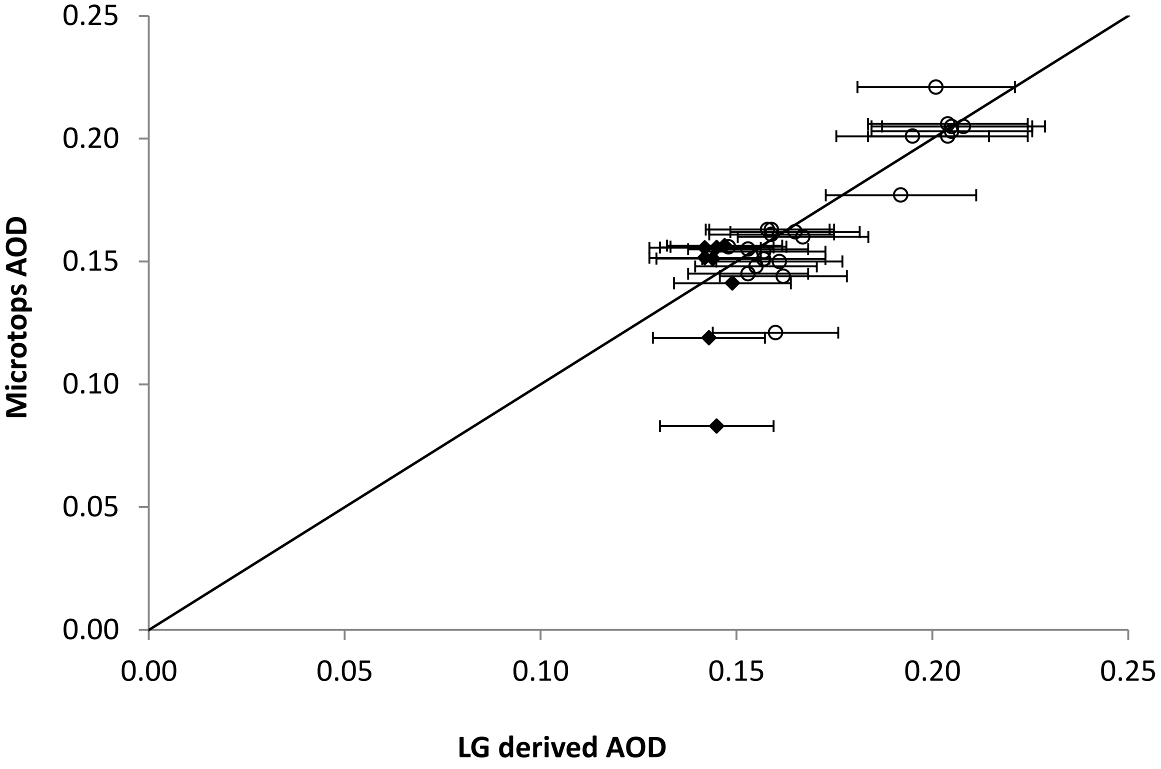

Figure 48: Comparison of the aerosol optical depths derived from observations from the smartphone app and the Microtops at the 340 nm waveband. The diamonds represent the recalibration data and the circles are the validation data. The line represents an exact match.

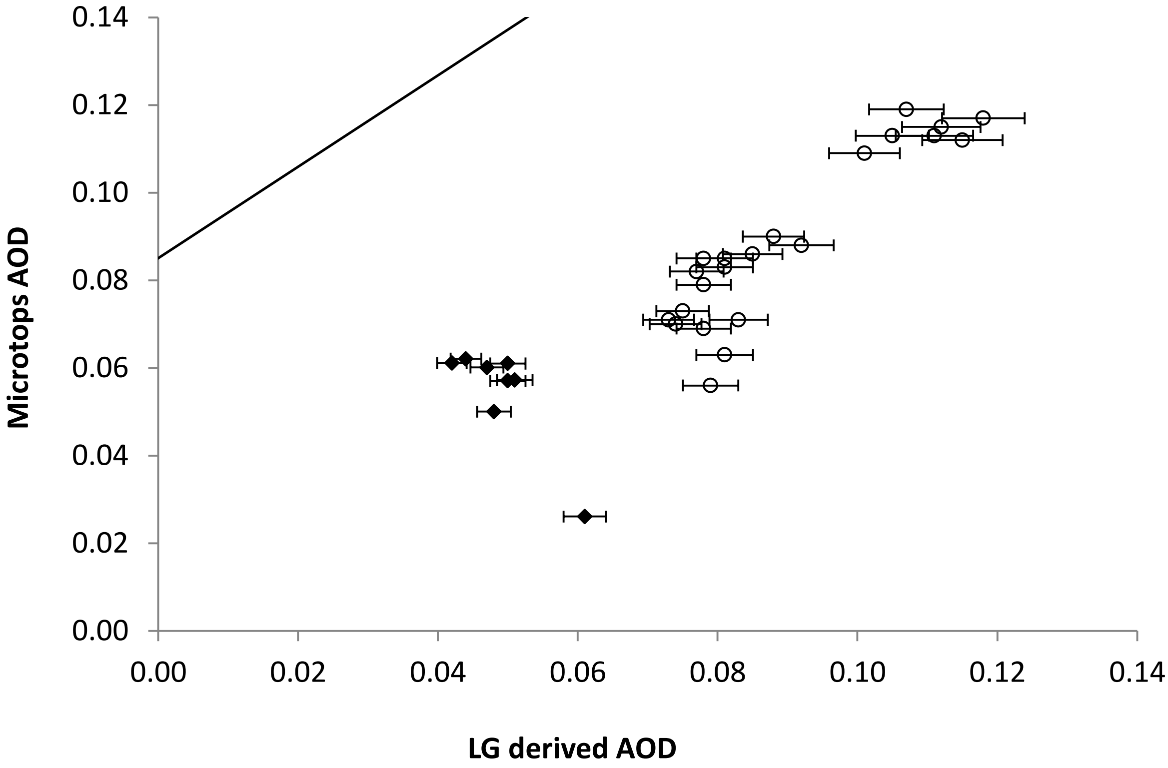

Figure 49: Comparison of the aerosol optical depths derived from observations from the smartphone app and the Microtops at the 380 nm waveband. The diamonds represent the recalibration data and the circles are the validation data. The line represents an exact match.

Generally, the AOD comparisons demonstrated a similar trend to the calibration observations presented in section 5.4.2.3 and in Igoe et al. (2013c). The aerosol optical depth values demonstrated far greater accuracy and precision at lower solar zenith angles, with the greatest deviations occurring at angles of greater than 60° (air mass greater than 2). The average discrepancies for both 340 nm and 380 nm observations were 8% (ranging between 10% and 6%). Inaccuracies also can be due to the presence of invisible upper level clouds, the increase in error in sun zenith angle calculations at higher zenith angles and air pressure variations.

6.5 Chapter Discussion

Once the regression calibration constants are recalibrated, the Android app provides an accurate measure of both direct UVA irradiance and AOD, particularly for solar zenith angles smaller than 60° (air mass less than 2). This correlates with McIntosh (2006)'s assertion that the approximation in equation 5 becomes more erroneous at air masses greater than 2. The observations at 340 nm were considerably more scattered and less accurate compared with those at 380 nm. This is consistent with the earlier calibration observations. The data were consistent at different locations and when tests were performed over a week apart.

Calibration and validation of the results were consistent with those of previous non-automated research demonstrating that automation of the calculations of the direct solar UVA irradiance and aerosol optical depth are feasible using the internal sensors and the Android programming platform, common in smartphones.

A major implication of the recalibration is the potential that by determining the quantities and subsequently changing the regression calibration constants in the relevant part of the code, the app could potentially be made to work on any smartphone, as has been demonstrated in recalibrating the constants for the two types of LG Optimus smartphone.

7. Conclusions

7.1 Conclusions

The three sets of tests: laboratory modelling, field and Android app based calibration and validation represent two general reference points that explain the overall findings of the research, these will be generalised to ‘lab tests’ and ‘field tests’ respectively in the conclusion, unless otherwise specified.

Throughout the research, several overall observations can be made:

- Even very low solar UVA irradiances result in saturation of the image sensor, requiring the use of neutral density filters. The most extreme case is for the 380 nm solar observations, where two such filters were required. All field-tests required the use of an ND1% neutral density filter that absorbed just over 99% of the incident UVA solar irradiance. This is likely due to the high energy that UVA photons possess compared to visible light. Although, most UVA photons are absorbed by the filters and camera lens, the ones that do go through have enough energy to create a signal.

- The signal for shorter UVA wavelength tests, particularly for the 340 nm field tests, was subjected to more variation than those at 380 nm. This observation applies to all aspects observed: calibration/validation, direct solar UVA irradiance and AOD. This is possibly due to the increased scattering experienced by shorter wavelength radiation in the atmosphere with increased air mass, this is seen with the decreasing error as the air mass decreased towards noon in the field tests. The solar aureole is also likely to have affected each wavelength differently.

- The research indicates that each phone possesses a unique response to UVA, whether it is of a different brand or a different version. This difference is more noticeable with direct solar UVA irradiances. The main causes of these differences are likely to be mainly due to specific image sensor architecture differences and in a minor part due to the thickness of the inner and outer lenses. As image sensor data is proprietary information, differences in phone architecture and manufacturing quality assurance must be taken into account by recalibration and validation.

- All of the image sensors demonstrate sensitivity to ambient conditions, particularly the presence of clouds, intermittent smoke and dust aerosols that occurred locally during tests. Particularly important to this are suspected invisible high level clouds. However, there is not a great sensitivity to increased heat, with thermal noise resulting in minimal fluctuations, as evidenced by the low overall errors. Dark current is also not a significant issue, despite being temperature dependent.

- The sensitivity extends to which mathematical function is used to extract the average grayscale pixel value. However, the accuracy of the calculated direct UV solar irradiance and AOD remains the same, particularly in the field tests.

> The use of formula-based solar zenith angles and station air pressure equivalents did not affect the accuracy significantly, particularly for air masses less than 2, resulting in discrepancies averaging 8%.

Laboratory and field tests yield two sets of distinct equations that best model their behaviour. A concluding generalisation can be developed for the natural log of direct UV irradiance ($\ln I_{UVA}$) for both, based on linearised rearrangements of equations 10, 11, 13 and 14, shown in equations 37 and 38 for the laboratory and field tests respectively:

$$\ln I_{UVA} \propto \left(\frac{G}{R+G+B}\right)^{2.5} \qquad [37]$$

$$\ln I_{UVA} \propto \ln(0.30R + 0.59G + 0.11B) \qquad [38]$$

The natural log of direct solar UV irradiance was proportional to the natural log of the intensity or grayscale response, whereas in the laboratory tests, the direct UVA irradiance was observed to be proportional to the 2.5th power of the chromatic green ratio. Equations 37 and 38 are distinct from each other due to the different conditions that they were observed in, primarily due to variations that typically occur in the environment. Specifically, laboratory tests were subjected to a low-power UV source of known and controllable intensity, whereas the field tests were subject to variations of distance to the UV source, unpredictable local aerosol and cloud cover, varying air masses and a varying UV irradiance. The accuracy and precision were much higher (higher correlation coefficients) for the field data than the laboratory data, this may be due to the amount of data used to determine the average grayscale response.

The objectives stated in section 1.3 have been fulfilled. Specifically:

1. It was found that it was feasible for several types of smartphone to determine and characterise useful UVA irradiances and AOD values focussed on the target wavelengths (340 nm and 380 nm).
2. Very accurate automated direct solar UVA irradiances and AOD values were able to be observed by the smartphone. The Android programming was able to perform this through manipulating image sensor grayscale responses and the use of the internal clock and calendar.
3. The main implication of this research is that using smartphone technology to determine the direct solar UVA irradiances and AOD, high spatial resolution real time monitoring of these crucial parameters is possible. Furthermore, the potential for greater involvement of the wider community through this readily accessible technology will further promote awareness and potentially positive action in terms of increased UV dose awareness and air quality considerations.

In addition, this research demonstrates another example of how consumer electronics can be used for scientific applications and provides another potential avenue for ‘Citizen Science’.

7.2 Future Research

The Android tests show that the regression constants can be changed to accommodate different smartphone image sensor architecture, requiring recalibration of these constants. Future programming could:

- Include the regression constants for at least the main image sensor architectures. A drop down list on the user interface would allow for its selection. However, determining the regression constants for all architectures is impractical for this study, owing to the considerable models available.

- Further extend and refine grayscale response by using sorting and thresholding algorithm, which potentially could lead to a single algorithm that would fit all image sensor models, and perhaps create a single algorithm for both target wavelengths.

Newer and currently more expensive smartphone models are being manufactured with a barometer installed. By accessing this sensor, the need for determining the elevation could potentially be negated. However, the accuracy of the station air pressure would need to be tested and any corrections applied, possibly in a similar method to recalibrating the regression constants for the image sensor. The barometer would also mean that the GPS sensor could be used with more confidence.

Geotagging the images taken would also be a potentially more accurate method of retrieving all of the information required. Geotagging would allow position (latitude and longitude) details to be extracted from the image, coupled with the barometric sensor, a far more accurate measure of direct UV solar irradiance and AOD is possible. The use of such a system would be dependent on battery and CPU usage, as well as how long it would take to run the algorithms and provide information.

Currently, the app presents a dialog box with the calculated and observed values for AOD and direct solar UV irradiance, but does not save them due to this app concentrating on the calculation algorithms. It is possible to have the data saved on the SD-card or internal memory of the phone, which can then be sent as a text file that could be opened in a graphing program such as Microsoft Excel for further analysis. Further developments of this research could include the deployment of a smartphone based monitoring system of direct solar UVA irradiances and aerosol optical depth across the nation (and the world), with the results being transmitted to a central database. This would provide an unprecedented spatial resolution and a subsequent greater understanding of how these affect all aspects of life.

The external setup that holds the bandpass and neutral density filters, while being effective for this research, would be cumbersome for everyday use. Further research can be potentially focused on integrating these components into the smartphone cover, as well as finding less expensive alternatives for the filters used. This development was beyond the scope of the current research. The system would also be accessible by schools, allowing them to determine the level of exposure to UVA radiation as well as allowing them to monitor the levels of aerosols within the school grounds, both from internal (e.g. from Manual Arts) and external sources (e.g. nearby traffic).

References

Ableson, W. Sen, R. King, C. and Ortiz, C. 2011, *Android in Action*, 3rd Edition, Manning Publication Co.

Adler-Golden, S. and Slusser, J. 2007, 'Comparison of plotting methods for solar radiometer calibration', *Journal of Atmospheric and Oceanic Technology*, vol. 24, pp. 935-938s

Agar, N. Halliday, G. Barnetson, R. Ananthaswamy, H. Wheeler, M. and Jones, A. 2004, 'The basal layer in human squamous tumors hHarbors more UVA than UVB fingerprint mutations: A role for UVA in human skin carcinogenesis', *Proceedings of the National Academy of Science,* vol. 101, pp. 4954-4959

Alakarhu, J. 2007, 'Image sensors and image quality in mobile phones', *Proceedings of the International Image Sensor Workshop*, June 7-10, 2007, Ogunquit, Maine, USA

Anton, M. Serrano, A. Cancillo, M. and Garcia, J. 2009, 'Influence of the relative optical air mass on ultraviolet erythemal irradiance', *Journal of Atmospheric and Solar-Terrestrial Physics,* vol. 71, pp. 2027-2031

Avvenuti, M. and Vecchio, A. 2008, Advances in ubiquitous computing: Future paradigms and directions, IGI Publishing

Bai, Y. Bajaj, J. Beletic, J. Farris, M. Joshi, A. Lauxtermann, S. Petersen, A. and Williams, G. 2008, 'Teledyne Imaging Sensors: Silicon CMOS imaging technologies for x-ray, UV, visible and near infrared', *Proceedings of the SPIE Conference on Astronomical Instrumentation*, 2008, Marseilles, France

Ballare, C. Caldwell, M. Flint, S. Robinson, A. and Bornman, J. 2011, 'Effects of solar ultraviolet radiation on terrestrial ecosystems, patterns, mechanisms and interactions with climate change', *Photochemical and Photobiological Sciences*, vol. 10, pp. 226-241

Behar-Choen, F. Martinsons, C. Vienot, F. Zissis, G. Barlier-Salsi, A. Cesarini, J. Enouf, O. Garcia, M. Picaud, S. and Attia, D. 2011, 'Light emitting diodes (LED) for domestic lighting: Any risks for the eye?', *Progress in Retinal and Eye Research*, vol. 30, pp. 239-257

Berberan-Santos, M. Bodunov, E. and Pogliani, L. (1996), 'On the barometric formula', *American Journal of Physics*, vol. 65, pp. 404-412

Berneburg, M. Plettenberg, H. and Krutmann, J. 2000, 'Photoaging of human skin', *Photodermatology, Photoimmunology and Photomedicine*, vol. 16, pp. 239-244

Bigelow, D. Slusser, J. Beaubien, A. and Gibson, J. 1998, 'The USDA ultraviolet radiation monitoring program', *Bulletin of the American Meteorology Society*, vol. 79, pp. 601-615

Bodhaine, B. Wood, N. Dutton, E. and Slusser, J. 1999, 'On Rayleigh optical depth calculations', *Journal of Atmospheric and Oceanic Technology*, vol. 16, pp. 1854-1861

Blue, A. Clark, A. Houston, S. Laing, A. Maneuski, D. Prydderch, M. Turchetta, R. and O'Shea, V. 2009, 'Optical and electrical characterisation of a back-thinned CMOS active pixel sensor', *Nuclear Instruments and Methods in Physics Research A*, vol. 604, pp. 215-217

Bluth, G. Shannon, J. Watson, L. Prata, A. and Realmuto, V. 2007, 'Development of an ultraviolet digital camera for volcanic SO_2 imaging', *Journal of Volcanology and Geothermal Research*, vol. 161, pp. 47-56

Bogaerts, J. De Munck, K. De Moor, P. Sabuncuoglo Tezcan, D. Ficai Veltroni, I. Lepage, G. and Van Hoof, C. 2007, 'Radiometric performance enhancement of hybrid and monolithic backside illuminated CMOS APS for space-borne imaging', *International Image Sensor Workshop*, Ogunquit, Maine, June 7-10, 2007

Breslauer, D. Maamari, R. Switz, N. Lam, W. and Fletcher, D. 2009, 'Mobile phone based clinical microscopy for global health applications', *PLoS ONE*, vol. 4, pp. 1-6

Campos, F. Ulson, J. Castanho, J. and Aguiar, P. 2012, 'Noise performance of time-domain CMOS image sensors;, *in* Yuri, I.(ed), *Photodiode – From Fundamentals to Applications*, InTech

Cancer Council Australia, 2012, *Skin Cancer*, http://www.cancer.org.au/about-cancer/types-of-cancer/skin-cancer.html accessed 29th December, 2012

Cheymol, A. De Backer, H. Josefsson, W. and Stubi, R. 2006, 'Comparison and validation of the aerosol optical depth obtained with the Langley Plot method in the UV-B from Brewer Ozone Spectrophotometer measurements', *Journal of Geophysical Research*, vol. 111, D16202

CIE (International Commission of Illumination), 2006, *Action Spectrum for the Production of Previtamin D_3 in Human Skin*, Publication no. CIE174

CIE (International Commission on Illumination), 1998, *Erythema Reference Action Spectrum and Standard Erythema Dose,* Publication no. CIE S007E-1998

Cullen, J. Page, R. and Misdorp, N. 2002, 'An overview of cancer pathogenesis, diagnosis, and management', *in* Meuten, D. (ed), *Tumours in Domestic Animals*', 4th edition, Ames, Iowa State Press pp. 3-44

Debevec, P. and Malik, J. 1997, 'Recovering high dynamic range radiance maps from photographs', *Siggraph '97,* 3-8 August, Los Angeles, pp. 369-376

Diffey, B. 2002, 'Sources and measurement of ultraviolet radiation', *Methods,* vol. 28, pp. 4-13

Diffey, B. 1991, 'Solar ultraviolet radiation effects on biological systems', *Physics of Medicine and Biology,* vol. 36, pp. 299-328

Diner, D. Ackerman, T. Anderson, T. Bosenberg, J. Braverman, A. Charlson, R. Collins, W. Davies, R. Holben, B. Hostetler, C. Kahn, R. Martonchik, J. Menzies, R. Miller, M. Ogren, J. Penner, J. Rasch, P. Schwartz, S. Seinfeld, J. Stephens, G. Torres, O. Travis, L. Wielicki, . and Yu, B. 2004, 'Paragon: An integrated approach for characterizing aerosol climate impacts and environmental interactions', *Bulletin of the American Meteorological Society*, vol. 85, pp. 1491-1501

Di Sarra, A. Ccciani, M. Chamard, P. Cornwall, C. DeLuisi, J. Di Iorio, T. Disterhoft, P. Fiocco, G. Fua, D. and Monteleone, F. 2002, 'Effects of desert dust and ozone on the ultraviolet irradiance at the Mediterranean island of Lampedusa during PAUR II', *Journal of Geophysical Research*, vol. 107, pp. 8135-8148

Dubovik, O. Holben, B. Eck, T. Smirnov, A. Kaufman, Y. King, M. Tanre, D. and Slutsker, I. 2002, ‘Variability of absorption and optical properties of key aerosol types observed in worldwide locations’, *Journal of the Atmospheric Sciences*, vol. 59, pp. 590-608

Estelles, V. Martinez-Lozano, J. Utrillas, M. and Campanelli, M. 2007, ‘Columnar aerosol properties in Valencia (Spain) by ground-based sun photometry’, *Journal of Geophysical Research*, vol. 112, D11201

European Machine Vision Association, 2010, *Standard for Characterisation of Image Sensors and Cameras*, EMVA standard 1288, Release 3.0

Fartasch, M. Diepgen, T. Schmitt, J. and Drexler, H. 2012, ‘The relationship between occupational sun exposure and non-melanoma skin cancer’, *Deutsches Arzteblatt International*, vol. 109, pp. 715-720

Fioletov, V. Griffioen, E. Kerr, J. Wardle, D. and Uchino, O. 1998, ‘Influence of volcanic sulphur dioxide on spectral UV irradiance as measured by Brewer spectrophotometers’, *Geophysical Research Letters*, vol. 25, pp. 1665-1668

Firbank, M. Coulthard, A. Harrison, R. and Williams, E. 1999, ‘A comparison of two methods for measuring the signal to noise ratio on MR images’, *Physics in Medicine and Biology*, vol. 44. pp. N261-N264

Fransen, M. Karahallos, A. Sharma, N. English, D. Giles, G. and Sinclair, R. 2012, ‘Non-melanoma skin cancer in Australia’, *Medical Journal of Australia*, vol. 197, pp. 565-568

Friedlaender, M. 2005, ‘Ultraviolet radiation and the external eye’, *International Ophthalmology Clinics*, vol. 45, pp. 49-54

Galindo, I. Frank, S. and Bravo, H. 1995, ‘Ultraviolet irradiances over Mexico City’, *Journal of the Air and Waste Management Association*, vol. 45, pp. 886-892

Gallo, O. Tico, M. Manduchi, R. Gelfand, N. and Pulli, K. 2012, ‘Metering of exposure stacks’, in Cignoni, P. ad Ertl, T. (eds), *Eurographics,* Oxford, Blackwell Publishing

Gandhewer, N. and Shiekh, R. 2010, ‘Google Android: An emerging software platform for mobile devices’, *International Journal on Computer Science and Engineering,* NCICT 2010 Special Issue, pp. 12-17

Gangl, M. Kocifaj, M. Videen, G. and Horvath, H. 2007, ‘Light absorption by coated nano-sized carbonaceous particles’, *Atmospheric Environment*, vol. 42, pp. 2571-2581

Gao, W. Slusser, J. Gibson, J. Scott, G. Bigelow, D. Kerr, J. and McArthur, 2001, ‘Direct-sun column ozone retrieval by the ultraviolet multifilter rotating shadow-band radiometer and comparison with those from Brewer and Dobson spectrophotometers’, *Applied Optics*, vol. 40, pp.3149-3155

Gies, P. 2003, ‘Australia has more than enough solar UV radiation’, *Clinical and Experimental Optometry*, vol. 86, pp. 71-73

Gies, P. Roy, C. Javorniczky, J. Henderson, S. Lemus-Deschamps, L. and Driscoll, C. 2004, ‘Global solar UV index: Australian measurements, forecasts and comparison with the UK’, *Photochemistry and Photobiology*, vol. 79, pp. 32-39

Goldman, J. 2011, *Why the iPhone 4 takes good low-light photos: BSI CMOS sensors explained!*, http://news.cnet.com/8301-17938_105-20030382-1.html , accessed 18th February, 2013

Gonzales, R. and Woods, E. 2008, *Digital Image Processing*, Boston, Prentice Hall

Grant, W. 2008, 'The effect of solar UVB doses and vitamin D production, skin cancer action spectra, and smoking in explaining links between skin cancers and solid tumours', *European Journal of Cancer*, vol. 44, pp. 12-15

Grant, W. and Holick, M. 2005, 'Benefits and requirements of vitamin D for optimum health: A review', *Alternative Medicine Review*, vol. 10, pp. 94-111

Hader, D. Kumar, H. Smith, R. and Worrest, R. 2007, 'Effects of solar UV radiation on aquatic ecosystems and interaction with climate change', *Photochemical and Photobiological Sciences*, vol. 6, pp. 267-285

Har, D. Son, Y. and Lee, S. 2004, 'SLR digital camera for forensic photography', In *Scientific, Industrial and Digital Photography Application V*, 19-21 January 2004, San Jose, California, USA, IS&T-SPIE, Bellingham, pp. 276-284

Harrison, L. and Michalsky, J. 1994, 'Objective algorithms for the retrieval of optical depths from ground-based measurements', *Applied Optics*, vol. 33, pp. 5126-5132

Harrison, L. Michalsky, J. and Berndt, J. 1994, 'Automated multifilter rotating shadow-band radiometer: an instrument for optical depth and radiation measurements', *Applied Optics*, vol. 33, pp. 5118-5125

Hauftecker, H. 2000, ‘Radiometry of imaging’, in Jahne and Hauftecker, 2000, *Computer Vision and Applications*, Concise Edition, Academic Press Inc. San Diego

Hayes, T. 2012, ‘Next-generation cell phone cameras’, *Optics and Photonics News*, vol. 23, pp. 17-21

Hockwin, O. Kojima, M. Sakamoto, Y. Wegener, A. Shin, Y. and Sasaki, K. 1999, ‘UV damage to the eye lens, further results from animal model studies: A review’, *Journal of Epidemiology*, vol. 9 suppl., pp. S39-S47

Hoffman, A. Loose, M. and Suntharalingam, V. 2005, ‘CMOS detector technology’, *in Belectic, J. (eds), Scientific Detectors for Astronomy,* pp. 377-402, Netherlands, Springer

Horvath, H. 1993, ‘Atmospheric light absorption – a review’, *Atmospheric Environment*, vol. 27A, pp. 293-317

Hoya Filters (n.d.) Special Effect Filters: NDx400, http://www.hoyafilter.com/products/hoya/oef-07.html, accessed 25th Feb. 2012

Hughes, I. and Hase, T. 2010, Measurements and their Uncertainties: A Practical Guide to Modern Error Analysis, New York, Oxford University Press

Hung, C. Fang, C. Al-Suwayeh, S. Yang, S. and Fang, J. 2012, ‘Evaluation of drug and sunscreen permeation by skin irradiated with UVA and UVB: Comparisons of normal skins and chronologically aged skin’, *Journal of Dermatological Science*, vol. 68, pp. 135-148

Ialongo, I. Casale, G. and Siani, AM. 2008, ‘Comparison of total ozone and erythemal UV data from OMI with ground-based measurements at Rome stations’, *Atmospheric Chemistry and Physics*, vol. 8, pp. 3283-3289

Igoe, D. 2011, *Analysing Urban Aerosols Using a Digital Camera*, unpublished MSc thesis, University of Southern Queensland

Igoe, D. Parisi, A. and Carter, B. 2013a, ‘Characterization of a smartphone’s response to ultraviolet A radiation’, *Photochemistry and Photobiology*, vol. 89, pp. 215-218

Igoe, D. Parisi, A. and Carter, B. 2013b, ‘Smartphones as tools for delivering sun-smart education to students’, *Teaching Science*, vol. 59, pp. 36-38

Igoe, D. Parisi, A. and Carter, B. 2013c, ‘Evaluating UVA aerosol optical depth using a smartphone camera’, *Photochemistry and Photobiology*, DOI: 10.1111/php.12082

Irie, K. McKinnon, A. Unsworth, K. and Woodland, I. 2008, ‘Measurement of digital image noise for imaging applications’, *Sensors and Transducers*, vol. 90, pp. 185-194

Jacobson, M. 2002, *Atmospheric Pollution: History, Science an Regulation*, Cambridge, Cambridge University Press

Jegou, F. Godin-Beekman, S. Correa, M. Brogniez, C. Auriol, F. Peuch, V. Haeffelin, M. Pazmino, A. Salag, P. Goutall, F. and Mahe, E. 2011, ‘Validity of satellite measurements used for the monitoring of UV radiation risk on health’, *Atmospheric Chemistry and Physics Discussions*, vol. 11, pp. 17375-17421

Jerram, P. Burt, D. Hibon, V. Vaillant, J. and Henrion, Y. 2010, ‘Back-thinned CMOS sensor optimisation’, *SPIE Photonics West,* San Fransisco, Jan, 2010

Kakani, V. Reddy, K. Zhao, D. and Sailaja, K. 2003, ‘Field crop responses to Ultraviolet-B radiation: A review’, *Agricultural and Forest Meteorology*, vol. 120, pp. 191-218

Kalashnikova, O. Mills, F. Eldering, A. and Anderson, D. 2007, ‘Application of satellite and ground-based data to investigate the UV radiative effects of Australian aerosols’, *Remote Sensing of Environment,* vol. 107, pp. 65-80

Kalashnikova, O. Mills, F. Eldering, A. Anderson, D. and Mitchell, R. 2005, ‘The effects of smoke and dust aerosols on UV-B radiation in Australia from ground-based and satellite measurements’, *Proceedings of SPIE,* vol. 5886

Kamran, T. and Khan, S. 2007, ‘Solar radiation: Cutaneous hazards and their prevention’, *Journal of Pakistan Association of Dermatologists*, vol. 17, pp. 46-51

Kantzas, E. McGonigle, A. Tamburello, G. Aiuppa, A. and Bryant, R. 2010, ‘Protocols for UV camera volcanic SO_2 measurements’, *Journal of Volcanology and Geothermal Research,* vol. 194, pp. 55-60

Kazadzis, S. Bais, A. Amiridis, V. Balis, D. Meleti, C. Kouremeti, N. Zerefos, C. Rapsomanikis, S. Petrakakis, M. Kelesis, A. Tzoumaka, P. and Kelektsoglou, K. 2007, ‘Nine years of UV aerosol optical depth measurements at Thessaloniki, Greece’, *Atmospheric Chemistry and Physics,* vol. 7, pp. 2091-2101

Kimlin, M. 2008, ‘Geographic location and vitamin D synthesis’, *Molecular Aspects of Medicine,* vol. 29, pp. 453-461

Kohler, U. 1999, ‘A comparison of the new filter Ozonometer MICROTOPS II with Dobson and Brewer spectrometers at Hohenpeissenberg’, *Geophysical Research Letters*, vol. 26, pp. 1385-1388

Kokhanovsky, A. 2008, *Aerosol Optics: Light Absorption and Scattering by Particles in the Atmosphere*, Chichester, Praxis Publishing

Kollias, N. Ruvulu Jr. E. and Sayre, R. 2011, ‘The value of the ratio UVA to UVB in sunlight’, *Photochemistry and Photobiology*, vol. 87, pp. 1474-1475

Krutmann, J. 2000, ‘Ultraviolet A radiation-induced biological effects in human skin: Relevance for photoaging and photodermatosis’, *Journal of Dermatological Science*, vol. 23, Suppl. 1, pp. 22-26

Leitzell, K. 2008, ‘Aerosols over Australia’, http://nasadaacs.eos.nasa.gov/articles/2008/2008_aerosols.html accessed 6th March, 2012

Lenoble, J. Martin, T. Blumthaler, M. Philipona, R. Alboid, A. Cabot, T. de La Casiniere, A. Grobner, J. Masserot, D. Muller, M. Pichler, T. Seckmeyer, G. Scmucki, D. Toure, M. and Yvon, A. 2002, ‘Retrieval of the ultraviolet aerosol optical depth during a spring campaign in the Bavarian Alps’, *Applied Optics*, vol. 41, pp. 1629-1639

Lidon, F. Reboredo, F. Leitao, A. Silva, M. Duarte, M. and Ramalho, J. 2012, ‘Impact on UV-B radiation on photosynthesis – An overview’, *Emirates Journal of Food Agriculture*, vol. 24, pp. 546-556

Liuo, K. 2002, *An Introduction to Atmospheric Radiation*, 2nd ed. San Diego, Academic Press

Lohberger, F. Honninger, G. and Platt, U. 2004, ‘Ground-based imaging differential optical absorption spectroscopy of atmospheric gases’, *Applied Optics*, vol. 43, pp. 4711-4717

Luk, J. Torealday, S. Perry, G. and Pal, L. 2012, ‘Relevance of vitamin D in reproduction’, *Human Reproduction*, vol. 27, pp. 3015-3027

Lund, L. and Timmins, G. 2007, ‘Melanoma, long wavelength ultraviolet and sunscreens: Controversies and potential resolutions’, *Pharmacology and Therapeutics*, vol. 114, pp. 198-207

Luo, B. Yang, F. and Yan, L. 2010, ‘Key technologies and research development of CMOS image sensors’, *Second IITA International Conference on Geoscience and Remote Sensing*

Malacara, D. 2002, *Color Vision and Colorimetry: Theory and Applications*, Bellingham, SPIE Press

Maroulis, J. Nanson, G. Price, D. and Pietsch, T. 2007, ‘Aeolian-fluvial interaction and climate change: Source-bordering dune development over the past ~100ka on Cooper Creek, Central Australia’, *Quaternary Science Reviews*, vol. 26, pp. 386-404

McIntosh, G. 2006, ‘A simple photometer to study skylight’, *The Physics Teacher*, vol. 44, pp. 540-544

McKenzie, R. Liley, J. and Bjorn, L. 2009, ‘UV radiation: balancing risks and benefits’, *Photochemistry and Photobiology*, vol. 85, pp. 88-98

Medina, J. 2012, *Sensor CCD o CMOS? Qué significa todo esto?* (in Spanish), http://www.parentesis.com/tutoriales/Sensor_CCD_o_CMOS_Que_significa_todo_esto, accessed 18th February, 2013

Mednieks, Z. Dornin, L. Meike, G. and Nakamura, M. 2012, *Programming Android*, 2nd Edition, O'Reilly Media, Sebastapol, USA.

Meloni, D. Marenco, F. and di Sarra, A. 2003. 'Ultraviolet radiation and aerosol monitoring at Lampedusa, Italy', *Annals of Geophysics*, vol. 46, no. 2, pp. 373-383

Minoglou, K. De Munck, K. Tezcan, D. Van Hoof, C. De Moor, P. Bogaerts, J. and Veltroni, J. 2008, 'Backside illuminated thinned CMOS image sensors for space imaging', *IEEE Sensors 2008 Conference*, pp. 1429-1432

Mitchell, R. Campbell, S. and Qin, Y. 2010, 'Recent increase in aerosol loading over the Australian arid zone', *Atmospheric Chemistry and Physics*, vol. 10, pp. 1689-1699

Mitchell, R. and Forgan, B. 2003, 'Aerosol measurement in the Australian Outback: intercomparison of sun photometers', *Journal of Atmospheric and Oceanic Technology*, vol. 20, pp. 54-66

Moan, J. Dahlback, A. and Setlow, R. 1999, 'Epidemiological support for a hypothesis for melanoma induction indicating a role for UVA radiation', *Photochemistry and Photobiology*, vol. 70, pp. 243-247

Morys, M. Mims III, F. Hagreup, S. Anderson, S. Baker, A. Kia, J. and Walkup, T. 2001, 'Design, calibration, and performance of MICROTOPS II handheld ozone monitor and sun photometer', *Journal of Geophysical Research*, vol. 106, pp. 14573-14582

Nakamura, J. 2006, 'Basics of Image Sensors' in Nakamura, J. (ed) *Image Sensors and Signal Processing for Digital Still Cameras*, Boca Raton, CRC Taylor and Francis

Oliva, M. and Taylor, H. 2005, 'Ultraviolet radiation and the eye', *International Ophthalmology Clinics*, vol. 45, pp. 1-19

Orphal, J. 2003, 'A critical review of the absorption cross-section of O_3 and NO_2 in the ultraviolet and visible', *Journal of Photochemistry and Photobiology A: Chemistry*, vol. 157, pp. 185-209

Parisi, A. Sabburg, J. and Kimlin, M. 2004, *Scattered and Filtered UV Measurements*, Dordrecht, Kluwer Press

Paulos, E. Honicky, R. and Goodman, E. 2007, 'Sensing atmosphere', *SenSys 2007*, 6-9 November, Sydney, Australia

Perna, G. 2010, 'No longer niche, smartphones sales skyrocket', *International Business Times*, August 13, 2010

PhysOrg.com, 2011, 'UV-transparent coating for image sensors', http://www.physorg.com/news/2011-02-uv-transparent-coating-image-sensors.html accessed 21st September, 2011

Piri, E. Babaeian, M. Tavassoli, A. and Esmaeillan, Y. 2011, 'Effects on UV irradiation on plants', *African Journal of Microbiology Research*, vol. 5, pp. 1710-1716

Platt, U. Perner, D. and Patz, H. 1979, 'Simultaneous measurement of atmospheric CH_2O, O_3 and NO_2 by differential optical absorption', *Journal of Geophysical Research*, vol. 14, pp. 6329-6335

Poduri, S. Nimkar, A. and Sukhatme, G. 2010, 'Visibility monitoring using mobile phones', http://robotics.usc.edu/~mobilesensing/visibility/MobileAirQualitySensing.pdf accessed 18th September, 2011

Porter, J. Miller, M. Pietras, C. and Motell, C. 2001, 'Ship-based sun photometer measurements using Microtops Sun Photometers', *Journal of Atmospheric and Oceanic Technology*, vol. 18, pp. 765-774

Queface, A. Piketh, S. Annegarn, H. Holben, B. and Uthui, R. 2003, 'Retrieval of aerosol optical depth and size distribution from the CIMEL sun photometer over Inhaca Island, Mozambique', *Journal of Geophysical Research*, vol. 108, pp. 8509-8517

Rabe, J. Mamelak, A. McElgunn, P. Morison, W. and Sauder, D. 2006, 'Photoaging: mechanisms and repair', *Journal of the American Academy of Dermatology*, vol. 55, pp. 1-19

Radhi, M. Box, M. Box, G. Mitchell, R. Cohen, D. Stelcer, E. and Keywood, M. 2010, 'Optical, physical and chemical characteristics of Australian continental aerosols: results from a field experiment', *Atmospheric Chemistry and Physics*, vol. 10, pp. 5925-5944

Reddy, K. Prasad, P. and Singh, S. 2010, 'Effects of Ultraviolet-B radiation and its interactions with climate change factors on agricultural crop growth and yield’, *in* Gao, W. Schmoldt, D. and Slusser, J. (eds), *UV Radiation in Climate Change: Measurements, Modelling and Effects on Ecosystems*, Beijing. Tsinghua University Press, pp. 394-436

Rigel, D. 2008, ‘Cutaneous ultraviolet exposure and its relationship to development of skin cancer’, *Journal of the American Academy of Dermatology*, vol. 158, pp. S129-132

Rosales, A. Pedroni, J. and Tocho, J. 2006, ‘Symposium in Print: UV effects on aquatic and coastal ecosystems global spectral UV-radiometer with automatic shadow band’, *Photochemistry and Photobiology*, vol. 82, pp. 844-849

Sabburg, J. and Wong, J. 1999, ‘Evaluation of a ground-based sky camera system for use in surface irradiance measurement’, *Journal of Atmospheric and Oceanic Technology*, vol. 16, pp. 752-759

Samarek, A. Croager, E. Gies, P. Milne, E. Prince, R. McMichael, A. Lucas, R. and Slevin, T. 2006, ‘Estimates of beneficial and harmful sun exposure times for major Australian population centres’, *The Medical Journal of Australia*, vol. 184, pp. 338-341

Schnaiter, M. Horvath, H. Mohler, O. Naumann, K. Saathoff, H. and Schlock, O. 2003, ‘UV-VIS-NIR spectral optical properties of soot and soot-containing aerosols’, *Journal of Aerosol Science*, vol. 34, pp. 1421-1444

SciLab, http://www.scilab.org/ accessed 28th December, 2012

Scott, P. 2011, ‘Technology demystified: backside illuminated sensors’, *Cameratechnica*, http://www.cameratechnica.com/2011/06/23/technology-demystified-backside-illuminated-sensors/ accessed 14th April, 2012

Seinfeld, J. and Pandis, S. 2006, *Atmospheric Chemistry and Physics: From Air Pollution to Climate Change,* 2nd edition, Hoboken, John Wiley and Son

Setlow, R. Grist, E. Thompson, K. and Woodhead, A. 1993, ‘Wavelengths effective in induction of malignant melanoma’, *Proceedings of the National Academy of Sciences*, vol.90, pp. 6666-6670.

Siani, AM, Casale, G. Diemoz, H. Agnesod, G. Kimlin, M. Lang, C. and Colosimo, A. 2008, ‘Personal UV exposure in high albedo alpine sites’, *Atmospheric Chemistry and Physics*, vol. 8, pp. 3749-3760

Siani, AM. Casale, G. Modesti, S. and Colosimo, A. 2010, ‘Solar UV radiation as a double face environmental pollutant’, *Biophysics and Bioengineering Letters*, vol. 3, pp. 13-20

Siani, AM. Casale, G. Sisto, R. Borra, M. Kimlin, M. Lang, C. and Colosimo, A. 2009, ‘Short-term UV exposure of sunbathers at a Mediterranean Sea site’, *Photochemistry and Photobiology*, vol. 85, pp. 171-177

Sliney, D. 2005, ‘Exposure geometry and spectral environment determine photobiological effects on the human eye’, *Photochemistry and Photobiology,* vol. 81, pp. 483-489

Sliney, D. 2002, ‘How light reaches the eyes and its components’, *International Journal of Toxicology*, vol. 21, pp. 501-509

Sliney, D. 1995, ‘UV radiation ocular exposure dosimetry’, *Journal of Photochemistry and Photobiology B: Biology*, vol. 31, pp. 69-77

Slusser, J. Gibson, J. Bigelow, D. Kolinski, D. Disterhoft, P. Lantz, K. and Beaubien, A. 2000, ‘Langley Method of calibrating UV filter radiometers’, *Journal of Geophysical Research*, vol. 105, pp. 4841-4849

Slusser, J. Gibson, J. Bigelow, D. Kolinski, D. Mou, W. Koenig, G. and Beaubien, A. 1999, ‘Comparison of column ozone retrievals by use of an UV multifilter rotating shadow-band radiometer with those from Brewer and Dobson spectrophotometers’, *Applied Optics*, vol. 38, pp. 1543-1551

Smith, W. 2000, *Modern Optical Engineering*, McGraw Hill, New York

Soehnge, H. Ouhtit, A. and Ananthaswamy, H. 1997, ‘Mechanisms of induction of skin cancer by UV radiation’, *Frontiers in Bioscience*, vol. 2, pp. 538-551

Solar Light, (n.d.), *Model 540 Microtops II Sunphotometer*, http://www.solarlight.com/products/sunphoto.html accessed 20th January, 2013

SunSmart Victoria, 2012, ‘*Skin Cancer Stats and Facts*’, http://www.sunsmart.com.au/faqs/facts_and_stats accessed 29th December, 2012

Tetley, C. and Young, S. 2008,’Digital infrared and ultraviolet imaging, part 2: ultraviolet’, *Journal of Visual Communication in Medicine*, vol. 31, pp. 51-60

Theuwissen, A. 2008, ‘CMOS image sensors: state-of-the-art’, *Solid State Electronics*, vol. 52, pp. 1401-1406

Torres, O. Bhartia, P. Herman, J. Sinyuk, A. Ginoux, P. and Holben, B. 2002, ‘A long-term record of aerosol optical depth from TOMS observations and comparison to AERONET measurements’, *Journal of the Atmospheric Sciences*, vol. 59, pp. 398-413

Tsaknakis, G. Papayannis, A. Kokkalis, P. Amiridis, V. Kambezidis, H. Mamouri, R. Georgoussis, G. and Avdikos, G. 2011, ‘Inter-comparison of lidar and ceilometer retrievals for aerosol and planetary boundary layer profiling over Athens, Greece’, *Atmospheric Measurement Techniques Discussions*, vol. 4, pp. 73-99

Turner, J. and Parisi, A. 2009, ‘Measuring the influence of UV reflection from vertical metal surfaces on humans’, *Photochemical and Photobiological Sciences,* vol. 8, pp. 62-69

Vajdic, C. Kricker, A. Giblin, M. McKenzie, J. Aitken, J. Giles, G. and Armstrong, B. 2002, ‘Sun exposure predicts risk of ocular melanoma in Australia’, *International Journal of Cancer*, vol. 101, pp. 175-182

Verhoeven, G. and Schmitt, K. 2010, ‘An attempt to push back frontiers – digital near-ultraviolet aerial archaeology’, *Journal of Archaeological Science*, vol. 37, pp. 833-845

Vierkotter, A. and Krutmann, J. 2012, ‘Environmental influences on skin aging and ethnic-specific manifestations’, *Dermato-Endocrinology,* vol. 4, pp. 1-5

Wang, S. Setlow, R. Berwick, M. Polsky, D. Marghoob, A. Kopf, A. and Bart, R. 2001, ‘Ultraviolet A and melanoma: A rReview’, *Journal of the American Academy of Dermatology,* vol. 44, pp. 837-846

Wayne, C. and Wayne, R. 2005, *Photochemistry,* New York, Oxford University Press

Webb, A. 1998, *UVB Instrumentation and Applications,* Amsterdam, Gordon and Breach Publishers

Wenham, S. Green, M. Watt, M. Corkish, R. and Sproul, A. (2012), *Applied Photovoltaics*, 3rd edition, Earthscan, New York

Wenny, B. Saxena, V. and Frederick, J. 2001, ‘Aerosol optical depth measurements and their impact on surface levels of ultraviolet-B radiation’, *Journal of Geophysical Research*, vol. 106, pp. 17311-17319

Westly, E. 2009, ‘Citizen science: how smartphones can aid scientific research’, *Popular Mechanics*, http://www.popularmechanics.com/science/4308375 accessed 26th January, 2012

World Health Organisation (WHO), 2012, *Ultraviolet Radiation and the INTERSUN Program*, http://www.who.int/uv/uv_and_health/en/ accessed 20th December, 2012

Yaar, M. and Gilchrest, B. 2007, “Photoaging: mechanism, prevention and therapy’, *Britih Journal of Dermatology*, vol. 157, pp. 874-887

Yabe, T. Holler, R. Tohno, S. and Kasahara, M. 2003, ‘An aerosol climatology at Kyoto: observed local radiative forcing and columnar optical properties’, *Journal of Applied Meteorology*, vol. 42, pp. 841-850

Yamanoi, Y. Takeuchi, S. Okumura, S. Nakashima, S. and Yokoyama, T. 2008, ‘Colour measurements of volcanic ash deposits from three different styles of summit activity at Sakurajima Volcano, Japan, conduit processes recorded in colour of volcanic ash’, *Journal of Volcanology and Geothermal Research*, vol. 178, pp. 81-93

York, D. Evensen, N. Martinez, M. and Delgado, J. 2004, ‘Unified equations for the slope, intercept, and standard errors of the best straight line’, *American Journal of Physics*, vol. 72, pp. 367-375

Young, C. 2009, ‘Solar ultraviolet radiation and skin cancer’, *Occupational Medicine*, vol. 59, pp. 82-88

Zepp, R. Erickson III, D. Paul, N. and Sulzberger, B. 2011, ‘Effects of solar UV radiation and climate change on biogeochemical cycling: interactions and feedbacks’, *Photochemical and Photobiological Sciences*, vol. 10, pp. 261-279

Zhang, M. Queshi, A. Geller, A. Frazier, L. Hunter, D. and Han, J. 2012, ‘Use of tanning beds and incidence of skin cancer’, *Journal of Clinical Oncology*, DOI: 10.1200/JCO.2011.39.2652

Zigman, S. 2005, ‘Ultraviolet A and cataracts: basic research and practical applications’, *International Ophthalmology Clinics*, vol. 45, pp. 29-40

Zlater, Z. Lidon, F. and Kaimakanova, M. 2012, ‘Plant physiological responses to UVB radiation’, *Emirates Journal of Food Agriculture*, vol. 24, pp. 481-501

Appendix 1: Published Papers

Igoe, D. Parisi, A. and Carter, B. 2013a, ‘Charcterization of a Smartphone’s Response to Ultraviolet A Radiation’, *Photochemistry and Photobiology*, vol. 89, pp. 215-218

Igoe, D. Parisi, A. and Carter, B. 2013b, ‘Smartphones as tools for delivering sun-smart education to students’, *Teaching Science*, vol. 59, pp. 36-38

Igoe, D. Parisi, A. and Carter, B. 2013c, ‘Evaluating UVA aerosol optical depth using a smartphone camera’, *Photochemistry and Photobiology*, DOI: 10.1111/php.12082

Igoe, D. Parisi, A. and Carter, B. 2013d, ‘Smartphone based Android app for determining UVA aerosol optical depth and direct solar irradiances.’, *accepted by Photochemistry and Photobiology.*